Mechanical Regulation in Cell Division and in Neurotransmitter Release

Sathish Thiyagarajan

Submitted in partial fulfillment of the
requirements for the degree of
Doctor of Philosophy
in the Graduate School of Arts and Sciences

COLUMBIA UNIVERSITY

2018

ABSTRACT

Mechanical Regulation in Cell Division and in Neurotransmitter Release

Sathish Thiyagarajan

During their lifecycle, cells must produce forces which play important roles in several subcellular processes. Force-producing components are organized into macromolecular assemblies of proteins that are often dynamic, and are constructed or disassembled in response to various signals. The forces themselves may directly be involved in subcellular mechanics, or they may influence mechanosensing proteins either within or outside these structures. These proteins play different roles: they may ensure the stability of the force-producing structure, or they may send signals to a coupled process. The generation and sensing of subcellular forces is an active research topic, and this thesis focusses on the roles of these forces in two key areas: cell division and neurotransmitter release.

The first part of the thesis deals with the effect of force on cell wall growth regulation during division in the fission yeast *Schizosaccharomyces pombe*, a cigar-shaped, unicellular organism. During cytokinesis, the last stage of cell division in which the cell physically divides into two, a tense cytokinetic ring anchored to the cellular membrane assembles and constricts, accompanied by the inward centripetal growth of new cell wall, called septum, in the wake of the inward-moving membrane. The contour of the septum hole maintains its circularity as it reduces in size—an indication of regulated growth. To characterize the cell wall growth process, we performed image analysis on contours of the leading edge of the septum obtained via fluorescence microscopy in the labs of our collaborators. We quantified the deviations from circularity using the edge roughness. The roughness was spatially correlated, suggestive of regulated growth. We hypothesized that the cell wall growers are mechanosensitive and respond to the force exerted by

the ring. A mathematical model based on this hypothesis then showed that this leads to corrections of roughness in a curvature-dependent fashion. Thus, one of the roles of ring tension is to communicate with the mechanosensitive septum growth processes and coordinate growth to ensure the daughter cells have a functional cell wall.

The second part of the thesis deals with how ring tension is produced and sustained, using experimentally measured ultrastructure of the cytokinetic ring itself. Recent super-resolution experiments have revealed that several key proteins of the fission yeast constricting ring are organized into membrane-anchored complexes called nodes. The force producing protein myosin-II in these nodes exerts pulling forces on polymeric actin filaments that are synthesized from polymerizers residing in the nodes. How these forces are marshalled to generate ring tension, and how such an organization maintains its stability is unclear. Using a mathematical model with coarse-grained representations of actin and myosin, we showed that such a node-based organization reproduces previously measured ring tension values. The model explains the origin of experimentally observed bidirectional motion of the nodes in the ring, and showed that turnover of the nodes rescues the ring from inherent contractile instabilities that would be expected when a force-producing structure is made up of small object that effectively attract one another.

Finally, the third part of the thesis deals with the role of forces produced by SNARE proteins at synapses between two neurons during neurotransmission. A key step here is synaptic release, where inside a neuron, membrane-bound compartments called vesicles filled with neurotransmitter fuse with the membrane of the neuron forming a transient fusion pore, and release their contents to the outside of the cell. These neurotransmitter molecules are sensed by another neuron that is physically separate from the neuron in question and this neuron propagates the signal henceforth. Thus, regulation of neurotransmitter release is a key step in neurotransmission. A fusion machinery consisting of several proteins facilitates membrane fusion, and pore nucleation requires the formation of a SNARE protein complex in this machinery, whose role during pore dilation is unclear. Using electrophysiological measurements, our collaborators experimentally measured the statistics of the size of single fusion pores *in vitro,* and observed that average pore sizes increased with the number of SNARE proteins. Using mathematical modeling, we showed that this effect was due to an entropic crowding force that expands the pore and increases with the number of SNAREs, and counteracts the energy barrier to fusion pore expansion.

Contents

List of Figures

List of Tables

Acknowledgements

I wish to thank my advisor Prof. Ben O’Shaughnessy for the constant guidance and support throughout my Ph. D. I enjoyed our several discussions and they benefitted the content and the direction of the thesis tremendously. I have found that my thinking is much clearer and that I have grown in confidence due to his close mentorship. I also wish to thank other current and former members of our research group: Shuyuan Wang and Drs. Matt Stachowiak, Brett Alcott, Ben Stratton, Jason Warner, and Anirban Polley for the many fruitful discussions.

This work benefitted greatly from the several interesting experiments performed in the groups of our collaborators, Prof. Thomas Pollard and Prof. Erdem Karatekin. Although the work here is primarily theory-based, I had the good fortune of performing some of the experiments myself, and I thank Prof. Pollard for being a gracious host. I also thank Drs. Caroline Laplante and Rajesh Arasada of the Pollard group, and Dr. Zhenyong Wu of the Karatekin group.

I wish to thank the National Institutes of Health for funding our research. Government support is crucial for research in the basic sciences, and I hope this continues at or above the current level for many years to come.

Finally, I wish to thank my parents T. Lalitha and V. A. Thiyagarajan, and my friends Sujay Prasad Srivastava, Ananda Theertha, Rajkumar RB, Filip Cosmanescu, Siddharth Ramesh, Royston Fernandes, and Claudia Solis-Roman for tolerating me.

To my parents and friends.

Chapter 1: Introduction

Cellular forces are important in a wide variety of cellular processes (Schoen *et al.*, 2013). Forces developed by muscle cells are essential to several key functions of the human body (Lieber and Ward, 2011). During cell division, forces are used to separate chromosomes to ensure correct division of nuclear material, and during cytokinesis are thought to drive cell division by pinching the cell into two (Green *et al.*, 2012). In addition to force generation, a variety of proteins are sensitive to forces (Wang *et al.*, 2001). Proteins that polymerize other proteins either up or downregulate their polymerization depending on the amount of force exerted on them (Courtemanche *et al.*, 2013; Jégou *et al.*, 2013). Yet others undergo structural changes upon the action of force (Hytönen and Vogel, 2005). How do these force producers and force sensitive proteins come together to form a successful macromolecular assembly?

Perhaps the most studied force-producing structure is muscle (Cooke, 1997). The two proteins actin and myosin-II generate forces here; contractile forces are produced by myosin-II molecules pulling on polymeric filaments of actin. The spatial organization of these proteins in muscle is well-understood (Schiaffino and Reggiani, 2011). Actin and myosin form repeat units called sarcomeres, and each muscle cell contains several sarcomeres arranged in long-lived periodic arrays. Actin and myosin are also used in subcellular structures to generate force, but these structures are often assembled and disassembled over timescales ranging from a few minutes to a few hours. During these processes, the cell may undergo shape changes and or locomotion in part due to these forces. In such a dynamic environment, how do these structures produce force? Do these forces help regulate the coupled processes? Contractile structures are prone to instabilities that could result in runaway expansion and hence severing; how is the stability of these structures maintained? The goal of this thesis is to partially answer these questions as applied to two processes: cell division and neurotransmission.

Cytokinesis

Cytokinesis is the last stage in cell division where the cell physically divides into two daughter cells. As the nuclear material has already been segregated by this stage, the bulk of the cell splits in to two daughter cells during this process. Several diseases such as cancer, anaemia, and age-related macular degeneration, to name a few, are associated with failure of cytokinesis (Lacroix and Maddox, 2012).

In fungi and animal cells, a contractile ring assembles in the division plane attached to the membrane of the cell. The ring develops tension and constricts along with the cell, and this tension is thought to drive the whole process. The ring is made up of several proteins (Pollard and Wu, 2010). Of interest are the two proteins actin and myosin-II. Actin forms helical polymeric filaments; the two ends are called the barbed and the pointed end (Carlier, 1991). Myosin-II molecules pull on the filaments with the force parallel to the barbed-pointed axis. These interactions add up to give rise to a tense ring, which has been measured in fission yeast previously to be ~400 pN (Stachowiak *et al.*, 2014).

Fission yeast as a model organism

The fission yeast *Schizosaccharomyces pombe* is a model organism used to study cytokinesis. It is a cell-wall enclosed, cigar-shaped unicellular organism whose cross-sectional diameter is ~4 μm and length is ~14 μm at the onset of division. The cytokinetic ring is well-characterized in fission yeast. Several ring proteins have been identified, their amounts measured throughout assembly of the ring, maturation, and constriction, and their biophysical properties have been characterized. Its genome has also been sequenced (Wood *et al.*, 2002), making it easy to obtain cells with mutated genes for experiments, in order to study the function of a given protein. Given the relatively short cell cycle (~ 3 hours) and ease of genetic manipulation, it is widely used. Lessons learned here can be carried over to mammalian cells as several ring proteins of *S. pombe* are homologous to their mammalian counterparts. Fission yeast is arguably the only organism where a rigorous cytokinetic ring model can be developed in a quantitative manner.

Lifecycle and structure of the contractile ring in *S. pombe*

The ring assembles, matures, and constricts, in that order. A broadband of membrane-anchored protein complexes called nodes appear at the middle of the cell at the membrane just prior to cytokinesis. These nodes synthesize actin filaments via polymerization at the nodes by the actin synthesizing protein formin Cdc12. The nodes also contain myosin-II, these exert force on the actin filaments being grown from neighboring nodes. Such a search-capture-pull-release mechanism draws these nodes together and forms a compact actomyosin ring (Wu *et al.*, 2006; Vavylonis *et al.*, 2008). The protein content of the ring changes throughout maturation. Then, ~30 mins after the broad band assembles, the ring begins constricting (Wu and Pollard, 2005).

Recent super-resolution studies have started to shed light on the ultrastructure of the ring. Using fluorescence photoactivated localization microscopy (FPALM) that can probe length scales of ~35 nm, a study discovered that nodes persist into constriction (Laplante *et al.*, 2016). These have well-defined stoichiometric ratios of several ring components, and move bidirectionally within the ring. Another recent study obtained the distances of several ring components from the plasma membrane, using images from fixed (dead) cells. This study revealed that ring components seem to be grouped into three distinct layers within the ring, with each serving a different function related to scaffolding, signaling, and force generation (Mcdonald *et al.*, 2017).

Septum growth in *S. pombe* cytokinesis

Cytokinesis in fission yeast cells is accompanied by cell wall growth that ingresses in the wake of the constricting ring. This newly synthesized cell wall material is produced by several transmembrane proteins that reside at the membrane of the cell. The cell wall is a crosslinked polysaccharide network with a high elastic modulus ~50 MPa (Atilgan *et al.*, 2015). It is largely made up of β-glucan, a polymeric form of glucose, and is ~200 nm thick. It is synthesized by transmembrane β-glucan synthases in the membrane that are thought to polymerize glucans using UDP-Glucose as their substrate (Cortés *et al.*, 2007; Munro, 2013).

SNARE proteins and the fusion machinery

The basic process of membrane fusion is implicated in both the release of neurotransmitters and the release of hormones (Jahn and Scheller, 2006). These release processes are tightly controlled as the functioning of the nervous system and the endocrine system depend on these. Several proteins including soluble N-ethyl maleimide sensitive factor attachment protein receptors (SNAREs), SM (Sec1/Munc18-like) proteins, Complexin, Synaptotagmin-1 are involved in the formation of fusion pores between vesicles and cell membranes (Südhof and Rothman, 2009).

The SNAREs are the core of the fusion machinery. Syntaxin-1 and SNAP-25 located on the presynaptic plasma membrane (t-SNAREs) and the vesicle-associated membrane protein (VAMP or v-SNARE) form a four-helix bundle between the vesicle and the membrane, a “SNAREpin” that catalyzes fusion. The exact nature of this catalysis is unclear. The zippering process where these three proteins come together to form one four helix bundle releases ~65 kT of energy (Gao *et al.*, 2012). A recently published model predicts that this energy is dissipated quickly after assembly, and that the entropic force from steric interactions between SNAREpins brings membranes into close contact and drives fusion (Mostafavi *et al.*, 2017).

Outline of the thesis and my contributions

The first part of the thesis deals with cell division in fission yeast. During cytokinesis, the last stage in cell division, a contractile ring attached to the cellular membrane assembles and constricts, accompanied by the inward centripetal growth of the cell wall in its wake. Using fluorescently labelled cell wall growing proteins, we extracted the leading edge of the newly synthesized cell wall (septum) using image analysis. We found that the contour of the cell wall hole was almost circular, and quantified the deviations from circularity using the edge roughness. The roughness was spatially correlated and suggested that cell wall growth was regulated. We hypothesized that the cell wall growers are mechanosensitive and respond to the force exerted by the ring. A mathematical model based on this hypothesis then showed that this leads to corrections of roughness in a curvature-dependent fashion. Thus, one of the roles of ring tension is to communicate with the mechanosensitive septum growth fashion and ensure that the closure is circular to ensure the daughter cells have a functional cell wall. This part of the thesis has been adapted from (Thiyagarajan *et al.*, 2015). Here, I performed the image analysis and mathematical modeling, and compared predictions of the model with experiment. I also performed experiments to obtain a subset of the images used here, the rest were obtained by our colleagues at Columbia and Yale.

The second part of the thesis deals with the ultrastructure of the contractile ring itself. Recent super-resolution experiments have revealed that several key proteins of the constricting ring are organized into membrane-anchored complexes called nodes. Two key proteins are the actin polymerizer formin, and the force-producing myosin-II. Forces are produced by myosin-II pulling on actin filaments, but how these forces are marshalled together to generate ring tension is unclear. Using a mathematical model with coarse-grained representations of actin and myosin, we showed that the node-based organization ensures that the force-producing interactions are aligned for high tension. The model reproduces experimentally observed bidirectional motion of the nodes in the ring. The model also showed that turnover rescues inherent contractile instabilities in the ring. This part of the thesis has been adapted from (Thiyagarajan *et al.*, 2017). This is a study with only mathematical modeling, with the work here performed by Shuyuan Wang, another graduate student in my group, and I. We both contributed equally here.

Finally, the third part of the thesis deals with neurotransmission. During synaptic release, neurotransmitters are released between neurons and these are an essential part of their communication. SNAREs complexes assemble at the fusion site, and are thought to play an important role in the process. Our collaborators at Yale created small patches of membrane ~23 nm in diameter with v-SNAREs reconstituted in them, and fused these with the outer membrane of a cell expressing cognate, ‘flipped’ t-SNAREs. They were able to isolate single pores resulting from this fusion process and performed conductance measurements. They analyzed the data to obtain characteristics of fusion pore sizes. This part of the thesis has been adapted from (Wu *et al.*, 2017). Our experimental colleagues at Yale performed all the experiments and the data analysis on the electrophysiological recordings thus obtained. I performed the mathematical modeling and compared these theoretical results to the experiments.

Chapter 2: The Fission Yeast Cytokinetic Contractile Ring Regulates Septum Shape and Closure

Introduction

Fungal and bacterial cells are enclosed by a cell wall whose growth is spatiotemporally regulated to maintain and evolve cell shape throughout the cell cycle (Das *et al.*, 2012; Cabib and Arroyo, 2013; Pinho *et al.*, 2013). Following cell division the fission yeast *S. pombe*, a rod-shaped fungus, elongates by growth at the rounded cell tips, whereas cell wall synthesis by the ovoid bacterium *Streptococcus pneumoniae* is largely confined to a region close to the division site and occurs during cell division (Pinho *et al.*, 2013). The cell wall is a high modulus crosslinked network that withstands high turgor pressures and must be reshaped if the cell shape is to change. The mechanisms are debated, but growth is regulated by various signaling pathways in *S. pombe* (Krapp and Simanis, 2008; Das *et al.*, 2012) and annealing of crosslinks is thought to assist local remodeling in the rod-shaped bacterium *E. coli* (Furchtgott *et al.*, 2011). Mechanical effects may also play a role. In *S. pombe*, network stretching by turgor pressure was proposed to promote insertion of cell wall material locally (Drake and Vavylonis, 2013). Mechanical stress increases the rates of cell wall synthesis in *E. coli* (Amir *et al.*, 2014), and the actin homologue MreB localizes to regions of negative curvature that define the sites of growth (Ursell *et al.*, 2014).

Precise regulation of cell wall growth is essential for cell division, a process that results in two daughter cells that are properly enclosed by new cell wall. In fission yeast and other fungi and bacteria this is accomplished by growth of a septum in the central division plane during cytokinesis, the final stage of the cell cycle. Yeast grows a ~ 0.3 μm thick septum by centripetal growth of the almost circular inner septum edge that closes down the central septum hole over ~ 25 mins, separating the ~ 3.7 μm diameter cell into two sealed compartments (Wu and Pollard, 2005) (Fig. 2.1A). Constriction of the septum is tightly coupled to constriction of an actomyosin contractile ring attached to the inside of the plasma membrane adjacent to the leading septum edge (Muñoz *et al.*, 2013).

During septation, maintenance of the circularity of the growing septum edge ensures proper septum closure down to almost a point and encloses the daughter cells in new cell wall, but the regulating mechanism is unknown. For example, if the septum had an elongated shape it would close down to almost a slit. The β-glucan and α-glucan synthases Bgs1-4 and Ags1 residing in the plasma membrane grow the septum (Martín *et al.*, 2003; Cortés *et al.*, 2005, 2007, 2012) (Fig. 2.1A). At the onset of constriction several thousand Bgs1 proteins participate at different locations around the edge (Cortés *et al.*, 2007; Proctor *et al.*, 2012; Arasada and Pollard, 2014). Given the intrinsic stochasticity of molecular complexes (Wang *et al.*, 1998; Geertsema *et al.*, 2014), independently operating Bgs1 molecules would presumably generate irregular edges; to maintain a smooth circular septum edge requires that growth rates at locations up to ~ 4 μm apart be coordinated. How the cell accomplishes this considerable technical challenge is unknown.

Several observations suggest that the yeast cytokinetic ring interacts with Bgs1. The actomyosin ring is required for localization of Bgs1 into a compact band at the division site (Liu *et al.*, 2002), and deletion of the IQ motifs from the ring component IQGAP Rng2 gives a uniform distribution of Bgs1 over the septum, in contrast to the wild-type distribution concentrated at the septum edge (Tebbs and Pollard, 2013). In mutants with reduced levels of the contractile ring protein Cdc15, the ring slid along the membrane until ~2000 Bgs1 molecules were recruited to the membrane adjacent to the ring (Arasada and Pollard, 2014). Thus the ring could influence septum growth, and mechanical interactions could play a role since the fission yeast ring was reported to exert ~ 400 pN of tension (Stachowiak *et al.*, 2014). Indeed, mutations of other ring components affect septation. Septa were abnormally thickened or incomplete with low expression levels of Myo2p (Kitayama *et al.*, 1997), while aberrant septum growth with disjoint patches of septal material was observed in temperature sensitive mutants of the contractile ring proteins profilin Cdc3, myosin light chain Cdc4, and tropomyosin Cdc8 (Streiblova *et al.*, 1984). Mutations in Bgs proteins can also influence the ring, as in cells with reduced levels of Bgs4 where constriction of the contractile ring appears to be faster than septum ingression (Muñoz *et al.*, 2013).

Here we present experimental and theoretical evidence that the contractile ring tension regulates septum shape during cytokinesis by controlling local growth rates. We measured ingrowing septum edges in live cells and quantified their deviations from circularity by the edge roughness, borrowing a classic definition from materials physics (Lapujoulade, 1994). The edges were inconsistent with independent Bgs-mediated growth processes, which would produce scale-independent roughness always increasing in time. Instead, roughness grew with length scale according to a power law, and peaked and decayed in time. In cells lacking intact actomyosin rings, septa constricted but had much greater roughness. To explain these findings we postulated that Bgs-mediated synthesis of septum is mechanosensitive, and that the contractile ring communicates mechanically with the septum synthesis machinery. A mathematical model showed that this mechanism generates smooth, circular septum edges with roughness that peaks in time and has power law dependence on length scale close to that observed. Our results suggest that cytokinetic ring tension does not set the rate of constriction, but regulates circularity of the septum and its defect-free closure by its effect on mechanosensitive Bgs-mediated growth processes.

Results

Ingressing septum edges during fission yeast septation have a roughness ~5% of ring radius that decreases in time

We sought to quantify the deviation from circularity of septum edges during cytokinesis in *S. pombe,* and to test if growth at the septum edge is spatially coordinated to regulate the edge to be smooth and circular. We extracted edges from experimental images and quantified their roughness, the root mean square (rms) fluctuation in height, a common measure of irregularity (Lapujoulade, 1994).

We used confocal microscopy to image cells expressing GFP-Bgs4 or RFP-Bgs4, which localize to the surface of the septum, and myosin-II light chain Rlc1-GFP or the F-BAR domain containing protein Cdc15-Tomato, which localize to the contractile ring (Le Goff *et al.*, 2000; Cortés *et al.*, 2005; Roberts-Galbraith *et al.*, 2009) (Fig. 2.1B). During constriction Bgs4 was distributed on the entire septum surface up to the location of the contractile ring, showing that the ring followed the inner septum edge and suggesting that Bgs4 reliably marked the edge. We traced septum edges using the Canny edge detection method based on intensity gradients (Fig. 2.1B, 2.7A, and Materials and Methods). The mean radius of septum edges decreased linearly in time with a mean constriction rate 80 ± 10 nm/min (mean ± s.d., n = 21 constrictions) (Fig. 2.1C).

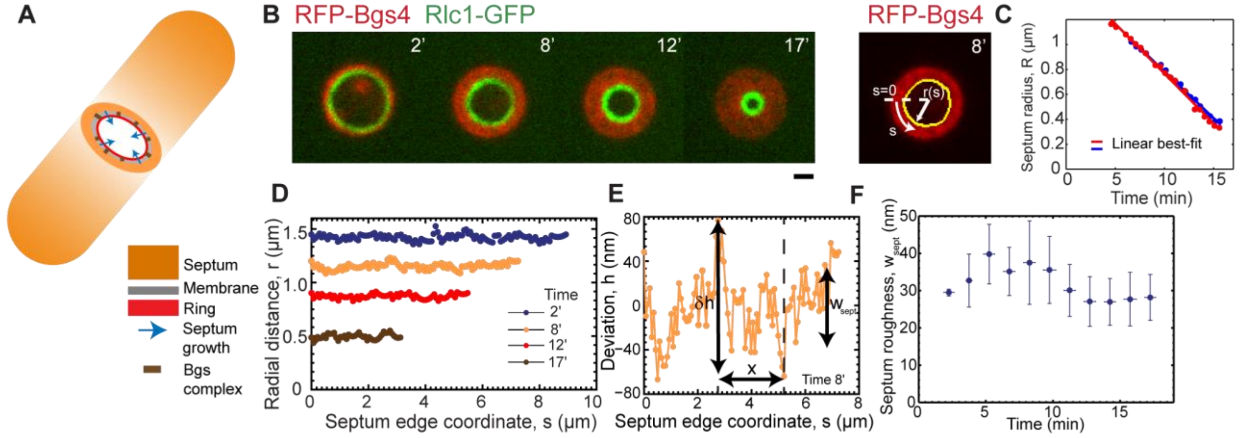

Figure 2.1. Constricting septum edges in fission yeast are nearly circular with low roughness. (A) Schematic of a *S. pombe* cell during cytokinesis, showing how constriction of the contractile ring and the septum edge are tightly coupled. The edge grows inwards as β-glucan synthases (Bgs) in the membrane synthesize the septum. (B) Confocal fluorescence micrographs of division plane during constriction-septation of a yeast cell expressing RFP-Bgs4 and Rlc1-GFP (*t = 0* is the onset of septum growth). Right: Edge determination (yellow) for the septum at 8 min. Bar: 1 µm. (C) Mean septum radius versus time for constrictions of two typical cells (blue and red symbols). The best fit straight lines have slopes of 75 nm/min (blue) and 80 nm/min (red). (D) Radial distance profile for each of the 4 septum edges in (B). (E) Enlarged view of edge profile at 8 min in (D) with details of deviation, $h(s)$, of radial distance from mean value *R*. The roughness *w* of edges on a scale *x* quantifies the variations in edge radius on that scale, δh. (F) Septum roughness versus time for experimental constrictions (*n* = 326 edges from 21 constrictions). Bin width, 1.5 min. Plotted points are mean ± s.d.

For an edge grown by independent random growth processes the roughness always increases in time (Lesne and Laguës, 2012). To test septum edges for this feature we fit best circles to measured edges and determined the deviations from circularity, $h(s)$, and hence the roughness, $w_{\text{sept}} = <(\delta h)^2>^{1/2}$ (Figs. 2.1B, D-F and Materials and Methods). Here δh denotes the deviation from the mean and the average is over all points on the edge. The roughness of septum edges decreased in time, in some cases showing an early increase before peaking and decreasing (Figs. 2.1F, 2.6A). The mean time averaged roughness was 31 ± 9 nm (mean ± s.d.) over n = 326 septum edges from 21 cells. Throughout, a 'septum edge' refers to a septum at one instant in time, and the statistics we present are averaged over many edges, i.e. we report averages over time and over different cells. The mean roughness is a small fraction 5.0 ± 1.8% of the septum radius, and the roughness does not show the steady increase in time characteristic of uncorrelated growth processes.

The roughness of septum edges increases with length scale and follows a power law

If septum edges are grown by statistically independent septum synthesis processes around the edge, at any instant the roughness would have a constant value independent of length scale, whereas if the septum shape is regulated growth rates at different locations would be correlated. A hallmark of spatially correlated growth is scale-dependent roughness: the longer the section of the edge, the bigger the fluctuations and the roughness within that section (Lesne and Laguës, 2012).

To test for growth correlations we calculated the mean roughness on the scale x, $w(x) = \, < (\delta h)^2 >_{\mathrm{x}}^{1/2}$, where the average is over all points in a given section of the septum edge of length *x*, and then over all such regions (Fig. 2.1E and Materials and Methods). The roughness of edges increased with length scale up to a saturation scale x_{sat} (Fig. 2.2A). For practical reasons, we define x_{sat} as the scale where roughness attains 80% of its maximum value, w_{sept}. The x_{sat} versus time curve, averaged over all edges, increased, peaked after ~ 5 min and thereafter decreased (Fig. 2.2B). Values of roughness and x_{sat} varied considerably from cell to cell (Figs. 2.6A,B), and for many individual cells we did not record a peak in x_{sat}, possibly because imaging commenced after the peak occurred. Averaged over all edges, roughness followed a power law $w \sim x^{\alpha}$ for $x < x_{\mathrm{sat}}$, with best-fit exponent $\alpha = 0.47 \pm 0.03$ (95% confidence interval, *n* = 326 septum edges from 21 cells) (Fig. 2.2C). Thus, septum edges are grown by spatially coordinated processes and have a characteristic roughness exponent.

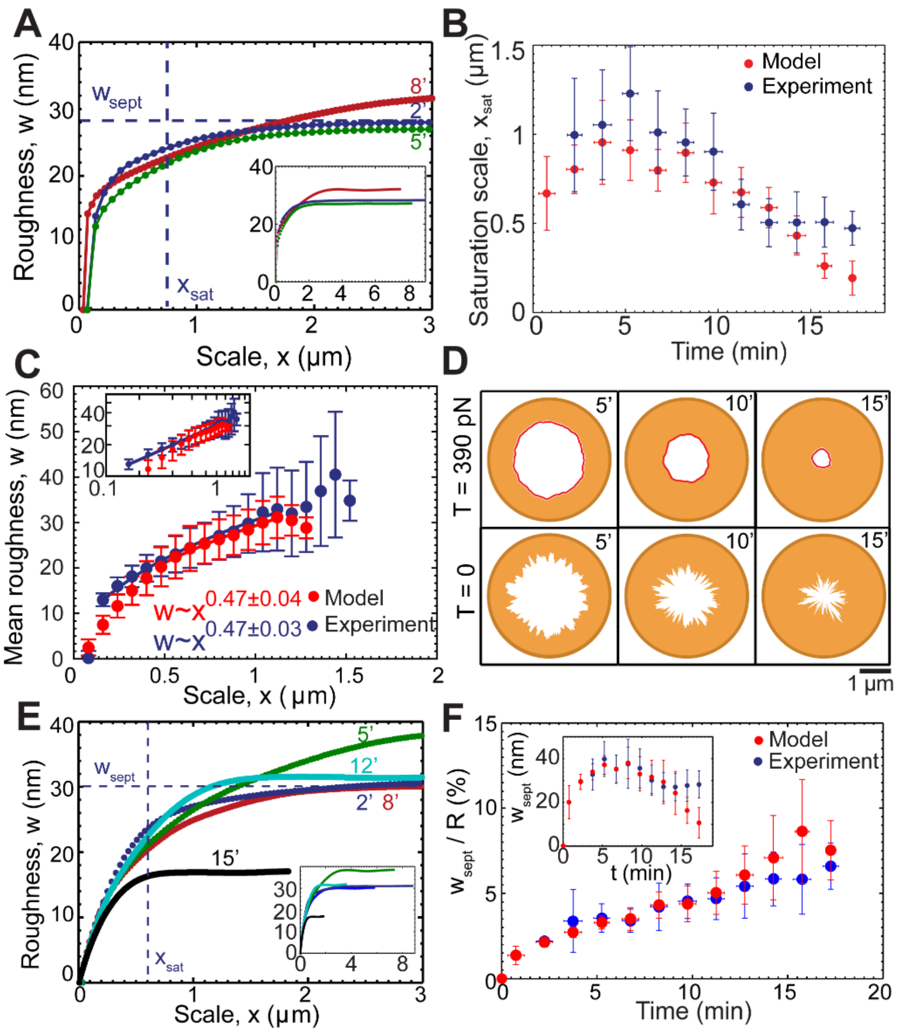

Figure 2.2. Roughness of septum edges is length scale dependent and follows a power law reproduced by a model of septum growth regulated by ring tension.

Table 2.1 lists the model parameters. (A) Roughness *w* versus length scale *x* for the septum edges of Fig. 2.1B at the indicated times. Dashed lines: w_{sept} and x_{sat} at time 2 min. Inset: full roughness profiles. (B) Roughness saturation length, x_{sat} versus time for (blue) experimental constrictions of Fig. 2.1F and (red) simulated constrictions (simulation: *n* = 428 edges from 30 constrictions). Points are mean ± s.d. Bin width, 1.5 min. (C) Mean roughness *w* versus length scale *x* for the experimental and simulated constrictions of (B). For each *x*, the mean is over all constrictions for which $x < x_{\mathrm{sat}}$ and over all times. The exponent of the best fit power law to simulated data is 0.47 ± 0.04 (95% confidence interval) for 0.48 μm $\leq x \leq$ 1.12 μm. Error bars denote s.d. Inset: Plot of log mean roughness versus log length scale *x*. (D) Typical simulated septum edges at indicated times (min) after the onset of constriction at two tensions: (top row) *T* = 390 pN as measured in protoplasts; and (bottom row) *T* = 0. (E) Roughness w versus scale x for simulated constrictions at *T* = 390 pN in (D). Dashed lines: Maximum roughness w_{sept} and roughness saturation scale x_{sat} after 2 min. Inset: Complete roughness profiles for the same edges. (F) Ratio of septum roughness to mean septum radius versus time for simulated and experimental constrictions and times of (B). Inset: Septum roughness versus time for same data. Bin width, 1.5 min. Points are mean ± s.d.

The values of roughness we report, $\lesssim$ 40-50 nm, are less than the pixel size (~65 nm) of our images and the estimated confocal microscopy point spread function (psf) width (~200 nm). To test our method, we generated artificial septum edges with roughness exponent $\alpha = 0.5$ and variable roughness (Fig. 2.7B-I). We mimicked confocal imaging of these edges with pixel size 65 nm and psf width 200 nm, we applied our edge detection algorithm to these 'images,' and we measured roughness w_{sept} and exponent α of these detected edges. For test data edges with actual roughness ~30 nm, typical of values we report in this study, our measurement procedure produced a similar roughness and an exponent ~ 0.37. This test suggests our method reproduces actual roughness to within ~ 20% of the actual value, but somewhat underestimates the roughness exponent (see Fig. 2.7 and caption).

Mathematical model of septum growth regulated by ring tension

Since the contractile ring is attached to the plasma membrane adjacent to the septum, the ring tension could mechanically influence the septum and the processes that synthesize it. The ring may plausibly have direct mechanical interactions with Bgs complexes, since Bgs1p is an integral membrane protein (Liu *et al.*, 2002). To examine if such effects could explain the highly correlated growth we observed, we developed a model of the stochastic centripetal growth of the inner septum edge that closes down the septum, assuming septum synthesis is mechanosensitive. Here we outline the main features of the model; for further details, see Materials and Methods.

The radius of the inner septum edge is defined to be $r(s,t) = R(t) + h(s,t)$ at location s on the edge at time t (Fig. 2.1B). Here $R(t)$ is the mean radius and $h(s,t)$ the deviation from circularity at s (Fig. 2.1B, D, E). We assume that the inward growth velocity $v_{\text{sept}}(s,t) \equiv -\partial r/\partial t$ due to Bgs complex-mediated synthesis of septum depends on the radial force per unit length, γ, exerted on the septum at that location by the contractile ring,

$$v_{\text{sept}}(s,t) = v_{\text{sept}}^{0}\left(1 + \frac{\gamma(s,t)}{\gamma^{\star}}\right) + \eta_{\text{fluc}}(s,t). \tag{2.1}$$

Here v_{sept}^{0} is the intrinsic septum edge growth velocity. The force is communicated to the septum synthesis apparatus and thereby accelerates growth by the factor γ/γ^{*}, where $\gamma^{\star}$ is a response threshold for the molecular machinery. The crucial term η_{fluc} represents fluctuations of the growth rate about the mean whose strength, λ, sets the magnitude of the edge roughness. This term describes independently operating growth machines around the septum, $< \eta_{\text{fluc}}(s,t)\eta_{\text{fluc}}(s',t') >= \lambda\, \delta(s-s')\delta(t-t')$. It is the force term in eq. 2.1 that will introduce growth correlations and shape regulation.

The centripetal force exerted by the contractile ring of tension T is given by Laplace's law, $\gamma = T(1/R - \partial^2 h/\partial s^2)$. Crucially, this force depends on the local curvature $\partial^2 h/\partial s^2$ of the ring, equal to the septum curvature, since the shape of the ring is the same as the shape of the septum edge, albeit separated from it by a few nanometers. From eq. 2.1 growth will be faster where the edge has large and negative curvature (troughs) and suppressed where curvature is positive (bumps). This hypothesis is consistent with reported correlations between local septum curvature and growth rate in deformed yeast cells (Zhou *et al.*, 2015). Overall, we expect that through this mechanism ring tension will tend to restore circularity.

Using this expression for the force in eq. 2.1 yields the basic equations for septum growth (see Materials and Methods)

$$\frac{\partial h}{\partial t} = D\frac{\partial^2 h}{\partial s^2} + \eta_{\text{fluc}}\,, \qquad -\frac{dR}{dt} = v_{\text{sept}}^{0} + \frac{D}{R}, \qquad D = \frac{v_{\text{sept}}^{0} T}{\gamma^{\star}}\,. \tag{2.2}$$

The first equation tells us that septum edge fluctuations h obey the diffusion equation plus a noisy source term η_{fluc}, with an effective diffusivity D proportional to the ring tension T. Thus, random growth excites septum edge fluctuations, but ring tension acts to smooth out these irregularities much like molecular diffusion smoothens density inhomogeneities in other contexts. These dynamics for h are similar to the classic Edwards-Wilkinson equation describing stochastic interfacial growth processes (Edwards and Wilkinson, 1982), with the complication that here the growing surface is curved and continuously shortening, $0 < s < 2\pi R(t)$. The second result of eq. 2.2 states that the mean constriction rate is increased due to the tension of the ring by an amount D/R, an increasingly strong effect as the ring shortens. We developed a computer simulation to implement this model on an initially circular lattice of points representing the septum edge that was evolved according to eq. 2.2 (see Materials and Methods).

Simulations close septa properly and reproduce experimental constriction curves and roughness profiles

We simulated our model using the parameter values of Table 2.1. Simulated septum edges regulated by rings with normal tension remained close to circular and achieved proper closure, constricting down almost to a point (Fig. 2.2D), while unregulated septum growth produced rough irregular edges that closed improperly (Fig. 2.2D). Fitting the mean initial slopes of simulated constriction curves to experiment (mean septum radius R versus time) we obtained the intrinsic septum growth rate v_{sept}^{0} = 72 ± 12 nm/min. With best fit parameters (see below) constriction curves showed little downward curvature in agreement with experiment, with a mean constriction rate 86 ± 3 nm/min (Fig. 2.6C, n = 428 edges from 30 constrictions) only ~20% greater than the intrinsic septum growth rate and consistent with the experimental value measured here, 80 ± 10 nm/min, and previously reported values (Pelham and Chang, 2002).

Table 2.1. Parameters used in the mechanosensitive septum growth model.

Symbol	Meaning	Value	Legend
D	Effective diffusivity	180 nm^2/s (±130 nm^2/s)	**(A)**
λ	Growth fluctuation strength	4100 nm^3/s (±2100 nm^3/s)	**(B)**
a	Correlation length of septum growth	100 nm	**(C)**
v_{sept}^0	Intrinsic septum growth rate	0.072 μm/min (±0.012 μm/min)	**(D)**
R_0	Initial radius of septum hole	1.55 μm	**(E)**
T	Tension produced by actomyosin ring	391 pN (±154 pN)	**(F)**
ρ_{bgs}	Mean density of Bgs1p at the ingressing septum edge	0.26 nm^{-1}	**(G)**
$\mu^\star$	Septum synthesis apparatus mechanosensitivity per Bgs complex	$0.15\ \mathrm{pN}^{-1}$ $(\pm 0.10\ \mathrm{pN}^{-1})$	**(H)**
w_{ring}	Width of the actomyosin ring	0.1 μm	**(I)**

Legend. Values in parentheses are standard deviations or ranges for experimentally measured values, and 95% confidence intervals for fitted parameters $(D, \lambda, v_{\mathrm{sept}}^0, \mu^\star)$.
(A) Estimated by fitting the saturation length scale x_{sat} of simulated edges to experimental measurements.
(B) Estimated by fitting the roughness profile $w(x)$ of simulated edges to experimental measurements.
(C) Assumed to be the same as the width of the ring, which was measured in Kanbe et al., 1989.
(D) Estimated by fitting model-predicted constriction rates at onset of constriction to experiment.
(E) From images of septum at onset of constriction.
(F) Measured in (Stachowiak *et al.*, 2014).
(G) Estimated from the total number of Bgs1 molecules at the inner septum edge, measured in (Proctor *et al.*, 2012).
(H) Estimated from our measurements of the diffusivity parameter D.
(I) Estimated using electron micrographs of the septum from Kanbe et al., 1989.

For each simulated constriction we calculated the roughness profile $w(x)$ of the septum edge at different times as the edge constricted over ~20 mins. As seen experimentally (Fig. 2.2A), at each time the roughness increased with length scale up to a plateau value w_{sept} at the roughness saturation length scale, x_{sat} (Fig. 2.2E, 2.6D). We used the saturation scale to extract the diffusivity parameter D: we fit the model-predicted time dependence of the saturation scale to experiment, averaged over all constrictions (n = 21 experimental and n = 30 simulated constrictions), using *D* as a fitting parameter (Fig. 2.6E). With the best fit value *D* = 180 ± 130 nm^2/s (± 95% confidence interval, Fig. 2.6E), the predicted and measured curves were in close agreement (Fig. 2.2B).

The model predicts a roughness exponent ~ 0.5 close to the experimental value

Our experiments showed a septum edge roughness exponent α = 0.47 (Fig. 2.2C). Given that our model is close to the Edwards-Wilkinson model of randomly growing interfaces, for which $w(x) \sim \sqrt{\lambda x / D}$ has an exponent α = 0.5 (Edwards and Wilkinson, 1982), we anticipated simulated septa would have a roughness exponent close to the experimental value. To test this we averaged simulated roughness profiles $w(x)$ over time and over $n = 30$ distinct constriction runs, and fit the mean profile to the averaged experimental profile with the previously determined value for *D* and using the growth fluctuation strength λ as a fitting parameter which sets the amplitude of the roughness (Fig. 2.2C). To focus on the power law regime the averaging procedure was confined to the increasing portion of each profile, in the window of length scales greater than the Bgs complex growth correlation length and the experimental pixel size, but less than the saturation scale x_{sat} (see Materials and Methods). This yielded $\lambda = 4100 \pm 2100\ \mathrm{nm}^3/\mathrm{s}$ (± 95% confidence interval, Fig. 2.6F).

With these parameter values the averaged simulated roughness profile was well described by a power law $w \sim x^{\alpha}$ with a best fit exponent α = 0.47 ± 0.04 (± 95% confidence interval, *n* = 428 edges from 30 constrictions), matching the experimental value, α = 0.47 ± 0.03 (Fig. 2.2C). Thus, our experimental results are consistent with a ring tension-mediated and curvature-sensitive mechanism that regulates local septum synthesis rates.

Consistent with experiment, simulated septum edges are nearly circular with low values of roughness

Consistent with the time dependence measured in live cells, the total roughness w_{sept} of simulated edges increased, peaked, and then decreased in time (Figs. 2.2F, 2.6G). The late time decrease occurs because the nominal value of x_{sat} then exceeds the septum length, so growth at all points is correlated and total roughness then increases with septum length. The mean time averaged simulated roughness was w_{sept} = 30 ± 10 nm (mean ± s.d.), a small fraction 4.3 ± 2.4% of the ring radius (mean ± s.d.) and consistent with the experimental value 31 ± 9 nm. The mean aspect ratio of simulated septum edges was 1.09 ± 0.10 (mean ± s.d.), close to the value of 1 for a circle and close to the experimental ratio of 1.09 ± 0.05 (Fig 2.8A). During constriction, ring tension corrected deviations from circularity by adjusting growth rates appropriately (Fig. 2.8B-F).

Contractile ring tension is sufficient to suppress septum roughness but insufficient to substantially affect constriction rates

We used the model to vary the tension over a broad interval $0 < T < 1000$ pN surrounding the value reported in live cells, $T \sim 400$ pN (Stachowiak *et al.*, 2014), for which septum roughness peaked and then decayed in time and the aspect ratio remained close to unity (Figs. 2.2D, 2.8G, 2.9A). By contrast septa closed improperly in the absence of ring tension with aspect ratios far from unity and increasing septum roughness with time. Increasing tension from zero to the physiological value decreased septum roughness ~4-fold (from 116 ± 46 nm to 30 ± 10 nm), but further increase to 1000 pN had little effect, Fig. 2.3A. Higher tensions produced constriction curves $R(t)$ with greater curvature (as expected, see eq. 2.2) that significantly exceeded the experimental value at the highest tension (Fig. 2.3B).

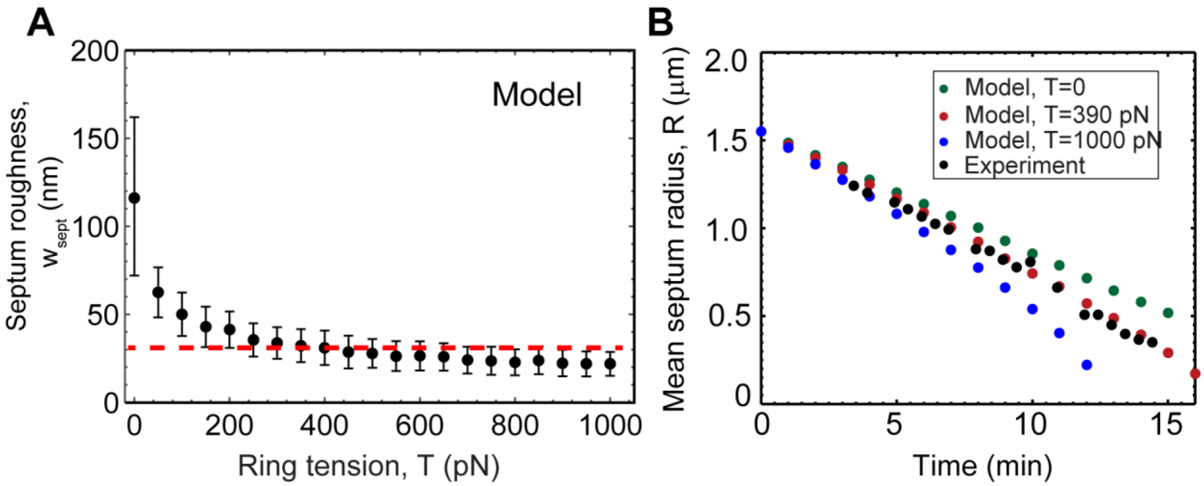

Figure 2.3. Cytokinetic ring tension is sufficient to curtail septum roughness without significantly affecting constriction rate.

(A) Mean roughness of simulated septa versus tension, fixing other parameters as in Table 2.1. Each point is the average over $n = 360$ edges from 30 constrictions. Error bars indicate s.d. Dashed line: experimental mean septum roughness from constrictions of Fig. 2.2B, averaged over constrictions and times. (B) Simulated mean septum radius versus time for three values of ring tension, compared to a typical experimental constriction.

Thus, the contractile ring tension in cells is just high enough to significantly suppress the roughness that uncorrelated septum growth would generate, yet insufficient to substantially increase the constriction rate.

Septum synthesis has a mechanosensitivity $\sim 0.1\ \mathrm{pN}^{-1}$ per Bgs complex

According to our model the suppression of septum roughness by ring tension is quantified by the "diffusivity" $D = v_{\mathrm{sept}}^{0} T/\gamma^{*}$ which depends on the ring tension T, the intrinsic septum growth rate v_{sept}^{0} and the parameter γ^{*}, the mechanical force per unit length that increases the synthesis rate of the septum-growing apparatus 2-fold. Using values for D and v_{sept}^{0} from fitting the model to experiment and the measured tension of the *S. pombe* ring (Table 2.1) gives $\gamma^{\star} = 2.61 \pm 1.89$

pN/nm, ~5 times the typical force per unit length exerted by the ring, *T/R*. This reflects the fact that ring tension has little effect on the mean constriction rate, while being sufficient to significantly affect high curvature local troughs or bumps.

If one were to assume that the leading septum edge is grown by Bgs1p alone, and estimating for simplicity that 50% of the ~8000 Bgs1 molecules (Arasada and Pollard, 2014) at the cleavage furrow localize to the edge and are active, this would give a density of active Bgs1p at the septum edge ρ_{bgs} ~ $0.4\ \text{nm}^{-1}$. Hence the mechanosensitivity for the septum synthesis apparatus on a per Bgs1 basis is $\mu^* = \rho_{\text{bgs}}/\gamma^* = 0.15 \pm 0.10\ \text{pN}^{-1}$. This represents the relative synthesis rate increase per unit force.

Ring disassembly or mutations in contractile ring components produce septa with increased roughness, shape irregularities and growth rate inhomogeneities

Since our results suggest ring tension controls local septum synthesis, we next examined the effects of disrupting the ring with mutation of three different contractile ring proteins, and LatA treatment to depolymerize actin filaments. LatA treatment and disabling of formin Cdc12 increased the roughness (Fig. 2.4C), the roughness exponents (Figs. 2.4D, 2.9C) and the aspect ratios (Fig. 2.9A) of the septum more than depletion of F-BAR Cdc15 or deletion of the IQ motifs from IQGAP Rng2 (Fig. 2.9B).

LatA treatment: We added 200 µM of the actin monomer sequestering agent Latrunculin A (LatA) to cells 2-5 min before imaging, sufficient to disassemble the F-actin ring and abolish actomyosin activity within 1 min of treatment (Pelham and Chang, 2002). LatA-treatment fragmented the contractile ring and over time the septum holes moved off center and became more irregular and increasingly slit-shaped (Fig. 2.4A), as noted previously (Zhou *et al.*, 2015).

The roughness of 149 ± 73 nm , the roughness exponent of 1.02 ± 0.10 and the aspect ratio of 1.77 ± 0.69 were all much larger than wild-type values (Figs. 2.4C,D, 2.9A).

Temperature sensitive cdc12 mutant: Contractile rings disassemble within ~4 min after shifting *cdc12-112* to the restrictive temperature (Zhou *et al.*, 2015), presumably due to loss of actin filaments. Over time at the restrictive temperature the septum edges became rougher and more elongated (Fig. 2.4A,B). Given the absence of F-actin, actomyosin activity is presumably abolished in these cells. The roughness of 73 ± 42 nm, the roughness exponent of 0.88 ± 0.07 and the aspect ratio of 1.25 ± 0.10 were above the wild-type value (Figs. 2.4C,D, 2.9A).

Rng2 mutant: We imaged *rng2Δ* cells complemented with Rng2pΔIQ, a construct of Rng2p that lacks IQ motifs ("Rng2pΔIQ") using a confocal microscope setup with a somewhat larger pixel size, 83 nm. The septa in dividing Rng2pΔIQ cells moved off center but remained almost circular and closed properly (Fig. 2.4A).The roughness of 43 ± 14 nm, the roughness exponent of 0.45 ± 0.03 and the aspect ratio of 1.09 ± 0.07 of the septa were closer to wild-type values (Figs. 2.4C,D, 2.9A).

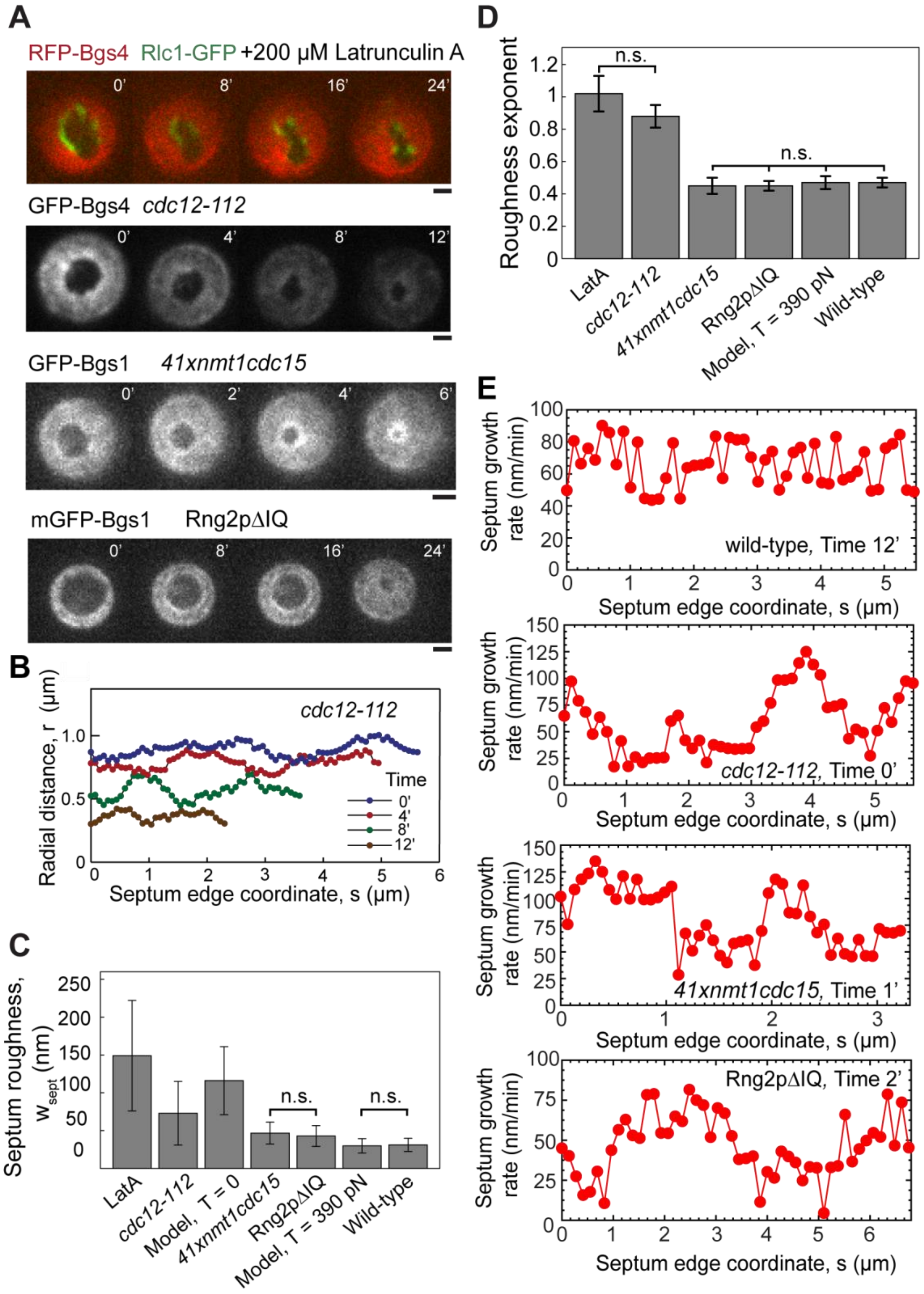

Figure 2.4. Septa with abnormal roughness, deviations from circularity and inhomogeneous growth rates in cells treated with LatA or with mutations of contractile ring proteins.

n.s. denotes that there were no statistically significant differences within the indicated group ($p > 0.05$). (A) Confocal fluorescence micrographs of division planes during constriction in a wild-type yeast cell expressing RFP-Bgs4 and Rlc1-GFP and treated with 200 μM Latrunculin A (LatA), a *cdc12-112* cell expressing GFP-Bgs4 and Rlc1-Tomato at the restrictive temperature, a *41xnmt1cdc15* cell expressing GFP-Bgs1p, Rlc1p-tdTomato and Sad1p-GFP, and a *rng2Δ* cell expressing mEGFP-Bgs1p, Sad1-RFP and complemented with Rng2pΔIQ. Times in minutes after the first frame. Scale bars: 1 µm. (B) Radial distance profiles of the septum edges in the *cdc12-112* cell of (A) at four times. (C) Comparison of mean septum edge roughness for wild type cells (Fig. 2.2B), the cases in (A), and simulations with and without tension. Roughness was calculated from constrictions of Figs. 2.2B, 2.3A, 2.9A. Error bars indicate ± s.d. (D) Comparison of septum edge roughness exponents for the same cases as (C), except for zero tension simulations. Exponents from Figs. 2.2C, 2.9B,C. Error bars denote ± 95% confidence intervals. (E) Septum growth rate versus edge coordinate s for the wild-type, *cdc12-112*, *41xnmt1cdc15* and Rng2pΔIQ cells of Figs. 2.1B and 2.4A. Growth rate is the mean value over an interval of 2 min (wild-type, *41xnmt1cdc15*) or 3 min (*cdc12-112*, Rng2pΔIQ). Growth rates of *cdc12-112, 41xnmt1cdc15*, and Rng2pΔIQ cells show large systematic spatial fluctuations, unlike the wild-type cell.

Cdc15 depletion: We grew *41xnmt1cdc15* cells under conditions that reduce amounts of the F-BAR protein Cdc15p to 15% of wild type levels. This reduces the initial rates of septum growth owing to slow delivery of Bgs1 to the division site (Arasada and Pollard, 2014). Septa in dividing *41xnmt1cdc15* cells remained almost circular and closed properly (Fig. 2.4A) with a roughness of 47 ± 15 nm, a roughness exponent of 0.45 ± 0.05 and an aspect ratio of 1.11 ± 0.06, similar to wild type cells (Figs. 2.4C,D, 2.9A).

The results of these experiments are consistent with the ring serving to control septum roughness and shape. To model septation without a functional ring we used our simulations with zero ring tension which produced a roughness similar to experiment (116 ± 46 nm, Fig. 2.4C), but with almost no dependence on length scale, as expected of independently operating septum synthesis processes (Fig. 2.9D).

We also observed that the edges of the septa in all three mutant strains and LatA-treated cells underwent large systematic variations in growth rates on a scale ~1-2 µm around the septum edge, about one quarter of the edge length (Fig. 2.4E). This behavior was manifested as high amplitude anticorrelations in the velocity correlation function on a similar scale (Figs. 2.9E,F). By contrast, in wild-type cells the velocity variations are lower and correlations are absent on scales $\gtrsim$ 0.5 μm (Figs. 2.4E, 2.9E). We also note occasional edge segments of length $\lesssim$0.5 μm that exhibited almost uniform growth rate in *cdc12-112*, wild-type, and *41xnmt1cdc15* cells.

The extended spatial variations we observe could reflect an inhomogeneous distribution of Bgs complexes related to the absence of or damage to the contractile ring, beyond the scope of our model. Indeed, previous studies showed altered Bgs localization in *41xnmt1cdc15* and Rng2pΔIQ. In *41xnmt1cdc15* cells the ring slid along the long axis of the cell until ~2000 Bgs1p molecules accumulated adjacent to the ring, and the amount of Bgs1p at the ring at the onset of constriction was ~30% lower than wild-type (Arasada and Pollard, 2014). Rng2pΔIQ cells have reduced amounts of the SIN kinase Sid2p at the division plane and altered Bgs1 distribution (Tebbs and Pollard, 2013). In LatA-treated cells, the Bgs1 distribution is anisotropic and, interestingly, spatial variations in growth rate correlate with Bgs and Rlc1p localization (Zhou et al., 2015).

Discussion

Stochastic growth produces rough interfaces

Surface growth phenomena such as crystallization and corrosion abound in nature (Hermann *et al.*, 1995; Stegemann *et al.*, 2004). Intrinsic molecular stochasticity can produce irregularities in the growing interfaces, commonly described by the roughness, the rms height fluctuation (Lapujoulade, 1994). Roughness is caused by spatial variations in growth rates that produce height differences, and is typically moderated by lateral diffusion or other smoothing effects that tend to equalize these heights. The net result is a roughness $w(x)$ that depends on length scale *x*: nearby points (small *x*) have similar heights due to diffusive smoothing, whereas more separated locations are less affected by diffusion and height differences are greater. The classic Edwards

Wilkinson (EW) and KPZ models of interfacial growth in the presence of diffusive smoothing predict a power law dependence $w(x) \sim x^{\alpha}$ with a roughness exponent $\alpha = 0.5$ (Edwards and Wilkinson, 1982; Kardar *et al.*, 1986).

Septum growth is spatially coordinated during septation in *S. pombe*

Stochastic growth also occurs in cells, as in septation during cytokinesis in fungi and bacteria when cell wall synthases grow the division septum (Pollard and Wu, 2010; Balasubramanian *et al.*, 2012), in the assembly of microtubules or actin filaments in the cytoskeleton (Desai and Mitchison, 1997; Vavylonis *et al.*, 2005) or in polymerase-mediated DNA synthesis from nucleotides (Geertsema *et al.*, 2014). In such cases molecular randomness leads to shape or length fluctuations in the assembled structures.

Here we studied septation in fission yeast mediated by glucan synthases that reside in the plasma membrane. Growing septum edges were almost circular, with small scale-dependent roughness (Fig. 2.2C). Were growth spatially uncoordinated, high roughness would be expected down to the smallest scales, and would presumably lead to improper septum closure. Given that septa close properly, and given the scale-dependent edge statistics, we concluded that septa are grown by spatially coordinated processes.

The contractile ring regulates septum roughness and directs proper septum closure

What mechanism achieves this coordination? To equalize growth rates around the septum with sufficient fidelity to maintain an almost perfectly circular septum edge would be demanding of a mechanism based on long range biochemical communication between edge locations microns apart. We proposed that septum growth rates are spatially coordinated by a robust, short-ranged mechanism that prevents edge irregularity that would otherwise result (Fig. 2.5A), based on the hypothesis that the contractile ring is mechanically coupled to the septum synthesis process. The molecular mechanism is unknown, but a conceptually simple possibility is a direct interaction with the integral membrane Bgs complexes (Fig. 2.5B). Other possibilities include stretching of the septum material to enhance synthesis rates locally.

A mathematical model showed that forces due to ring tension T then suppress roughness by adjusting growth rates by an amount depending on the local septum curvature (Fig. 2.5C), analogously to diffusive smoothing. The smoothing mechanism is quantified by a "diffusivity" parameter $D = v_{\mathrm{sept}}^{0} T/\gamma^{*}$ (eq. 2.2). The predicted roughness exponent $\alpha \sim 0.47$ was close to the EW model and experimental values (Fig. 2.2C). Simulated septa remained circular and closed without defects (Fig. 2.2D, 2.8A), and the roughness saturated in time as seen experimentally (Fig. 2.2F). These results support the hypothesis that the ring maintains circularity of the septum and its defect-free closure by regulating mechanosensitive septum synthesizing apparatus.

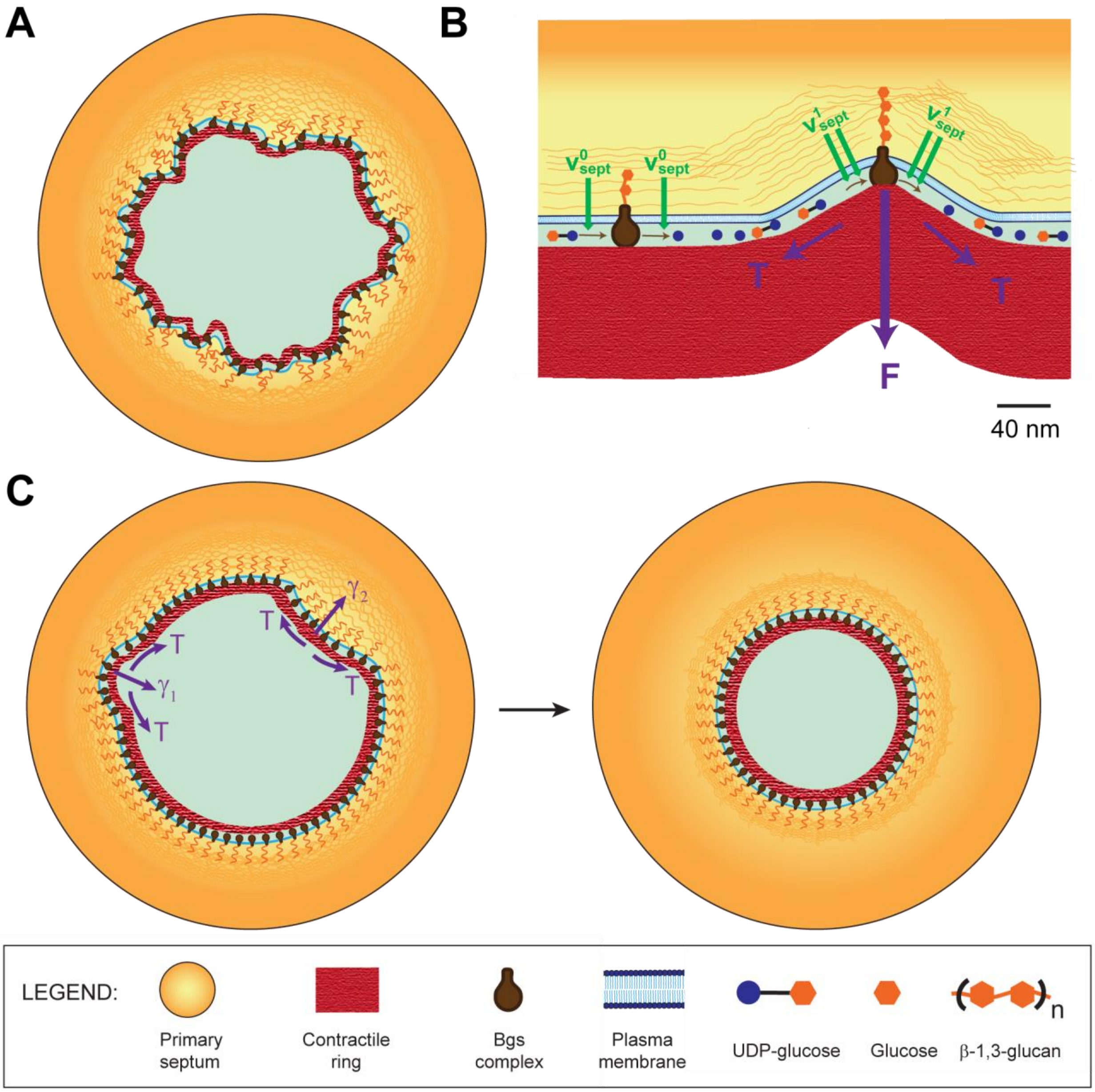

Figure 2.5. Model of septum shape regulation by cytokinetic ring tension.
UDP-glucose, glucose and β-glucan not to scale. (A) Were septum synthesis rates statistically independent around the septum, intrinsic fluctuations in local growth rates would produce irregular septum edges with high roughness. (B) Hypothetical mechanism for mechanosensitivity of septum synthesis based on direct mechanical coupling between the contractile ring (at tension *T*) and β-glucan synthase complexes in the plasma membrane. At flat locations septum is synthesized at the base rate (v^0_{sept}, left). Where curvature is high, the ring exerts force *F* on Bgs complexes, increasing the rates of polymerization and septum synthesis ($v^1_{\mathrm{sept}} > v^0_{\mathrm{sept}}$, right). (C) In the presence of the tense ring, the mechanism of (B) smoothes edges and maintains circularity. At a bump (negative curvature, right) an outward force per unit length γ_2 suppresses the rate of Bgs synthesis, while at a trough (positive curvature, left) the inward force per unit length γ_1 increases the rate of synthesis. The net effect is to reverse such deviations and restore circularity.

Mechanosensitivity of septum synthesis machinery enables shape regulation

We defined the mechanosensitivity as the rate of increase of septum synthesis rate per applied force, relative to the intrinsic rate without force. From the best fit value of the diffusivity parameter $D = 180\ \mathrm{nm}^2\mathrm{s}^{-1}$, we found a mechanosensitivity $\mu^{*} \sim 0.15\ \mathrm{pN}^{-1}$ on a per Bgs complex basis. If we assume the Bgs complexes are themselves directly affected (Fig. 2.5B), this would imply a ~ 0.15 pN^{-1} sensitivity of the synthase, considerably higher than that of another molecular polymerization machine, RNA polymerase II of *S. cerevisiae*, for which we estimate $\mu^{\star} \sim 0.01\ \mathrm{pN}^{-1}$ at saturating NTP conditions (Larson *et al.*, 2012). By contrast, the estimated sensitivities of actin polymerization regulators formin Bni1(FH1FH2)p and mDia1(FH1FH2) are somewhat greater, $\mu^{\star} \sim 1\ \mathrm{pN}^{-1}$ and $\mu^{\star} \sim 0.4 - 0.5\ \mathrm{pN}^{-1}$ respectively (Courtemanche *et al.*, 2013; Jégou *et al.*, 2013).

The role of the cytokinetic contractile ring

Our study suggests that the fission yeast contractile ring tension controls septum shape but has very little influence on the rate of constriction. A tension ~ 400 pN was measured in the contractile ring in fission yeast protoplasts (Stachowiak *et al.*, 2014), and the ring is commonly thought to drive cell division and set the constriction rate. However, such tensions are unlikely to directly mechanically affect the septum beyond negligible strains ~0.01%, given the cell wall modulus ~30 MPa (Minc *et al.*, 2009) and the ring width $w_{\mathrm{ring}} \sim 0.1$ μm (Kanbe *et al.*, 1989b). Ring bending rigidity is expected to exert even weaker forces on the septum (Stachowiak *et al.*, 2014). Thus, inward growth of the rigid septum limits the rate of constriction. Moreover, septa can complete constriction without a ring (Proctor *et al.*, 2012), and in yeast protoplasts rings constricted at variable speeds depending on the local slope of the plasma membrane, suggesting the constriction rate is not an intrinsic property of the ring (Stachowiak *et al.*, 2014).

The possibility remains that the ring tension could indirectly affect constriction rates by boosting the rate of septum synthesis. Our analysis suggests this is not so; the tension is sufficient to curtail roughness but the constriction rate is set by the rate at which septum is synthesized, little affected by ring tension (Figs. 2.2F, 2.3A,B). This originates in the incoherent nature of growth fluctuations that tend to self-cancel: during constriction the net septum area produced by fluctuations $(\lambda R_0 \tau_{\text{constrict}})^{\frac{1}{2}} \sim 0.06\ \mu\text{m}^2$ is much less than the total septum area grown $\pi R_0^2 \sim 7.5\ \mu\text{m}^2$, where R_0 is the initial radius. Thus fluctuations are relatively easily influenced. We found that the value of ring tension in cells lies within a broad window where roughness is affected but not the mean constriction rate (Figs. 2.3A, B).

If the ring tension has only a small effect on the rate of septation, why are constriction rates lower in Rng2p mutants lacking IQ motifs, in *myo2-E1* cells and in *cdc12-112* cells at the restrictive temperature (Proctor *et al.*, 2012; Tebbs and Pollard, 2013)? This may be because mutations in ring components affect septation in many ways, independently of ring tension. Indeed, Rng2p mutations resulted in fewer molecules of the Sid2p kinase (a septation initiation network kinase) in rings (Sparks *et al.*, 1999; Tebbs and Pollard, 2013), and altered the spatial distribution of Bgs1 in the cleavage furrow (Tebbs and Pollard, 2013).

The most direct evidence that the ring tension T does not accelerate septation comes from measurements in wild-type fission yeast uncomplicated by systemic effects of mutations, together with Laplace's law which dictates that the ring exerts an inward force per unit length T/R. If the mean septum growth rate were influenced by this force, constriction would accelerate dramatically as the ring radius *R* becomes small. On the contrary, experimental constriction rates are almost constant (Pelham and Chang, 2002). Experiment and modeling suggest this is not explained by decreasing ring tension as constriction proceeds, since myosin-II concentration in the ring increases (Wu and Pollard, 2005) and the predicted tension increases accordingly (Stachowiak *et al.*, 2014). Thus, in the picture emerging from our study, once the ring and septum synthesis apparatus are in place it is septum synthesis that sets the rate of constriction while the ring coordinates growth spatially to ensure proper closure.

Materials and Methods

Yeast Strains and Media

Standard methods were used for genetic manipulation and media. Strains are listed in Table 2.2. Wild-type, *cdc12-112*, and LatA-treated cells were incubated in PDMS chambers in YE media and imaged in the lab of Fred Chang (Columbia University). *cdc12-112* cells were imaged 5-10 minutes after imposition of 36 °C. Wild-type and LatA-treated cells were imaged at 25 °C. Experiments using Latrunculin A used 200 μM Latrunculin concentration, obtained by adding 20mM LatA stock to yeast cells in DMSO. LatA was added to cells 2-5 mins prior to imaging. *41xnmt1cdc15* and Rng2pΔIQ cells were incubated in PDMS chambers at 25 °C in EMM5S media and imaged in the lab of Thomas D. Pollard. Three Z slices 0.4 µm apart were acquired to cover the entire septum for wild-type, *cdc12-112*, and LatA. Six Z slices 1.8 µm apart were used for *41xnmt1cdc15* and Rng2pΔIQ cells. Images used for quantitative analysis were sum-intensity projections of these slices. Some images used in this study were provided by Z. Zhou and F. Chang, Columbia University. PDMS chambers used by them to orient cells vertically were

Table 2.2. ***S. pombe*** **strains used in this study.**

Strain	Genotype	Source
FC2561	h^+ *rlc1-GFP:kanMX bgs4::ura4+ RFP-bgs4+leu1+ leu1-32 ura4-D18 his3-D1*	Chang lab
FC2796	h^+ *rlc1-tomato:NatMX GFP-bgs4:leu1 bgs4::ura4 cdc12-112 ade6-M216 leu1-32 ura4-D18*	Chang lab
FC2809	h^- *cdc15-tomato dimer:NatMX GFP-bgs4:leu1 bgs4::ura4+ leu1-32 ura4-D18*	Chang lab
AR650	*h kanMX6-P41xnmt1-cdc15 rlc1-tdTomato-natMX6 sad1-GFP-kanMX6 bgs1Δ::ura4*$^+$ $P_{bgs1}{}^+$*::GFP-bgs1*$^+$*:leu1*$^+$ *leu1-32 ura4-D18 his3-D1 ade6-M21X*	Pollard lab
IRT 167	*leu1-32, ura4-D18, ade6-M21X, rng2Δ::natMX6, Prng2-rng2ΔIQ leu1*$^+$ *, kanMX6-Pbgs1-mEGFP-bgs1, sad1-RFP-hphMX6*	Pollard lab

developed by J. He, L. Munteanu, Z. Zhou, M. Bathe and F. Chang. The development and use of these chambers are described elsewhere (Zhou *et al.*, 2015). Imaging of *41xnmt1cdc15* and Rng2pΔIQ was performed using PDMS chambers created at Yale School of Engineering and Applied Sciences, using soft lithography techniques described in Wang and Tran, 2014. Procedures for growing and preparing *41xnmt1cdc15* and Rng2pΔIQ cells for imaging are identical to those used in Tebbs and Pollard, 2013 and Arasada and Pollard, 2014, except cells were imaged in PDMS chambers.

Microscopy and Image Analysis

Wild-type, *cdc12-112*, LatA: Images were acquired using a spinning-disc confocal (CSU10; Yokagawa) on an inverted microscope (Nikon Eclipse Ti) with a EM-CCD camera (Hamamatsu) and 100X 1.4 NA objective with a 1.5 × magnifier. The resulting images have pixel size 65.3 nm and were acquired at 5 s, 30 s, 1 min and 2 min intervals. Temperature was controlled using an objective heater (Bioptechs). Image acquisition was performed using Micromanager 1.4 (Edelstein *et al.*, 2010). *41xnmt1cdc15*, Rng2pΔIQ: Microscope setup details as in Tebbs and Pollard, 2013.

The MATLAB implementation of the Canny edge detection method was applied separately to every frame of every experimental movie, with low and high thresholds of edge detection equal to 0.1 and 0.6, and a standard deviation of $\sigma = 2.5$ pixels for the Gaussian smoothing procedure which is the first step of the Canny method (Canny, 1986). These parameters were chosen to maximize the number of successfully detected septum edges. A continuous closed boundary at the inner edge of the fluorescently-tagged Bgs4 signal is considered as a successfully detected septum edge.

We obtained best-fit circles and ellipses to septum edges using methods described in Umbach and Jones, 2003, to calculate mean radius and aspect ratio. To determine initial septum radius R_0 we used circles fit to hand drawn septum edges as edge detection failed at onset of septation. All other frames where edges could not be successfully detected were excluded from further analysis.

Calculation of septum edge roughness

The irregularity of an interface can be quantified by its roughness, the rms fluctuation in the height of the interface measured perpendicular to a reference shape. This measure is widely used in materials science (Lapujoulade, 1994). We measured the "height" of the septum as the deviation from circularity, by using best-fit circles to each septum edge as the reference shape. The "height" $h(s) = r(s) - R$, where R is the radius of the best-fit circle and $r(s)$ is the radial coordinate of the septum edge at coordinate s, where $0 \leq s \leq 2\pi R$. Here, the coordinate s is the distance around the best-fit circle. A discrete set of s values were used, corresponding to individual pixels.

For a given septum edge, roughness over the length scale x, $w(x)$, is defined as

$$w(x) = < (\delta h)^2 >_{\mathrm{x}}^{1/2} = \langle \left(\frac{1}{x} \int_{s=s_0}^{s_0+x} (r(s) - R)^2 ds \right)^{\frac{1}{2}} \rangle \qquad (2.3)$$

where angular brackets denote averaging over all portions of the septum edge of length x, i.e. averaging over s_0 values in the range $0 \leq s_0 \leq 2\pi R$. The total septum roughness w_{sept} is given by $w(x)$ evaluated at $x = 2\pi R$.

To calculate the roughness $w(x)$ averaged over many septum edges, we calculated $w(x)$ of each edge over all length scales $x \leq x_{\mathrm{sat}}$ and then grouped length scales into intervals of 80 nm. The roughness measurements were then averaged in each interval. The s.d. of length scales in each interval was too small (~10 nm) to be indicated on the Figure.

Estimation of roughness exponent

Power-law fits to roughness were performed using the Curve Fitting Toolbox of MATLAB. The upper limit for the range of scales for the fit was the last increasing data point of $w(x)$. The lower limit of scale for experimental septum edges was the first scale at which roughness was statistically different from zero. The lower limit for simulated septum edges was chosen to be sufficiently larger than the pixel size and the Bgs correlation length a (see Table 2.1).

Derivation of mathematical model of Bgs-mediated septum growth in *S. Pombe* (eq. 2.2)

Our model of septum growth proposes that the centripetal force exerted by the contractile ring, which is proportional to local curvature, is communicated to the septum synthesizing apparatus and modifies the local septum growth rate (Fig. 2.5B). The growth rate of septum at location s on the leading septum edge is given by eq. 2.1. The force exerted by the ring of tension T per unit length $\gamma(s, t)$ is proportional to the local curvature $K(s, t)$ of the leading septum edge,

$\gamma(s,t) = TK(s,t)$. Assuming the rate of change of the slope of h is much larger than h itself ($h \ll R^2\, \partial^2 h/\partial s^2$), the curvature can be expanded to leading order in h and its derivatives as $K(s,t) = 1/R - \partial^2 h/\partial s^2$. From these equations, we obtain the spatiotemporal evolution for the ingressing septum edge:

$$-\frac{\partial r}{\partial t} = \left(\frac{\partial R(t)}{\partial t} + \frac{\partial h(s,t)}{\partial t}\right) = v_{\mathrm{sept}}^{0} + \frac{D}{R} - D\frac{\partial^2 r}{\partial s^2} + \eta_{\mathrm{fluc}}(s,t). \qquad (2.4)$$

This gives the basic model equations, eq. 2.2.

The dynamics for the deviation from circularity h of eq. 2.2 are similar to the well studied Edwards-Wilkinson (EW) equation (Edwards and Wilkinson, 1982). The scale-dependent roughness, $w(x)$, of interfaces which obey EW dynamics varies with the scale of observation according to a power-law with a roughness exponent $\alpha = 0.5$ ($w \sim x^{0.5}$), for scales smaller than the system size (Nattermann and Tang, 1992), and for times much larger than a characteristic time scale τ defined by the observation scale, x, namely $\tau \sim x^2/D$ (Nattermann and Tang, 1992). This power law growth of roughness is observed up to a characteristic scale x_{sat}, which initially grows with time as $x_{\mathrm{sat}} \sim \sqrt{Dt}$, until it reaches a value that scales with the size of the system (Nattermann and Tang, 1992).

Simulation of mathematical model of Bgs-mediated septum growth

Using model parameters and the previously measured value of ring tension as input, we developed a stochastic simulation to study septum growth in cells with and without intact rings. We represented the septum edge as a one-dimensional boundary with N evenly spaced points, parameterized by their coordinate $(r_{\mathrm{i}}(t), \theta_{\mathrm{i}})$. These points move inwards in the radial direction as the septum grows inwards. All simulated edges start out as perfect circles with radius R_0

centered at the origin of the coordinate system, unless otherwise mentioned in the text. These N points are initially uniformly spaced with separation $\Delta x_0 = (2\pi R_0)/N = 40$ nm. The distance between the points decreases as the simulation proceeds. The end of one simulated constriction is defined to be the moment at which a section of the septum leading edge first lies within 20 nm of the origin of the coordinate system, i.e. $\min\big(r_{\mathrm{i}}(t)\big) = 20$ nm.

The contour of the actomyosin ring in the division plane closely follows the contour of the septum edge. The discretized version of eq. 2.4 was used for the evolution of the ingressing septum edge, where the local linearized curvature $K_i = (r_{\mathrm{i+1}}(t) + r_{\mathrm{i-1}}(t) - 2r_{\mathrm{i}}(t))/\Delta x^2$.

We used a time step of Δt = 10 ms for the simulation, and the following statistics for the fluctuation in local growth rate

$$< \eta_{\mathrm{i}}(t\,)\eta_{\mathrm{i}'}(t') >= \frac{\lambda}{a\tau} f_{\mathrm{ii}'} g\left(\frac{|t-t'|}{\tau}\right) \tag{2.5}$$

where

$$f_{\mathrm{ii}'} = \begin{cases} \left(1 - \dfrac{|i-i'|}{M}\right), & |i-i'| \leq M \\ 0, & |i-i'| > M \end{cases} \tag{2.6}$$

where $M = a/\Delta x$, and

$$g(x) = \begin{cases} 1, & x < 1 \\ 0, & x \geq 1 \end{cases}. \tag{2.7}$$

Here η_i is the growth fluctuation $\eta_{\mathrm{fluc}}(s,t)$ in eq. 2.4, evaluated at the i^{th} point around the septum edge. The parameters a and τ are a small length and time scale over which septum growth is correlated, and are related to λ according to $\lambda = v_0^2 a\tau$. The form of the correlation function given in eq. 2.5 reduces to $< \eta_{\mathrm{fluc}}(s,t)\,\eta_{\mathrm{fluc}}(s',t') >= \lambda\delta(s-s')\delta(t-t')$ in the continuous limit of vanishing grid size, for $|s - s'| \gg a$ and $|t - t'| \gg \tau$. Simulation parameters are provided in Table 2.1.

Output time intervals between edges range from 10 s to 130 s. Roughness was extracted from these edges using the same procedure as that used for experimental septum edges. All computational simulations were performed using MATLAB. Scripts can be made available upon request.

Statistical analysis

All quantitative results presented as mean ± s.d. or ± 95% confidence interval as indicated. Statistical significance was determined using Student's two-tailed t test for comparison between two independent groups. The 95% confidence intervals for exponents were calculated using the Curve Fitting Toolbox of MATLAB; the confidence intervals for the model parameters D and λ were obtained using chi-squared differences between simulation and experiment (Fig. 2.7C,D).

Appendix

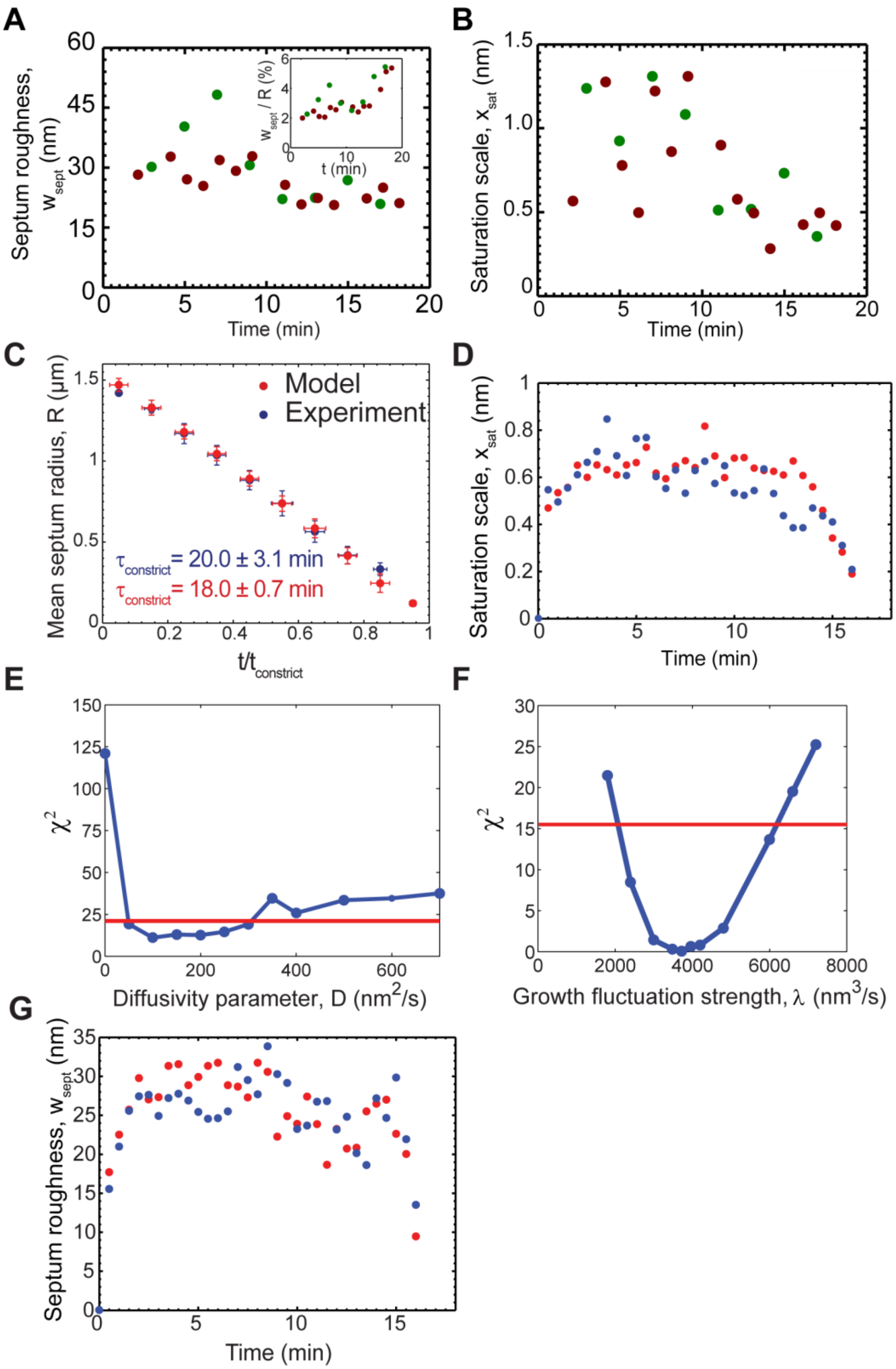
A
Septum roughness, w_{sept} (nm)
Time (min)
w_{sept} / R (%)
t (min)
B
Saturation scale, x_{sat} (nm)
Time (min)
C
Mean septum radius, R (µm)
$t/t_{constrict}$
Model
Experiment
$\tau_{constrict}$ = 20.0 ± 3.1 min
$\tau_{constrict}$ = 18.0 ± 0.7 min
D
Saturation scale, x_{sat} (nm)
Time (min)
E
χ^2
Diffusivity parameter, D (nm^2/s)
F
χ^2
Growth fluctuation strength, λ (nm^3/s)
G
Septum roughness, w_{sept} (nm)
Time (min)

Figure 2.6. Fitting procedures used to obtain best-fit parameters.

(A) Roughness of the entire edge, w_{sept}, versus time for the two constricting septa of two typical cells. The roughness decreases throughout constriction for one septum (red symbols), and for the other roughness increases, peaks and then decays (green symbols). Inset: Ratio of septum roughness w_{sept} to septum radius R versus time. Roughness is a small fraction of mean septum radius R. We synchronized the evolution of different septa versus time by assuming all septa started at the same mean radius R_0 at the onset of constriction. R_0 was calculated as the average of the initial septum radii of two cells where imaging began before the onset of constriction, as ascertained by an unchanging septum edge for the first few frames. Using this algorithm, we assigned the time to the first frame of each constriction to be equal to the time taken for the decrease in the septum hole radius to the value in the frame from R_0 at the rate of constriction of the cell. (B) Roughness saturation scale, x_{sat}, versus time for the two constrictions of Fig. 2.6A (green and red symbols respectively). (C) Mean septum radius versus scaled time for simulated and experimental constrictions of Fig. 2.2B. Time scaled with constriction time for each constriction. Scaled time bin width was 0.1. The intrinsic septum growth rate was obtained by fitting the mean initial slopes of simulated constriction curves to experiment. Mean constriction rates were 0.086 ± 0.003 µm/min (simulated) and 0.080 ± 0.010 µm/min (experiment). All values, including plotted points, are mean ± s.d. (D) Roughness saturation scale, x_{sat}, versus time for two typical simulated constrictions (red and blue symbols, respectively). x_{sat} decreases with time following a transient increase. Parameter values as in Table 2.1. (E) Chi-squared difference, χ^2, between saturation lengths, x_{sat} (defined as for Fig. 2.2A), measured from experimental and simulated septa plotted versus diffusivity parameter D. x_{sat} calculated from each septum edge was averaged across all constrictions and all times in intervals of 1 minute, from t = 6 min to 20 min for both simulation and experiment. Variance in x_{sat} due to measurement error in experiment was taken as the error in the χ^2 calculation (experiment: n = 21 constrictions, 326 edges; simulation (for each plotted value of D): n = 15 constrictions, 220 edges). Red line indicates upper bound of χ^2 beyond which simulated $w(x)$ differs from experiment in a statistically significant manner ($p < 0.05$). The best-fit estimate and the associated error of D were obtained using the mean and the width of the 95% confidence interval respectively. (F) Chi-squared difference, χ^2, between experimental and simulated mean roughness $w(x)$ versus the growth fluctuation strength λ. For each x, the mean is over all constrictions for which $x < x_{\mathrm{sat}}$ and over all times in each constriction. χ^2 was calculated in the interval $400\ \mathrm{nm} \leq x \leq 1.12\ \mu\mathrm{m}$. Variance in $w(x)$ due to measurement error in experiment was taken as the error in the χ^2 calculation (experiment: n = 326 edges, 21 cells; simulation (for each plotted value of λ): n = 428 edges, 30 cells). Red line indicates upper bound of χ^2 beyond which simulated $w(x)$ differs from experiment in a statistically significant manner ($p < 0.05$). The best-fit estimate and the associated error of λ were obtained using the mean and the width of the 95% confidence interval respectively. (G) Roughness of the septum edge, w_{sept}, versus time for two typical simulated constrictions (red and blue symbols, respectively). w_{sept} initially increases, peaks and then decreases with time.

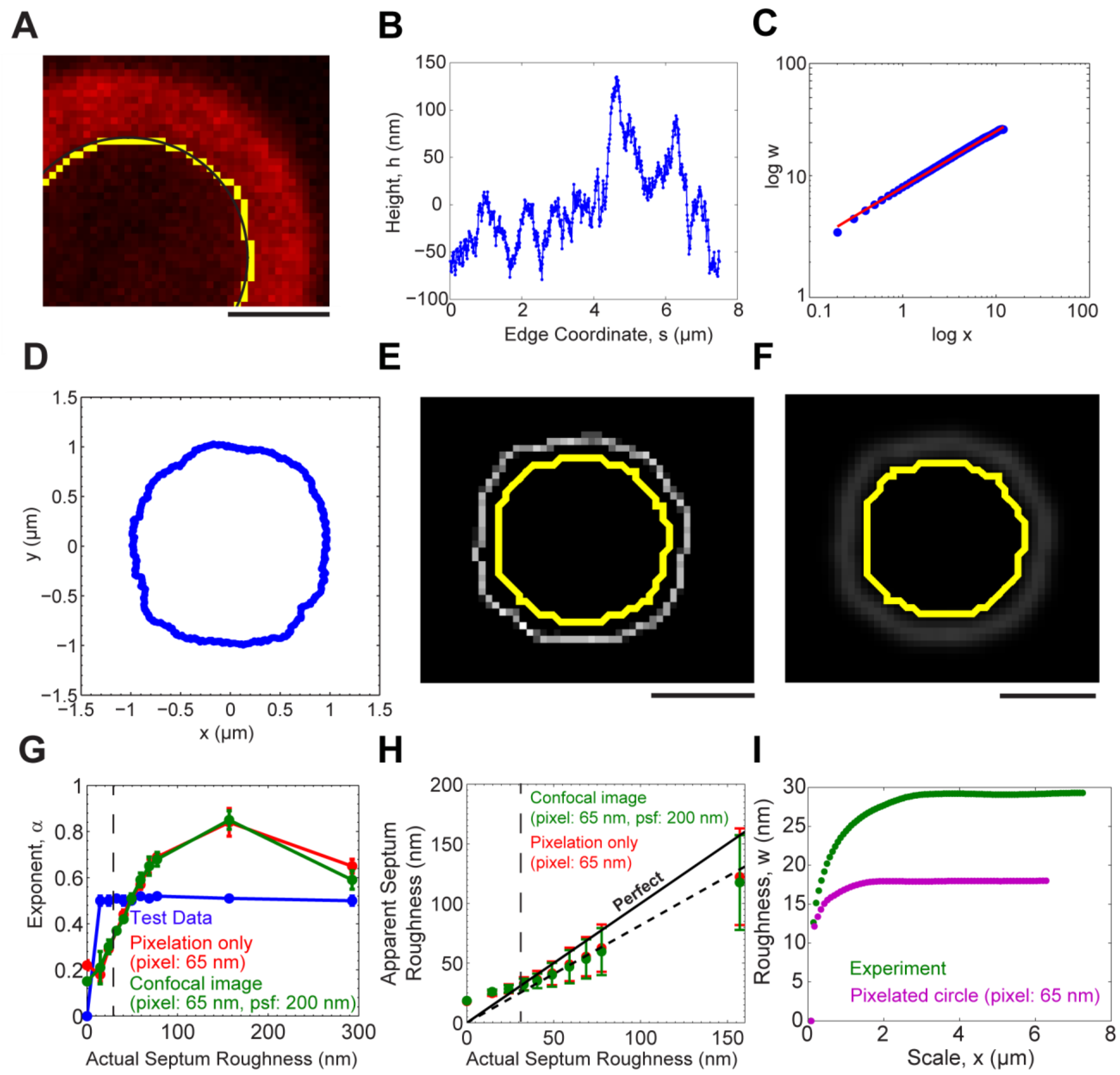

Figure 2.7. Edge detection method applied to artificially generated test edges.

(A) Enlarged section of septum edge of image in right panel of Fig. 2.1B. Yellow: detected edge. Black: best-fit circle to edge. Red: RFP-Bgs4 fluorescence intensity. (B) Typical artificial edge generated as test data for the edge detection method used in this study. Height h versus edge coordinate s for an edge of roughness 45 nm generated by numerical solution of the 1D Edwards-Wilkinson model in steady state. The initial edge is a straight line. Parameters as in Table 2.3, except $\lambda = 3.2 \times 10^4\ \mathrm{nm}^3/s$. (C) Log-log plot of roughness w versus scale x averaged over $n = 100$ edges of the type shown in (B). Best fit power law for 20 nm $\leq x \leq$ 1.2 µm has exponent 0.50 ± 0.01 (95% confidence interval). (D) The rough edge of (B) was placed on a circle of mean radius R_0=1 µm using the radial transformation $r(\theta) = R_0 + h(s)$, where $\theta = x/R_0$. (E) Grayscale pixelated image generated from edge of (D) using pixel size 65 nm (pixel intensity is proportional to length of septum edge passing through the pixel). Yellow: Result of edge detection method, identical to that used for real experimental images. (F) Simulated confocal image of (E) after convolution with a 2D Gaussian of spread 200 nm, mimicking point spread function (psf). This operation completes the mimicking of the experimental imaging method used in this study, which involved both pixelation and the effect of the confocal psf. Yellow: Result of edge detection. (G) Roughness exponents of edges from pixelated images (red) and from simulated confocal images (green) versus roughness of the test data used to generate the artificial images. Blue: true roughness exponent of test data. Mean values $\pm$ s.d. Each point represents an average over $n = 100$ edges. Simulation parameters as in Table 2.3. Vertical dashed line: experimentally measured roughness. (H) Roughness of edges from pixelated images (red) and from simulated confocal images (green) versus roughness of the test data used to generate the artificial images.

Mean values $\pm$ s.d. Each point represents an average over the same $n = 100$ edges as in (G). Vertical dashed line: experimentally measured roughness. Solid black line: Hypothetical roughness of detected edges for a perfect detection method. For large values of the actual roughness of the test data edge, the detected roughness ~ 80% of the true roughness (dashed black line). (I) Roughness *w* versus length scale *x* for a pixelated image of a perfect circle and for the real experimental edge of (A). All scale bars are 1 µm.

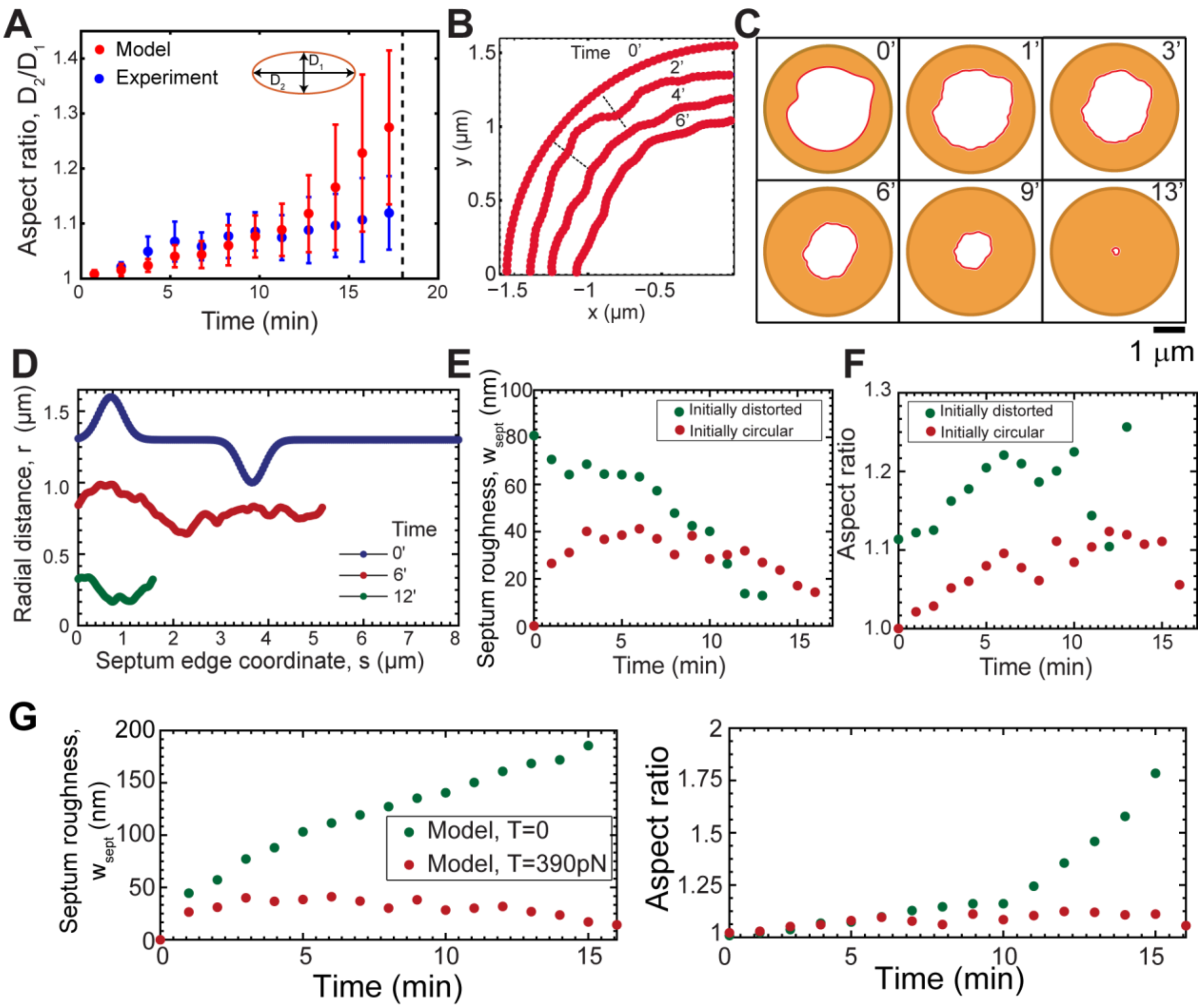

Figure 2.8. Ring tension maintains circularity of septum edges.

Model parameters are as shown in Table 2.1. (A) Aspect ratios of septum holes versus time for experimental and simulated septum edges of Fig. 2.2B (plotted points are mean ± s.d.). Dashed line: mean simulated septum constriction time, 18.0 min. Bin width 1.5 min. (B) Spontaneous high curvature shape fluctuations in simulated edges are corrected by tension-driven growth control. Portions of edges at four times during one simulated constriction are shown. A high negative curvature fluctuation (trough) at 2 min is relaxed 2 minutes later. (C) Evolution of a simulated septum edge with an artificially introduced ~300 nm bump and trough in the initial septum shape, each 500 nm wide. The septum hole recovers circularity after ~9 min. (D) Radial distance profiles for the septum edges of (C). (E) Septum roughness versus time for the simulated constrictions of Figs. 2.2D ($T = 390$ pN) and 2.8C. The decrease in roughness during the first ~8 mins of (C) is associated with the eradication of the initial bump and trough. (F) The aspect ratio of the septum edge for the simulated constriction of (C) is maintained close to unity for all time (1.18 ± 0.04, mean ± s.d., $n = 14$ septum edges), and close to the value for the simulated constriction at physiological ring tension of Fig. 2.2D (1.08 ± 0.04, $n = 17$). This shows that ring tension not only maintains global edge circularity, but also corrects local shape defects. (G) Septum edge roughness and aspect ratio versus time for the simulated constrictions of Fig. 2.2D with the previously reported ring tension of 390 pN (Stachowiak *et al.*, 2014), and without tension. Without tension roughness and the deviation from circularity always increase in time; with tension, roughness is stabilized and then decreases and circularity is maintained.

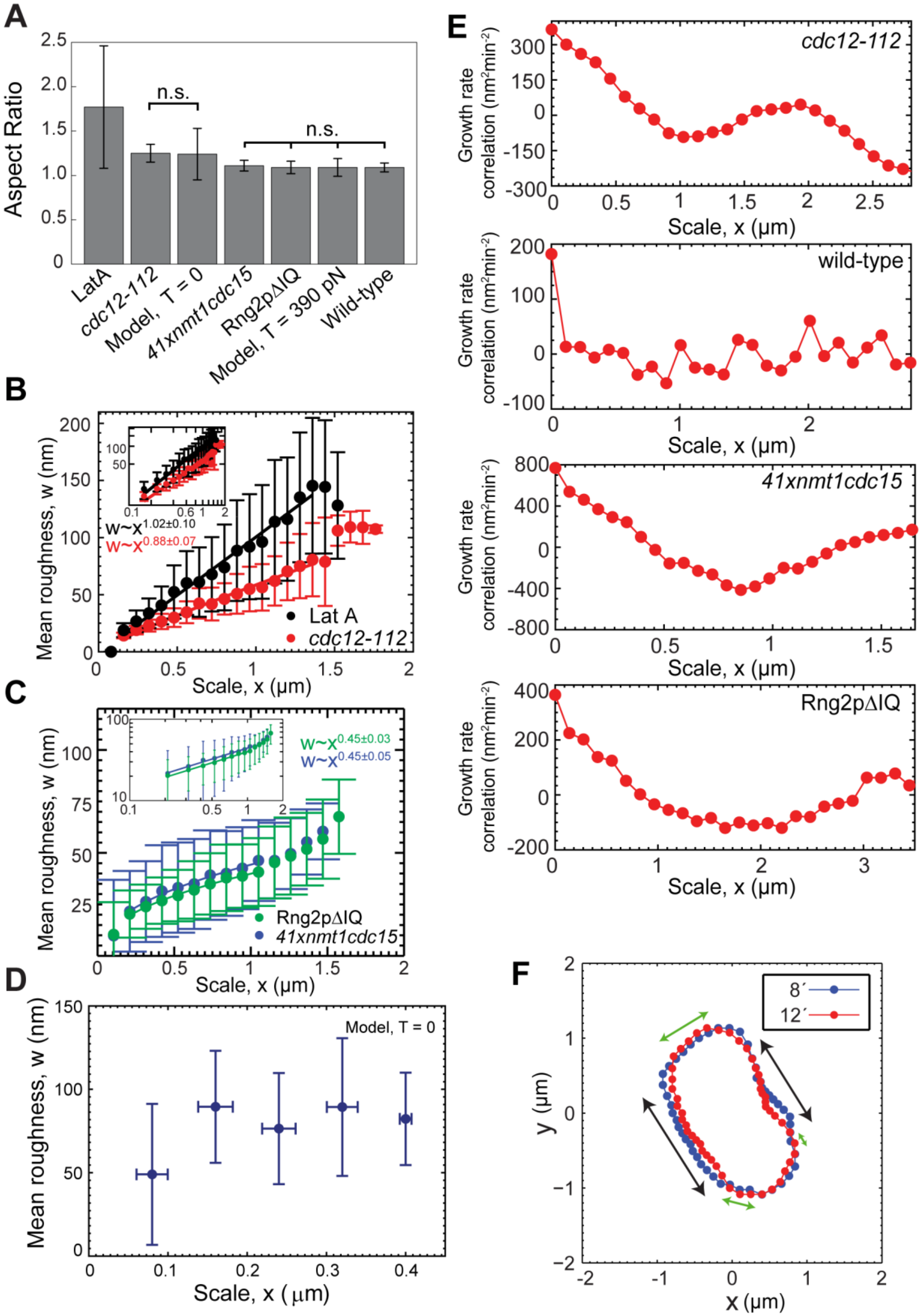
A
Aspect Ratio
2.5
2.0
1.5
1.0
0.5
0
n.s.
n.s.
LatA
cdc12-112
Model, T = 0
41xnmt1cdc15
Rng2pΔIQ
Model, T = 390 pN
Wild-type
B
Mean roughness, w (nm)
200
150
100
50
0
0
0.5
1
1.5
2
Scale, x (µm)
w~x1.02±0.10
w~x0.88±0.07
Lat A
cdc12-112
C
Mean roughness, w (nm)
100
75
50
25
0
0.5
1
1.5
2
Scale, x (µm)
w~x0.45±0.03
w~x0.45±0.05
Rng2pΔIQ
41xnmt1cdc15
D
Mean roughness, w (nm)
150
100
50
0
0
0.1
0.2
0.3
0.4
Scale, x (µm)
Model, T = 0
E
Growth rate correlation (nm2min-2)
cdc12-112
300
150
0
-150
-300
0
0.5
1
1.5
2
2.5
Scale, x (µm)
wild-type
200
100
0
-100
41xnmt1cdc15
800
400
0
-400
-800
Rng2pΔIQ
400
200
0
-200
3
F
8´
12´
y (µm)
x (µm)
2
1
0
−1
−2
-2
-1
0
1
2

Figure 2.9. Septa of cells with disassembled rings or mutations in contractile ring components have increased roughness and growth rate inhomogeneities.
(A) Mean aspect ratio of septa in LatA-treated cells (n = 21 edges, 7 cells), *cdc12-112* cells (n = 19 edges, 5 cells), simulations with zero tension (constrictions of Fig. 2.3A), *41xnmt1cdc15* cells (n = 15 edges, 4 cells), Rng2pΔIQ cells (n = 32 edges, 3 cells), in simulations with physiological tension (constrictions of Fig. 2.2B) and in wild type (Fig. 2.1F). n.s. denotes that there were no statistically significant differences within the indicated group ($p > 0.05$). Error bars are ± s.d. (B) Mean roughness of septum edges versus length scale x, averaged over all constrictions and all times for LatA-treated cells and *cdc12-112* cells of (A) including only scales $x < x_{\text{sat}}$. Best fit power laws for 160 nm ≤x≤ 1.36 μm (*cdc12-112*) and 160 nm ≤x≤ 1.36 μm (LatA) have exponents 0.88 ± 0.07 and 1.02 ± 0.10, respectively (95% confidence intervals). Inset: Log-log plots of same data. Red and black lines are the same best-fit power laws. Error bars indicate ± s.e.m. (C) Mean roughness of septum edges versus length scale x, averaged over all constrictions and all times for *41xnmt1cdc15* cells and Rng2pΔIQ cells of (A) including only scales $x < x_{\text{sat}}$. Best fit power laws for 210 nm ≤x≤ 1.05 μm (*41xnmt1cdc15*) and 210 nm ≤x≤ 1.05 μm (Rng2pΔIQ) have exponents 0.45 ± 0.05 and 0.45 ± 0.03, respectively (95% confidence intervals). Inset: Log-log plots of same data. Blue and green lines are the same best-fit power laws. Error bars indicate ± s.d. (D) Mean roughness w of septum edges versus length scale x for simulated constrictions of Fig. 2.3A with zero ring tension. For each x, the mean is over all constrictions for which $x < x_{\text{sat}}$ and over all times. Error bars denote ± s.d. (E) Growth rate correlation function for the cells of Figs. 2.1B, 2.4A versus length scale x, calculated from the growth rate curves of Fig. 2.4E. The correlation function is the normalized product of growth rate deviations from the mean for two locations separated by distance x, averaged over all such locations. For cells with compromised rings, large amplitude anticorrelations over scales ~ 1-2 μm are evident; these are absent in untreated wild-type cells. (F) Septum edges at the indicated times for the LatA-treated cell of Fig. 2.4A. Correlations in septum growth are evident over ~1 μm length scales (indicated by black arrows). Intrinsic noisiness in the edge detection method leads to negative growth in regions with little or no septum growth (green arrows).

Table 2.3. Parameters used to generate test data.

Symbol	Meaning	Value
D	Effective diffusivity	220 nm^2/s
λ	Growth fluctuation strength	$0 - 3 \times 10^6$ nm^3/s
Δx	Grid spacing used in simulation	10 nm
Δt	Time step used in simulation	50 ms
L	Length of 1D substrate	6.3 μm

Chapter 3: A node organization in the actomyosin contractile ring generates tension and aids stability

Introduction

During cytokinesis, the tensile actomyosin ring provides force that drives or guides division of the cell into two (Schroeder, 1972; Fujiwara and Pollard, 1976; Mabuchi and Okuno, 1977). Tension production is thought to be the primary role of the ring, and is thought to arise from forces exerted on actin filaments by non-muscle type-II myosin in the ring (Schroeder, 1975). However the mechanism of tension production has not been settled.

A natural candidate for the tension production mechanism is a sliding filament mechanism similar to that in striated muscle, based on the sarcomere repeat unit (Schroeder, 1975). However for fission yeast, the subject of the present study, little evidence supports a sarcomeric-like organization in the cytokinetic ring (Kanbe *et al.*, 1989a; Bezanilla and Pollard, 2000; Kamasaki *et al.*, 2007; Laplante *et al.*, 2015; Courtemanche *et al.*, 2016).

In the case of the fission yeast *Schizosaccharomyces pombe*, there is a real prospect of establishing realistic, detailed models of the cytokinetic ring, because many participating molecules have been identified (for a review, see Pollard and Wu, 2010b) and their numbers measured during ring assembly, the maturation phase, and the actual constriction of the ring (Wu and Pollard, 2005; Courtemanche *et al.*, 2016). Ring tensions of ~ 400 pN were also recently measured in fission yeast protoplasts, and a molecularly detailed simulation constrained by the considerable body of experimental data about the fission yeast ring was able to reproduce the measured values of tension (Stachowiak *et al.*, 2014).

Despite the abundance of information about the *S. pombe* ring, little was known about the organization of components in the matured, constricting ring. The organization of a number of key proteins is clearer during the process of ring assembly. The type-II myosin Myo2 and the actin nucleator formin Cdc12, among other proteins, are organized into plasma membrane-anchored protein complexes called nodes that assemble into a tight contractile ring from a broad band at the cell's equator (Wu *et al.*, 2006; Vavylonis *et al.*, 2008).

Important new information about the detailed organization in the constricting *S. pombe* ring was recently provided by a study using super-resolution fluorescence photoactivation localization microscopy (FPALM) (Laplante *et al.*, 2016). It was found that a membrane-anchored node-like organization of formin, myosin-II and other proteins persists beyond assembly into the constricting ring, and the stoichiometric ratios of molecules in the nodes were measured. Since formin caps actin filament barbed ends, this suggests an organization in which actin filament barbed ends and myosin-II colocalize and are anchored to the plasma membrane.

Here we develop a coarse-grained mathematical model of the constricting fission yeast cytokinetic ring which incorporates this recently established organizational information. In the model, formin and myosin-II are anchored to the membrane in nodes as seen experimentally, and the stoichiometry of components in the ring is fixed by experiment (Wu and Pollard, 2005; Laplante *et al.*, 2016). The model explains the origin of the observed bidirectional motion of nodes in the constricting ring, explains how tension arises from a disordered organization and generates values of ring tension close to experimentally measured values for realistic values of the force per myosin head. We find that the actomyosin contractile ring has an intrinsic contractile instability that is controlled by turnover and by anchoring of components to the membrane. The anchoring resists lateral sliding and thereby retards the instability growth rate.

Results

Mathematical model of the *S. pombe* cytokinetic ring: background

Our aim is to construct and analyze a coarse-grained mathematical model able to explore some essential consequences of the recently discovered ultrastructure of the fission yeast ring (Laplante *et al.*, 2016). In that study, FPALM super-resolution microscopy revealed that in the constricting ring the non-muscle myosin-II Myo2 and the actin nucleator and polymerizer formin Cdc12 colocalize in membrane-anchored nodes, together with the IQGAP Rng2 and the F-BAR protein Cdc15. The authors argued that there are 8 Myo2 dimers per node, unchanged from the number of Myo2 dimers in assembly nodes, the precursor nodes from which the ring is assembled. Previously, quantitative fluorescence microscopy had measured a mean of 1500 Myo2 dimers and 180 Cdc12 dimers in the ring at the onset of constriction (Wu and Pollard, 2005; Courtemanche *et al.*, 2016). This suggests that, at the onset of constriction, the cytokinetic ring contains ~190 "constriction" nodes, each containing 8 Myo2 dimers and a mean of approximately 1 formin Cdc12 dimer. Since Cdc12 dimers processively cap actin filament barbed ends while elongating the filament (Kovar *et al.*, 2006), each node would contain a mean of one actin filament anchored at its barbed end.

Thus motivated, in our simplified model the ring at the onset of constriction contains 190 nodes anchored to the plasma membrane, each node containing one formin dimer from which emanates one actin filament (Fig. 3.1A). Thus, actin filament barbed ends and Myo2 dimers are anchored to the membrane. For simplicity we neglect fluctuations in the number of formins (and hence actin filaments) per node. Further, we assume that all actin filaments are barbed-end-capped by formin Cdc12, so there are 190 actin filaments in the ring.

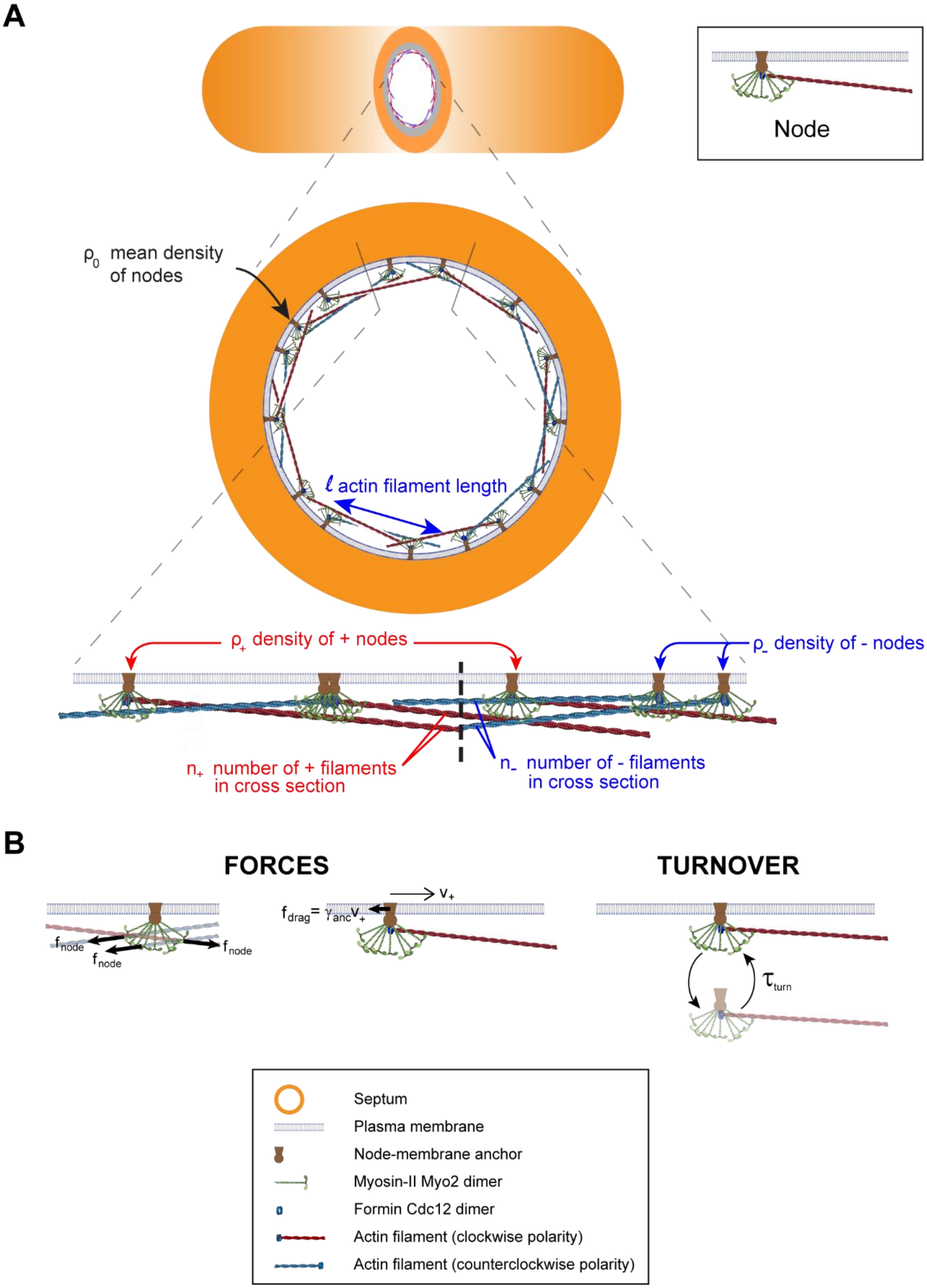

Figure 3.1. Mathematical model of the constricting fission yeast cytokinetic ring.

(A) Schematic of our coarse-grained, one dimensional mathematical model of the constricting cytokinetic ring (not to scale). The ring contains membrane anchored cytokinetic nodes (inset), protein assemblies where 8 Myo2 dimers and a formin Cdc12 dimer are attached to each other and to the node anchor that can slide along the membrane. Each node contains one actin filament of length l which is attached to the formin Cdc12 dimer at its barbed end. Nodes are referred to as clockwise (+) or counterclockwise ($-$) depending on the polarity of the attached filament, shown as red and blue, respectively. The ring is attached to the plasma membrane at the leading edge of the septum. The model describes the ring using one-dimensional continuous density fields. (B) Forces and turnover rules in the model. Myosins of a given node bind and pull every actin filament that passes through the node with a pulling force f_{node} per filament. Actin filaments experience force f_{node} per node from every node that falls along their lengths (left). As nodes slide laterally along the membrane with velocity v_{+}, they experience drag forces f_{drag} per node from membrane with a node anchor drag coefficient γ_{anc} (center). Nodes bind and unbind the membrane on a time scale τ_{turn} (right). We assume that nodes turnover with their attached actin filaments.

Another critical characteristic is the amount of actin in the fission yeast ring. A recent study counted 190,000 actin subunits at constriction onset, using the fluorescently tagged actin binding protein mEGFP–LifeAct (Courtemanche *et al.*, 2016). This translates to a mean actin length of 2.7 μm per node, given an F-actin axial rise of 2.7 nm per subunit (Carlier, 1991). For simplicity, our model assumes all actin filaments have the same length, the mean value of $l = 2.7$ μm. As the ring thickness and width of ~125 nm (Laplante *et al.*, 2016) are much less than the actin filament length, to a very good approximation a node-attached filament lies parallel to the ring and can point in either a clockwise or counter-clockwise direction along the ring (Fig. 3.1A).

Turnover times of key proteins in the fission yeast ring have been reported, including Cdc12 (43 s), Myo2 (18.6 s), and myosin-II regulatory light chain Rlc1 (41 s) (Clifford et al., 2008; Yonetani et al., 2008; Sladewski et al., 2009). The precise nature of turnover in the ring is unknown, but we assume whole-node turnover in a representative time $\tau_{\text{turn}} = 18.6$ s matching the reported Myo2 turnover time. Thus, actin turns over as whole filaments only. For simplicity our model neglects other turnover pathways, namely formin-mediated polymerization and cofilin-mediated depolymerization (Kovar *et al.*, 2006; Michelot *et al.*, 2007).

Turnover is represented by stochastic association and disassociation of nodes to and from the ring, with mean dissociation time $\tau_{\text{turn}} = 18.6$ s and a mean association rate that produces a mean of 190 nodes in the ring. We assume that formin-mediated nucleation of actin filaments is also directionally stochastic similarly to nodes during ring assembly (Vavylonis *et al.*, 2008), so that a newly arriving node produces a filament that randomly points in either the clockwise or counterclockwise direction. We refer to nodes as clockwise or counterclockwise, depending on the polarity of the attached filament. On average, there are equal numbers of each type of node but the numbers of each fluctuate in time.

The actomyosin ring consists of the bundled actin filaments and Myo2 associated with the 190 nodes (Fig. 3.1A), anchored to the membrane by the node-membrane anchors. Thus, an actin filament of length l belonging to a given node passes near the Myo2 dimers of all nodes within a distance l along the ring. These Myo2 molecules bind and exert pulling force on the filament and hence the node, resisted by the drag of the node anchor in the membrane. The anchor drag coefficient is γ_{anc} (Fig. 3.1B). These forces will pull nodes clockwise or counterclockwise, depending on the node type. Consistent with this, FPALM measured clockwise and counterclockwise motions of myosin in the ring, with a mean speed 22 nm s^{-1} (Laplante *et al.*, 2016). This supports our inference that on average there is one formin dimer and one actin filament per node, and that there are two classes of node.

Derivation of model equations

The above somewhat simplified representation of the fission yeast cytokinetic ring, severely constrained by experimental data, consists of 190 clockwise or counterclockwise nodes anchored to the plasma membrane. We developed a coarse-grained continuous mathematical description of this system. Our principle goals are to establish the mechanism of tension generation in the ring, to compare predictions of our model with experimentally measured values of tension (Stachowiak *et al.*, 2014), to explore how the ring maintains structural stability and to understand the functional significance of the two types of node motion, clockwise and counterclockwise.

We use a coarse-grained, continuous representation of the nodes. The density and velocity of clockwise nodes at time t and location x along the ring are denoted $\rho_+(x,t)$ and $v_+(x,t)$, respectively. For counterclockwise nodes the same quantities are $\rho_-(x,t)$ and $v_-(x,t)$. The total length of the fission yeast ring at constriction onset is 11.8 μm, so that $0 \leq x \leq 11.8$ μm (Fig. 3.1). Throughout, x represents the clockwise distance around the ring. Thus a positive (negative) velocity or force acts in the clockwise (counterclockwise) direction.

Consider first a typical clockwise node. The forces acting on a given node are: (i) the reaction force $F_{\text{node}}^{\text{total}}$ to the total force exerted by the myosins of that node that bind and pull actin filaments passing through it (note that the statistics of $F_{\text{node}}^{\text{total}}$ are the same for clockwise and counterclockwise nodes); (ii) the total force $F_{\text{fil},+}^{\text{total}}$ exerted by myosins of other nodes on the filament attached to that node; and (iii) the drag force exerted by the membrane that resists the lateral sliding of the node anchor, characterized by anchor drag coefficient γ_{anc} (Fig. 3.1B). The force balance reads

$$\gamma_{\text{anc}} v_+ = F_{\text{node}}^{\text{total}} + F_{\text{fil},+}^{\text{total}}. \tag{3.1}$$

Many actin filaments of both polarities pass through this node. The net myosin force exerted by that node on these filaments $F_{\text{node}}^{\text{total}}$ is proportional to the difference between the number of clockwise n_+ and counter-clockwise n_- filaments in the cross-section of the ring at the location of the node (Fig. 3.1B)

$$F_{\text{node}}^{\text{total}} = f_{\text{node}}(n_- - n_+),\ n_+ = \int_{x-l}^{x} \rho_+ dy\,,\ n_- = \int_{x}^{x+l} \rho_- dy. \tag{3.2}$$

Here, f_{node} is the time-averaged force exerted by the myosins of one node on one filament passing through it. Note that since each node carries one actin filament of length l, n_+ (n_-) equals the number of nodes within a distance l of the node in question, measured in the clockwise (counterclockwise) direction. The force acting on the node-attached actin filament is due to all nodes along its length (Fig. 3.1B),

$$F_{\text{fil},+}^{\text{total}} = \int_{x}^{x+l} f_{\text{fil},+}(y)\, dy,\ f_{\text{fil},+}(y) = f_{\text{node}}\big(\rho_+(y,t) + \rho_-(y,t)\big). \tag{3.3}$$

Here, $f_{\text{fil},+}(y)$ is the force per unit length experienced by a clockwise filament due to the pulling forces by myosins at y.

The evolution of the density is determined by the node velocities and turnover processes:

$$\frac{\partial \rho_+}{\partial t} + \frac{\partial}{\partial x}(\rho_+ v_+) = \frac{\rho_0/2 - \rho_+}{\tau_{\text{turn}}}. \tag{3.4}$$

Here $\rho_0 = 16.1\ \mu\text{m}^{-1}$is the mean number density of nodes, so that $\rho_0/2$ is the mean number of clockwise nodes. The right hand side of eq. 3.4 describes association and dissociation that maintains a mean density ρ_0 over the time τ_{turn} (Fig. 3.1B).

Eqns. 3.1-4 describe the dynamics of clockwise (+) nodes. Similar equations are obtained for the counterclockwise $(-)$ nodes, by replacing $\rho_+(x,t)$, $v_+(x,t)$ with $\rho_-(x,t), v_-(x,t)$, and replacing the filament length l by $-l$ in eq. 3.3 (eqns. 3.18-3.21, Materials and Methods).

The parameters γ_{anc} and f_{node} are obtained as best-fit parameters by comparison of model predictions with experiment (Table 3.1). We solved eqns. 3.1-3.4 and 3.18-3.21 numerically and analytically with periodic boundary conditions.

Table 3.1. Parameters of the mathematical model of the *S. pombe* cytokinetic ring

Symbol	Meaning	Value	Legend
ρ_0	Steady-state total density of nodes at onset of constriction	16.1 μm^{-1}	**(A)**
l	Length of F-actin per node at the onset of constriction	2.7 μm	**(A)**
f_{myo}	Force exerted by one Myo2 head	1.11 ± 0.43 pN	**(B)**
f_{node}	Force exerted by one node on one filament that passes through it	0.41 ± 0.16 pN	**(B)**
γ_{anc}	Membrane drag coefficient of the node anchor	810 ± 370 pN s μm^{-1}	**(B)**
τ_{turn}	Turnover time of nodes	18.6 s	**(C)**
L_0	Initial length of the ring	11.8 μm	**(D)**
f_{rep}	Repulsive force between nodes	0.1 pN	**(E)**
b_{rep}	Range of node repulsive force	0.1 μm	**(E)**
v_{myo}^0	Load-free velocity of myosin Myo2	240 nm s^{-1}	**(F)**
-	Ring tension	391 ± 154 pN	**(G)**
-	Myosin-II Myo2 node velocity	22 ± 10 nm s^{-1}	**(H)**

Legend: Errors are standard deviations (SDs) for experimentally measured values and calculated parameters.

- **(A)** Calculated from the experiments of (Pelham and Chang, 2002; Wu and Pollard, 2005; Courtemanche *et al.*, 2016; Laplante *et al.*, 2016).
- **(B)** Obtained in this study. Associated error is due to uncertainty in prior experimental measurements of node velocity and ring tension.
- **(C)** Obtained from fluorescence recovery after photobleaching (FRAP) experiments on YFP-Myo2 in constricting rings as measured in (Sladewski *et al.*, 2009).
- **(D)** Measured using fluorescence microscopy on GFP-Cdc4 (Pelham and Chang, 2002).
- **(E)** Chosen such that the final mean cluster width after aggregation was ~150 nm (Materials and Methods).
- **(F)** Obtained from gliding filament assays of (Stark *et al.*, 2010) as described in Appendix.
- **(G)** Obtained from tension measurement experiments in (Stachowiak *et al.*, 2014).
- **(H)** Obtained from FPALM myosin Myo2 node velocity measurements in (Laplante *et al.*, 2016).

Expression for f_{node}, the mean force exerted by a node on one actin filament

The net force exerted by a node on one filament passing through it, f_{node}, is a collective time-averaged force due to the individual pulling forces exerted by the 16 myosin Myo2 heads of the node. It is related to the instantaneous force f_{myo} that an individual myosin-II head exerts on an actin filament that it binds, as follows.

Now the mean number of filaments of each polarity passing through a given node is given by

$$\overline{n_+} = \overline{n_-} = \frac{\rho_0}{2} l. \tag{3.5}$$

The total force exerted by the 16 myosin heads belonging to this node, equal to 16 f_{myo}, is divided equally among these filaments, so that

$$f_{\text{node}} = 16 f_{\text{myo}} / (\overline{n_+} + \overline{n_-}). \tag{3.6}$$

Thus, the force exerted by a node on a filament passing through it depends on the number of myosin heads in the node, but also on the mean number of filaments passing through it.

The steady state ring consists of two contra-rotating families of nodes

By inspection of eqns. 3.1-3.4, 3.18-3.21 it is simple to see that a steady state solution is the homogeneous ring with equal numbers of clockwise and counterclockwise filaments and constant total node density ρ_0,

$$\rho_+(x,t) = \rho_-(x,t) = \rho_0/2. \tag{3.7}$$

Substituting eq. 3.7 into eqns. 3.2, 3.3, 3.19, and 3.20 gives

$$n_+ = n_- = \frac{\rho_0}{2} l,\ F_{\text{node}}^{\text{total}} = 0,\ F_{\text{fil},+}^{\text{total}} = f_{\text{node}} \rho_0 l,\ F_{\text{fil},-}^{\text{total}} = -f_{\text{node}} \rho_0 l. \tag{3.8}$$

eq. 3.8 states that the steady state ring has net polarity zero; thus the total myosin force exerted by a node $F_{\text{node}}^{\text{total}}$ is zero, as the myosins of that node pull on as many clockwise as counterclockwise filaments passing through the node. The only unbalanced force on a node is the force on its own actin filament $F_{\text{fil},\pm}^{\text{total}}$ due to pulling by myosin in the $\rho_0 l$ nodes that the filament of length l passes through. This force is balanced by the drag force on the node membrane anchor. eq. 3.1 yields the velocities of each node family (Fig. 3.2),

$$v_+(x,t) = -v_-(x,t) = v_0 = \frac{\rho_0 f_{\text{node}} l}{\gamma_{\text{anc}}}. \tag{3.9}$$

The two families move with speed v_0 in opposite directions, i.e. they contra-rotate. Comparing this predicted speed with the experimental node speed of 22 ± 10 nm s^{-1} (Laplante *et al.*, 2016) and using the parameter values in Table 3.1, we obtain a membrane anchor drag coefficient $\gamma_{\text{anc}} = 810 \pm 370$ pN s μm^{-1} (mean ± SD).

The model explains the observed bidirectional motions of nodes (Laplante *et al.*, 2016). The origin of the contra-rotation is that + nodes are pulled clockwise because their filaments point clockwise and are pulled clockwise by myosins, while the – nodes are similarly pulled counterclockwise. This is also consistent with other confocal microscopy measurements of myosin-II motions in *S. pombe* (Wollrab *et al.*, 2016).

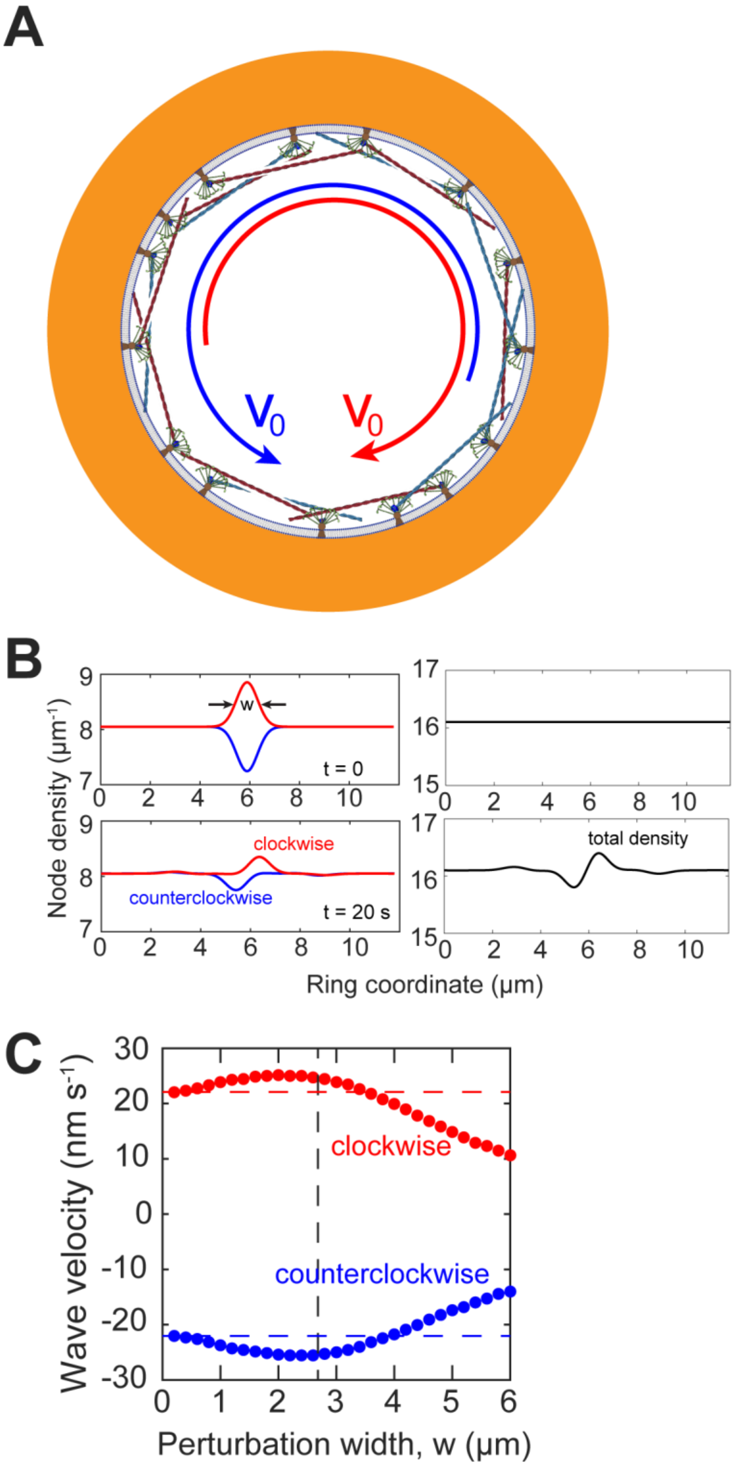

Figure 3.2. Actin and myosin in nodes contra-rotate around the steady state cytokinetic ring. Model parameters as in Table 3.1. (A) Schematic of node motions in the steady state ring. The motions of the clockwise (red filament) and counterclockwise (blue filament) nodes are indicated by curved arrows of respective colors. All nodes move at the same speed $v_0 = 22\ \mathrm{nm\ s^{-1}}$. (B) Density profiles of each type of nodes (left) and of the total density profile (right) at t = 0 and 20 s. Initial composition fluctuation had a Gaussian profile with a relative amplitude 5% and a full width half maximum w of 1 μm (black arrows). Over 20 s, perturbations travelled with a mean velocity $23\ \mathrm{nm\ s^{-1}}$. The amplitudes of both perturbations

decreased by 63% over 20 s, approximately the turnover time $\tau_{\text{turn}} = 18.6\ s$. (C) Density wave velocities versus perturbation full width at half-maximum w. Initial condition as in (B) but with a varying w. Velocities are calculated by the displacement of the peak of perturbation between 10 s and 20 s. Vertical dashed line: actin filament length $2.7\ \mu\text{m}$. Horizontal dashed lines: node velocity $\pm v_0$ in the steady state homogeneous ring. Magnitudes of cluster velocity of either type of cluster are approximately equal at every width w.

Node composition fluctuations generate contra-propagating density waves of myosin-II and other node components

What are the experimentally measurable consequences of the contra-rotating node families? Super-resolution microscopy can pick up individual node motions, but more commonly a collective fluorescence intensity distribution around the ring is measured. This intensity distribution represents the density of labelled molecules of one type, convoluted with a point spread function due to optical resolution limits.

Among the most common fluorescence microscopy measurements in the cytokinetic ring is time-lapse imaging of tagged heavy or light chain myosin-II molecules. To see how the contra-rotating node families would manifest themselves in such images, consider a local node composition fluctuation producing a surfeit of + nodes (say) over – nodes. Such fluctuations are inevitable, and will constantly occur in the stochastic ring. Let us follow the fate of a simple Gaussian-shaped composition fluctuation of relative amplitude 5% and full width at half maximum of w (Fig. 3.2B).

Numerically solving eqns. 3.1-3.4, 3.18-3.21, for a range of widths, $0.2\ \mu\text{m} \leq w \leq 6\ \mu\text{m}$, we obtained the time course of the total density profile (that would be measured in conventional fluorescence microscopy), as well as the density profile of each type of node and the associated velocities (Materials and Methods). The evolution of such a composition fluctuation of width $1\ \mu\text{m}$ is shown in Fig. 3.2B.

The result of such composition fluctuations is that two waves are generated in the total density field $\rho(x,t)$, travelling in opposite directions and associated with each node type. One wave is a translating surfeit pulse, and the other a translating deficit pulse (Fig. 3.2B). The wave speed depends on the width of the perturbation w. Narrow initial fluctuations ($w \ll l = 2.7$ µm) move at $\sim v_0 = 22$ nm s^{-1} whereas broader initial fluctuations generate waves that move more slowly, with a velocity that decreases with w (Fig. 3.2, B and C). For example, a perturbation of width 6 µm generates waves moving at 10 nm s^{-1}. The amplitude of the pulses decays over 20 s, approximately the turnover time $\tau_{\text{turn}} = 18.6$ s (Fig. 3.2B). These findings suggest the homogeneous ring is stable to small composition fluctuations, which we also demonstrated analytically (see Appendix).

These results show that node composition fluctuations generate clockwise and counterclockwise density waves moving in opposite directions. Thus, we predict that the experimental intensity distribution of Myo2, which is associated with the nodes, exhibits intensity waves of this type, a direct reflection of the two contra-rotating node families.

Tension is generated in the cytokinetic ring by myosin pulling on barbed-end anchored actin filaments

In this section we calculate the steady state ring tension predicted by the model, and we compare to experimental values measured in fission yeast protoplasts (Stachowiak *et al.*, 2014). We start form the tension profile along the length of a clockwise filament, $T_{\text{fil},+}(y)$, given by

$$T_{\text{fil},+}(y) = \int_y^l f_{\text{fil},+}(z)\, dz. \tag{3.10}$$

Here, $f_{\text{fil},+}(y)$ is the force per unit length experienced by the clockwise filament (eq. 3.3) due to myosins at location y along the filament. Using the fact that in steady state $\rho_+ = \rho_- = \rho_0/2$, eq. 3.3 yields $f_{\text{fil},+} = f_{\text{node}}\rho_0$. Using this expression in eq. 3.10 gives $T_{\text{fil},+} = f_{\text{node}}\rho_0(l - y)$, showing that the tension is highest at the anchored barbed end and decreases linearly to zero at the pointed end (Fig. 3.3A). Thus the mean tension along the filament length is

$$\bar{T}_{\text{fil},+} = \frac{1}{2} f_{\text{node}}\rho_0 l. \tag{3.11}$$

Each of the many filaments in the ring cross-section has the same mean tension in a homogeneous ring, so the net ring tension is $T_{\text{ring}} = (\overline{n_+} + \overline{n_-})\bar{T}_{\text{fil},+}$, or

$$T_{\text{ring}} = \frac{1}{2} f_{\text{node}}\rho_0^2 l^2 = 8 f_{\text{myo}}\rho_0 l. \tag{3.12}$$

after using eqns. 3.6, 3.8. This is our final expression for the tension in terms of f_{myo}, the force per Myo2 head.

Let us now compare this prediction with the measured ring tension in *S. pombe* protoplasts of 391 ± 154 pN (Stachowiak *et al.*, 2014). Using the experimentally measured mean number of actin filaments in the cross-section of the *S. pombe* ring, $\rho_0 l \approx 44$ (see Table 3.1), eq. 3.12 then yields $f_{\text{node}} = 0.4 \pm 0.2$ pN, and a myosin-II force per head of f_{myo} =1.1 ± 0.4 pN (mean ± SD).This value is similar to reported stall forces ~0.6 pN and ~0.8 pN per head for turkey gizzard smooth muscle myosin-II and chicken pectoralis skeletal muscle myosin-II, respectively (Tyska *et al.*, 1999). Using the above value for f_{node} in eq. 3.11 gives an average tension per filament of 8.9 pN (Fig. 3.3A).

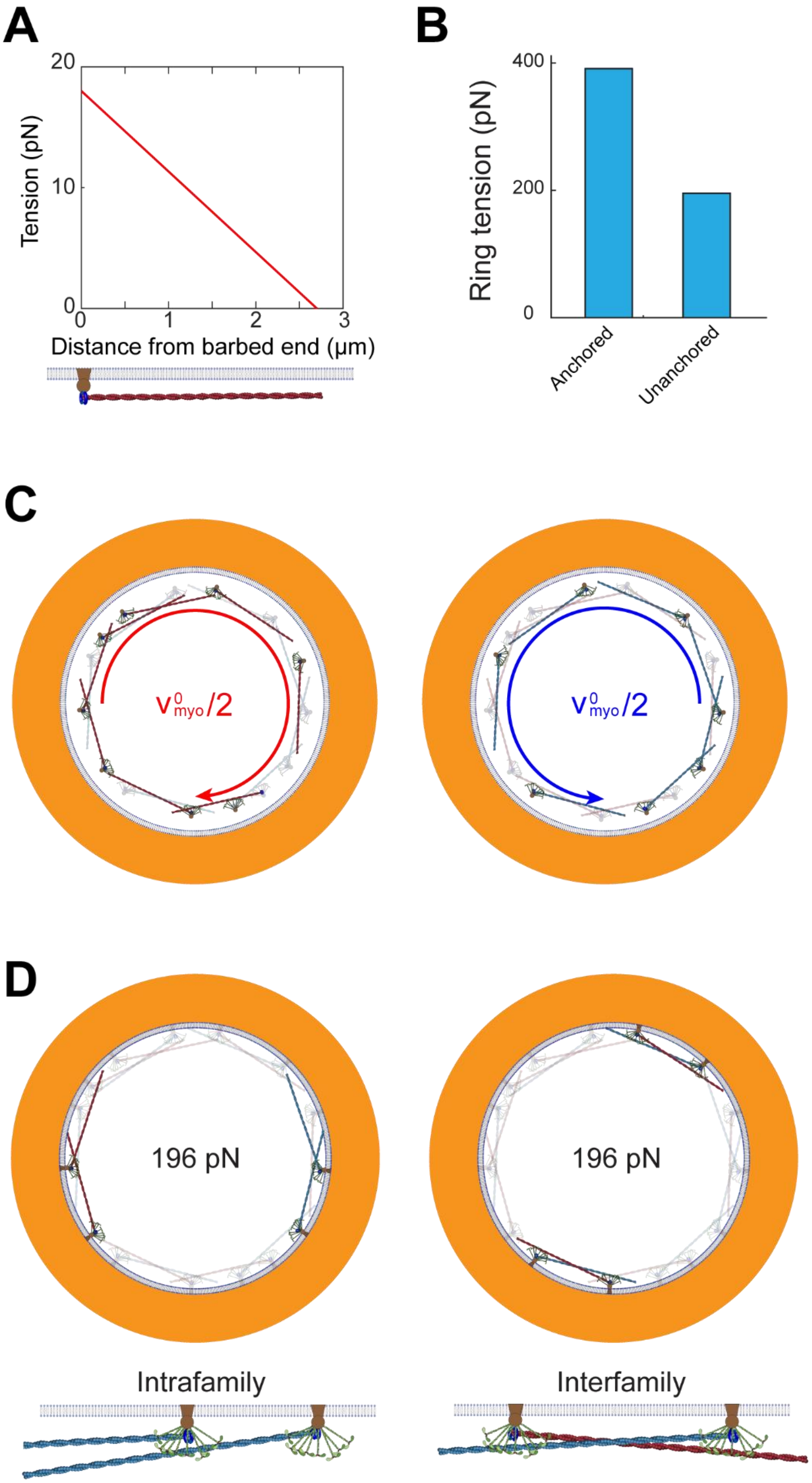
A
Tension (pN)
20
10
0
0
1
2
3
Distance from barbed end (μm)
B
Ring tension (pN)
400
200
0
Anchored
Unanchored
C
$v^0_{myo}/2$
$v^0_{myo}/2$
D
196 pN
196 pN
Intrafamily
Interfamily

Figure 3.3. The fission yeast ring generates tension by myosin pulling on barbed-end anchored actin filaments.
Model parameters as in Table 3.1 unless otherwise specified. (A) Tension versus distance from the barbed end along a filament. Tension is highest at the barbed end, and decreases linearly to zero at the pointed end. (B) Tension of rings with and without membrane anchoring. (C) Schematic of node motions in an unanchored ring, where the anchor drag coefficient γ_{anc} is zero. The motions of the clockwise (red filament) and counterclockwise (blue filament) nodes are indicated by curved arrows of respective colors. Nodes contra-rotate at the Myo2 load-free velocity v_{myo}^{0} relative to each other. (D) Schematic of two types of node-node interactions in the ring, intrafamily (left) and interfamily (right). Each type of interaction contributes half of ring tension.

The mechanism of tension generation is that myosin-II molecules bind and pull barbed-end anchored actin filaments in nodes. The filament tension is highest at the barbed end and decreases linearly to zero at the pointed end, and is balanced by the membrane drag of the barbed-end node anchor; this lateral resistance from the anchor in the membrane is the essential feature that enables the filament to build up tension. This mechanism is supported by the fact that it leads to a myosin force per head that is very similar in magnitude to previously reported values.

Membrane anchoring of actin and myosin doubles ring tension

We have seen that membrane anchoring underlies the tension generation mechanism, suggesting that in the absence of anchoring tension would vanish. We show in this section that this is in fact not true, because in the nodes organization actin barbed ends and myosin-II are internally anchored even when removed from the membrane. However, we will see that the effect of unanchoring is to halve the tension.

To perform the ‘thought experiment’ of unanchoring the ring, we will set the anchor drag coefficient γ_{anc} to zero. We will see below that this will cause much faster contra-rotation of the two node families; thus we will need to incorporate a myosin force-velocity relationship into our calculations (thus far we assumed the force exerted by a Myo2 head is fixed at f_{myo} , a good approximation for the low velocities realized in the anchored ring).

To model the unanchored ring, we incorporate a linear force velocity relationship for the myosin-II Myo2 in our model, with a Myo2 load-free velocity of v_{myo}^{0}. We assume (i) the densities of clockwise and counterclockwise nodes of the unanchored ring are uniform and equal, (ii) relative contra-rotation velocity between the two node families is uniform and equal to v_{rel}, and (iii) nodes of the same family move at a uniform velocity as in the anchored ring. We will self-consistently demonstrate the validity of these assumptions. Modifying eqns. 3.2 and 3.3 to include the myosin force-velocity relationship only for the interfamily actomyosin forces leads to

$$F_{\mathrm{node}}^{\mathrm{total}} = f_{\mathrm{node}}\left(1-\frac{v_{\mathrm{rel}}}{v_{\mathrm{myo}}^{0}}\right)n_{-} - f_{\mathrm{node}}n_{+}, \qquad f_{\mathrm{fil},+} = f_{\mathrm{node}}\left(\rho_{+} + \left(1-\frac{v_{\mathrm{rel}}}{v_{\mathrm{myo}}^{0}}\right)\rho_{-}\right). \qquad (3.13)$$

Using the homogeneous densities and number of filaments in the cross-section from eqns. 3.7, 3.8 into eq. 3.13, we have

$$F_{\mathrm{node}}^{\mathrm{total}} = f_{\mathrm{node}}\rho_{0}l\left(-\frac{v_{\mathrm{rel}}}{2v_{\mathrm{myo}}^{0}}\right), \qquad f_{\mathrm{fil},+} = f_{\mathrm{node}}\rho_{0}l\left(1-\frac{v_{\mathrm{rel}}}{2v_{\mathrm{myo}}^{0}}\right). \qquad (3.14)$$

Using these force expressions in the force balance eq. 3.1 with the membrane node anchor drag γ_{anc} set to zero, we have

$$f_{\mathrm{node}}\rho_{0}l\left(1-\frac{v_{\mathrm{rel}}}{v_{\mathrm{myo}}^{0}}\right) = 0. \qquad (3.15)$$

Thus, in the unanchored ring contra-rotating nodes exert zero force on one another, and move relative to one another with the load-free velocity of myosin Myo2, $v_{\mathrm{rel}} = v_{\mathrm{myo}}^{0} =$

240 nm s^{-1}(Stark *et al.*, 2010 & Appendix). (We note also that if formin-mediated polymerization of actin filaments is accounted for, at growth rate v_{pol}, the relative velocity becomes $v_{\text{myo}}^0 - v_{\text{pol}}$ such that the relative actin-myosin sliding velocity is maintained at v_{myo}^0 and the force is still zero.) Using eq. 3.7 and a uniform node velocity in eq. 3.4, we see that a homogeneous ring with uniform node velocities and a relative contra-rotation velocity of v_{myo}^0 satisfies all the equations (Fig. 3.3C). Similar equations can be written for the counterclockwise nodes (Materials and Methods, eqns. 3.22 and 3.23). We now calculate the force per unit length along a filament in an unanchored ring from eq. 3.13

$$f_{\text{fil},+} = f_{\text{node}}\rho_+ = \frac{f_{\text{node}}\rho_0}{2}. \tag{3.16}$$

This force per unit length is half that which a filament feels in an anchored ring (eq. 3.11). In the unanchored ring, a given actin filament experiences force only from myosin from nodes whose actin filaments have the same polarity as the given filament (eq. 3.15), in contrast to the anchored ring where Myo2 in nodes of both polarities exert force on a given filament (eq. 3.11). Thus, the actin of one node family does not feel forces from the myosins of the other node family. Using a tension calculation procedure similar to that illustrated by eqns. 3.11, 3.12, we obtain $\bar{T}_{\text{fil},+} = f_{\text{node}}\rho_0 l/4$. Thus the tension in the ring, equal to $T_{\text{ring}} = (\overline{n_+} + \overline{n_-})\bar{T}_{\text{fil},+}$, is given by

$$T_{\text{ring}} = \frac{1}{4} f_{\text{node}}\rho_0^2 l^2. \tag{3.17}$$

This is our final result for the unanchored ring. We see that an unanchored ring exerts only half the tension of the anchored ring (eqns. 3.12, 3.17, Fig. 3.3, B and D). Put differently, by anchoring components to the membrane the tension is doubled, because additional tension can then be generated by inter-node family myosin forces.

Turnover prevents myosin aggregation that would lead to loss of tension and ring fracture

Confocal micrographs show that the density of myosin-II and other components in the ring exhibit continuous intrinsic fluctuations. In this section we will use our model to show that such fluctuations are a constant threat to the tension and structural integrity of the ring, due to the intrinsic instability of contractile actomyosin structures. The instability arises because a fluctuation that increases density locally will tend to amplify the contractility at that location, further increasing the density and leading to a runaway instability. We will show that turnover plays a vital role in preventing this catastrophic sequence of events.

Let us use our model without turnover (turnover terms deleted from eqns. 3.4 and 3.21) to compute the fate, without turnover protection, of an initial 5% localized density fluctuation with full width at half maximum of 500 nm (Fig. 3.4A). We numerically solved eqns. 3.1-3.4, 3.18-3.21 and obtained the time course of node density profiles (Materials and Methods). For these calculations we added to our model a small scale short-ranged node-node repulsion of magnitude $f_{\rm rep} = 0.1$ pN and range $b_{\rm rep} = 0.1$ μm (Materials and Methods). This measure was in order to prevent a blow up of densities to infinity as aggregation progressed.

We found that the initial local density perturbation precipitated a disastrous aggregation of myosin and actin into clusters with widths much smaller than the mean actin filament length $l =$ 2.7 μm. The detailed sequence of events is shown in Fig. 3.4A. For smaller times, $t \leq 10$ s, the perturbations grow in amplitude. Valleys appeared to the left and right of the peak, separated from the peak center by $\sim l = 2.7$ µm, the mean actin filament length (Fig. 3.4A). During the next ~ 200 s, the perturbation split into two distinct peaks, each associated with one node family, and several smaller peaks and valleys appeared (Fig. 3.4A). From 200 – 600 s, peaks and valleys grew in amplitude rapidly and merged, terminating in six clusters with a mean width of ~150 nm. This final width is set by the short-ranged node repulsion force (Table 3.1).

The time for aggregation during the above process was $\tau_{\text{agg}} = 110$ s, defined as the time when the maximum density of nodes of one type increased to a value a factor e times the initial value (Fig. 3.4B).

We also tracked the mean tension of the ring during this aggregation process (Materials and Methods), and the number of actin filaments in the cross-section from eq. 3.2 (Fig. 3.4, C and D). The mean tension dropped from 382 pN to only 6 pN after 600 s, with most of the decrease from 200 s – 400 s as peaks and valleys in density became more and more pronounced (Figs. 3.4, A and C). The number of actin filaments in the cross-section remained approximately uniform up to ~250 s, after which filaments rapidly aggregated. This led to ring fracture after 540 s, defined as the time when at least one location along the ring had < 1 filament (Figs. 3.4, A and D).

We then repeated this numerical calculation with the same initial localized density perturbation, but with turnover restored. The perturbation was completely smoothed within 70 s (Fig. 3.4E). Thus, turnover prevented the aggregation and ring fracture that would have occurred after $\tau_{\text{agg}} = 110$ s. It was essential that the turnover time $\tau_{\text{turn}} = 18.6$ s was significantly smaller than the aggregation time for this intervention to be successful. These results show that in the absence of turnover the ring is inherently unstable to fluctuations in myosin density, which cause myosins to aggregate. Turnover intervenes and prevents such fluctuations from running their natural course, as it tends to restore the homogeneous state of the ring.

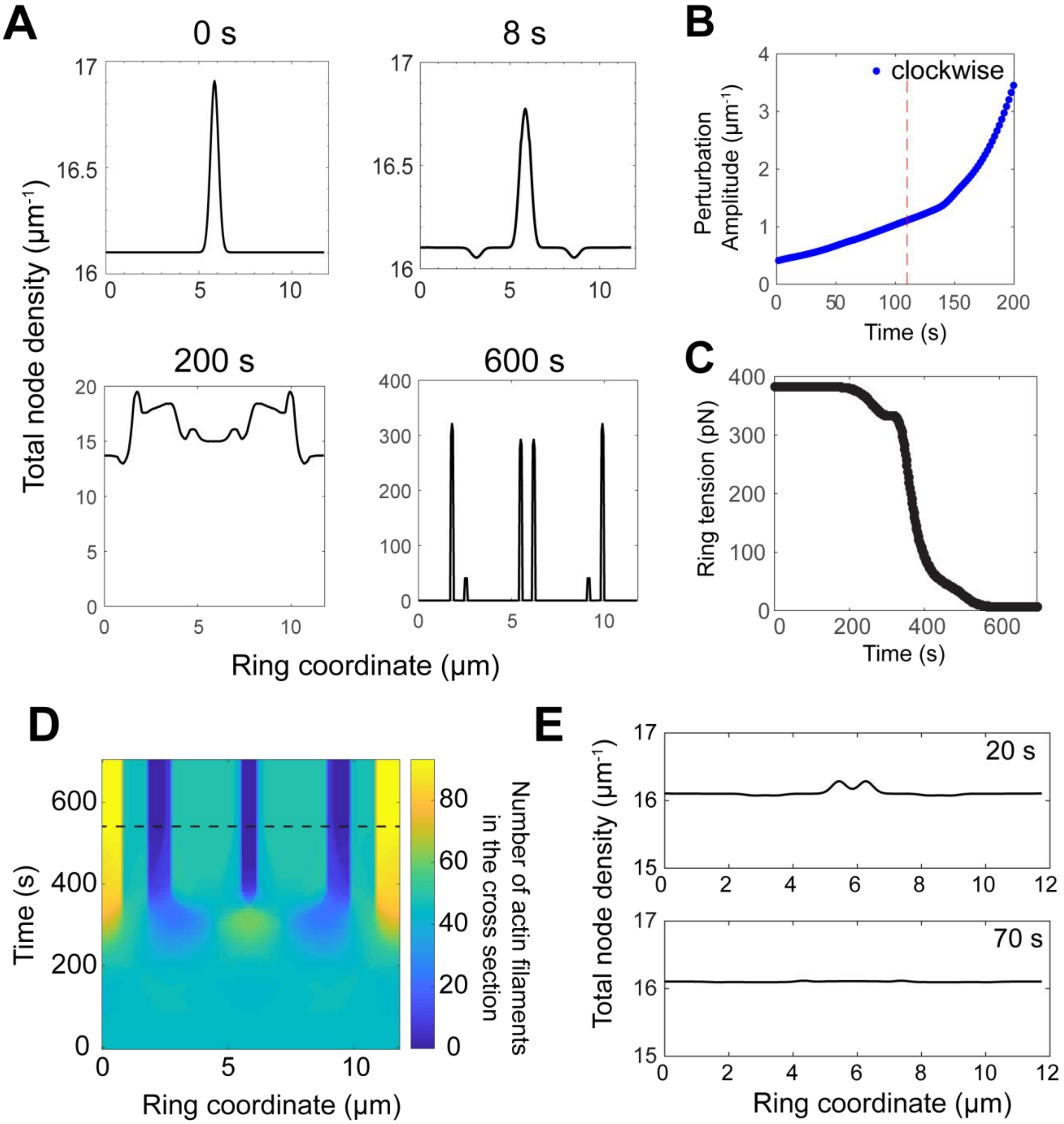

Figure 3.4 Turnover of actin and myosin in nodes prevents aggregation of nodes, loss of tension and ring fracture.

Model parameters as in Table 3.1, except that node turnover is switched off, unless otherwise stated. (A) Total node density versus ring coordinate at the indicated times. In the initial condition, a gaussian of full width at half maximum 500 nm and amplitude 5% of the mean node density ρ_0 is superimposed on a homogeneous ring of node density $\rho_0/2$ for both families. (B) Time evolution of the amplitude of the highest peak of clockwise node density profile, in the ring of (A). Vertical dashed line: Aggregation time scale τ_{agg} defined as the time at which the amplitude of the central clockwise peak increases to a value a factor e times its initial value. (C) Mean tension of the ring in (A) versus time. The ring loses 90% of its initial tension over ~500 s. (D) Total actin filaments in the ring cross-section versus ring coordinate and time of the ring in (A). Horizontal dashed line: time of ring fracture, defined as the instant where there is <1 filament at one location in the ring. (E) Total node density versus ring coordinate of a ring with turnover, at 20 s and 70 s. Turnover prevents the aggregation of nodes in the initial condition, and the initial perturbation visibly disappears by 70 s. Initial condition as in (A).

Membrane anchoring of actin and myosin stabilizes the ring

We uncovered the role of turnover in removing clumps of actin and myosin in the ring that occur due to an intrinsic aggregation instability in the ring. Presumably, the compliance of the node anchors also plays a role in such an aggregation as nodes that experience a very large drag would be reluctant to aggregate. Here, we investigated how the aggregation time varies with the membrane anchor drag coefficient.

In an earlier section we showed that anchoring of actin and myosin to the membrane double ring tension. In this section we show that anchoring serves another function, to greatly enhance stability. We will see that, were the components more weakly anchored, the intrinsic contract instabilities described above would onset more rapidly.

To demonstrate this we varied the anchor drag coefficient to be greater or smaller than the value γ_{anc}=810 pN s μm^{-1} that we had previously obtained by comparison of predicted and experimentally measured node velocities (Table 3.1). We used the same initial density fluctuation as in the previous subsection and we numerically solved eqns. 3.1-3.4, 3.18-3.21 with no turnover, using anchor drags of $\gamma_{\text{anc}} = 400 \text{ and } 1200 \text{ pN s } \mu\text{m}^{-1}$. We computed the mean ring tension (Materials and Methods) and the profile of actin filaments in the cross-section from eq. 3.2 (Fig. 3.5, A-C). For both values of the drag, the mean tension decreased from 382 pN to 6 pN, the filaments aggregated and the ring fractured (Figs. 3.5, A-C). However, for lower anchor drag these events onset sooner; for example, ring fracture occurred after 230 s (680 s) for an anchor drag of 400 (1200) pN s μm^{-1} (Fig. 3.5, A and B).

We measured the aggregation time τ_{agg} for different anchor drag values in the range $400 \leq \gamma_{\mathrm{anc}} \leq 1200$ pN s μm^{-1}. The aggregation time increased linearly with membrane drag (Fig. 3.5D).

These results show that weakening of the lateral anchoring of the nodes makes the ring more unstable and prone to aggregation, suggesting that lateral membrane anchoring is essential to stabilize the ring.

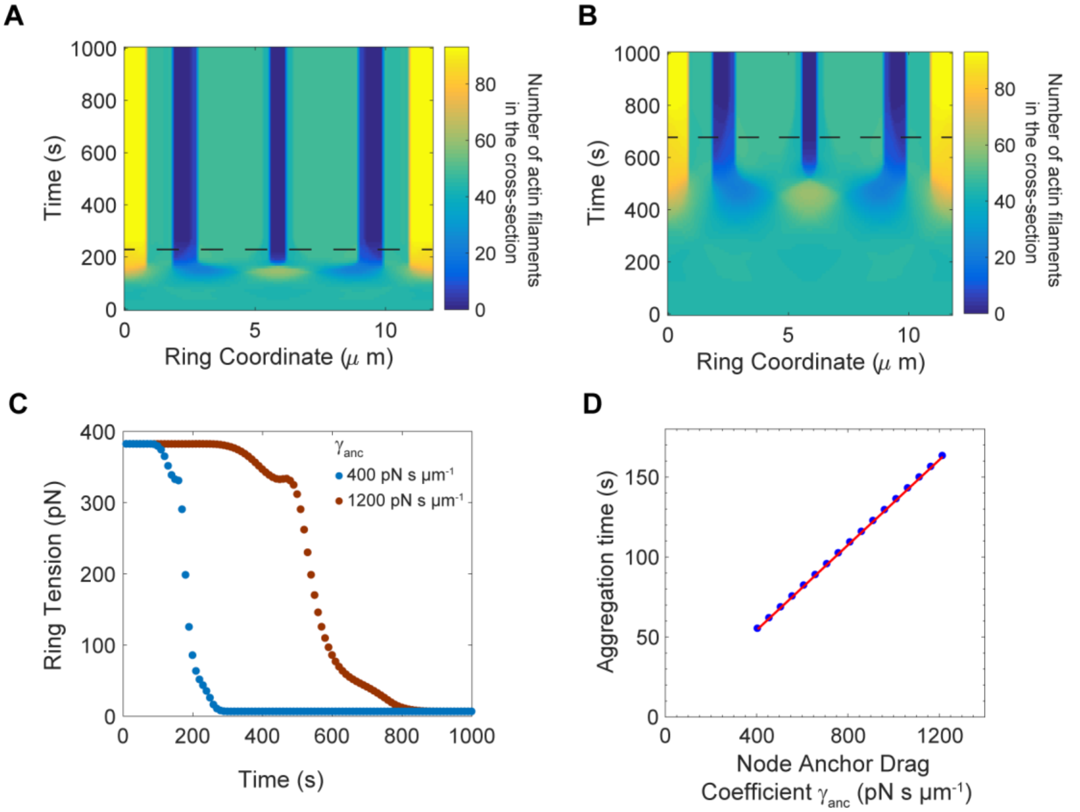

Figure 3.5. Weakening the lateral anchor drag leads to faster node aggregation and ring fracture in the absence of turnover.
Simulation parameters as in Table 3.1, except node turnover is switched off by deleting turnover terms in eqns. 3.4, 3.21, and the anchor drag coefficient γ_{anc} is varied as specified. (A, B) Profiles of actin filaments in the cross-section versus time, in rings with anchor drag coefficient γ_{anc} = 400 pN s μm^{-1} (A) and 1200 pN s μm^{-1} (B). Horizontal dashed lines indicate time to ring fracture, defined as in Figure 3.4D. (C) Time-

evolution of tension in rings of (A) (blue) and (B) (red). (D) Aggregation time versus node anchor drag coefficient γ_{anc}. Red: least-squares best-fit straight line.

Discussion

Fission yeast is a model organism for realistic mathematical models of the cytokinetic ring

In fission yeast many contractile ring proteins have been identified and their amounts measured throughout cytokinesis (Wu and Pollard, 2005; Courtemanche *et al.*, 2016). In addition, two recent developments have provided vital new information about the fission yeast cytokinetic ring which opens the door to more realistic mathematical modeling. First, perhaps the most basic property of the ring, its tension, was measured in *S. pombe* for the first time (Stachowiak *et al.*, 2014). The ring tension is the primary quantity for a mathematical model to generate and compare with experiment, and the absence of ring tension measurements has been a serious obstacle to modeling. Second, super-resolution FPALM revealed organizational features of the ring not previously available from conventional microscopy, showing that in the constricting ring myosin and formin are organized in node-like structures anchored to the plasma membrane (Laplante *et al.*, 2016).

Here we aimed to take advantage of this newly available information by building a realistic, coarse-grained, minimal model of the fission yeast ring whose assumptions are consistent with experimental measurements of actomyosin organization, membrane anchoring of ring components, and the amounts of key components (Wu and Pollard, 2005; Vavylonis *et al.*, 2008; Courtemanche *et al.*, 2016; Laplante *et al.*, 2016). Our aim was to reveal the basic principles of tension generation and stability. Our coarse-grained approach, representing components by continuous density fields, has the advantage that it can illuminate basic mechanisms at play within the complex ring organization, which might be difficult to perceive in the context of a highly detailed molecular simulation.

Node-like organization marshals actomyosin forces to generate ring tension

Cytokinetic ring tension is thought to result from non-muscle myosin-II binding to and exerting force on actin filaments. A difficulty is that the ring has considerable disorder, but a random actomyosin bundle exerts no tension, even when crosslinkers are present, because as much compression as tension is produced in filaments. Our model shows that ring tension is generated by myosin pulling on barbed-end anchored actin filaments. Anchoring barbed ends to the plasma membrane is important because it limits motion both in the radial direction and in the lateral direction. Thus, barbed-end anchoring both attaches the ring to the plasma membrane, and also provides lateral resistance to myosin pulling so that filament tension can accumulate. Barbed end anchoring is the most efficient for tension generation, as all myosins pulling a filament produce tension.

We showed that this tension production mechanism is efficient enough to generate values of tension consistent with the experimentally reported value of ~ 400 pN (Stachowiak *et al.*, 2014), (Fig. 3.3B), given the total amount of actin and myosin in the ring (Wu and Pollard, 2005; Courtemanche *et al.*, 2016). By fitting the predicted tension to experiment, we obtained a myosin force per head for fission yeast Myo2, $f_{\mathrm{myo}} \sim 1.1$ pN. The force per head is actually somewhat less than the stall force f_{stall}, due to relative motions of the nodes and due to formin-mediated growth of the actin filaments. Assuming a linear force-velocity relation for Myo2, we estimate $f_{\mathrm{myo}} \sim 0.45 f_{\mathrm{stall}}$ (see Appendix). Thus, $f_{\mathrm{stall}} \sim 2.5$ pN, close to previously reported stall force values for myosin-II in different organisms, 0.6 – 2.3 pN (Kishino and Yanagida, 1988; Molloy *et al.*, 1995; Ishijima *et al.*, 1996; Tyska *et al.*, 1999).

Our model neglected crosslinkers in the ring. How much do they contribute to tension? The best characterized actin filament crosslinkers in the fission yeast cytokinetic ring are α-actinin dimers which are very dilute in the ring: given ~250 α-actinin dimers and ~190 nodes each with a mean of about one filament at onset of constriction (Wu and Pollard, 2005; Courtemanche *et al.*, 2016; Li *et al.*, 2016), there are $n_\alpha \sim 1-2$ crosslinking connections per actin filament. Each of these has a relatively small turnover time τ_α ~ 0.3 s, according to the *in vitro* experiments of Li et al., 2016. Using the measured α-actinin force constant k_α = 0.025 pN nm^{-1} (Claessens *et al.*, 2006), and taking the relative velocity of actin filaments to be twice the node velocity $2v_0$ ~ 44 nm s^{-1}, we estimate a typical force per actin filament $\sim 2k_\alpha v_0 \tau_\alpha n_\alpha$ ~0.6 pN, much smaller than the ~ 20 pN force that Myo2 exerts on a filament. Thus, α-actinin is likely unimportant to internal ring forces and dynamics in the constricting ring. Furthermore, given the relatively small amount of α-actinin, we suggest that myosin-II probably serves as the main crosslinker for bundling the ring.

Bidirectional motions reflect two classes of nodes in the constricting ring

From FPALM, an interesting observation about the constricting fission yeast ring is that myosin and formin move bidirectionally, with similar velocity distributions (Laplante *et al.*, 2016). This supports the nodes hypothesis, and also indicates that few nodes remain stationary and suggests that there are two families of nodes with opposite directionality.

What defines this directionality? We used our model to show that actin filaments are responsible. A typical node, having on average one actin filament emanating from it, moves in the direction defined by the polarity of this actin filament. The actin filament produces a bias in the node motion because it points in a particular direction and is grabbed by myosin-II molecules, all pulling the filament in that same direction. By contrast the myosin belonging to that node produces no bias in motion, because it grabs filaments in the unbiased bundle with balanced polarity. Overall, our model reproduces the phenomenon that nodes move bidirectionally in the constricting ring (Fig. 3.2).

A previous model considered a similar but different ring organization, in which formin and myosin were assumed independently anchored rather than co-anchored in nodes. The model produced a stable ring that generates tension similar to experimental values (Stachowiak *et al.*, 2014). If we were to consider such an arrangement in the framework of the present model, the mean tension per filament, and hence the ring tension, would be unchanged, as every actin filament would interact with the same number of myosin-II heads as in the nodes organization. The formins would be predicted to execute bi-directional motion, but the anchored myosins would not move other than small fluctuations since their velocity is proportional to the local net actin polarity, which vanishes for a homogeneous ring. This latter feature is inconsistent with FPALM measurements that report bidirectional motions of both formin and myosin with similar speeds (Laplante *et al.*, 2016).

A stochastic sliding filament mechanism operates in the fission yeast cytokinetic ring

Long ago a sliding filament mechanism was proposed for tension production by cytokinetic rings (Schroeder, 1975; Maupin and Pollard, 1986). How this might actually work is not obvious, however, since in muscle the mechanism is based on the sarcomere repeat unit and contraction of the unit produces thickening. In the fission yeast contractile ring neither sarcomeres nor thickening are apparent (Kanbe *et al.*, 1989a; Bezanilla and Pollard, 2000; Wu and Pollard, 2005; Kamasaki *et al.*, 2007).

Our model shows that the mechanism at work is related to the sliding filament system used in muscle, but is a subtly stochastic and transient version of this model in such a way as to maintain translational invariance along the ring. We find that filaments slide in opposition to one another, but do so continuously and everywhere around the ring, without being confined to fixed sarcomere-like structures. Moreover, the sliding processes are transient.

More specifically, we found that even though nodes are positioned around the ring without periodicity, pairwise interactions between nodes have characteristics of the sliding filament mechanism. However, the interactions are transient and stochastic. A pair of nodes with opposite polarity interact like a sarcomere or contractile unit (Fig. 3.3D, “inter-family”). As the two families of nodes contra-rotate, pairs of nodes with opposite polarity disappear as they meet and move past one other, while new pairs constantly appear as nodes first arrive within reach of one another. Turnover of nodes also contributes to the transient nature of the sliding filament interaction.

We find, however, that the sliding filament mechanism is not the whole story. A pair of nodes with the same polarity interacts like one half of a sarcomere, with myosins pulling on barbed-end anchored actin filaments (Fig. 3.3D, “intra-family’). Unlike the transient appearing and disappearing of inter-family interacting pairs, pairs of nodes with the same polarity do not move relative to each other and maintain their relation until they leave the ring. Without sliding relative to one another, they generate tension, because a large number of such nodes are connected in a single family ring. Our model shows that each of these two sub-organizations contributes to half of the ring tension.

Anchoring of components to the membrane and component turnover protect the ring from intrinsic instabilities

We found that the cytokinetic ring suffers from an instability characteristic of actively contractile organizations. A fluctuation that increases the local actin and myosin density produces higher contractile forces that draw in further actin and myosin, increasing the local contractility further and leading to run-away aggregation (Figs. 3.4 and 3.5). In the absence of turnover, this instability led to loss of tension and ring fracture after a certain aggregation timescale (Fig. 3.4). Restoring turnover, this disastrous outcome was averted provided the turnover time is less than the aggregation time. In normal cells this is indeed the case. We conclude that turnover functions to preserve organizational homeostasis and tension in the ring.

In addition, we found that node anchor drag in the membrane protects the ring from this contractile instability, because the bigger the drag the longer the aggregation and ring fracture time (Fig. 3.5). Thus, anchoring of components in the plasma membrane and turnover work together to stabilize the ring.

Cytokinetic rings in other organisms

What can the results of the present study tell us about cytokinetic rings in organisms other than fission yeast? While animal cells have much longer and wider contractile rings, their thicknesses are very similar to that of the fission yeast ring, ~ 0.1-0.4 μm (Schroeder, 1972; Mabuchi, 1986), suggesting that anchoring of components to the plasma membrane may play a similar role in the tension mechanism as in fission yeast. Furthermore, in sea urchin embryos, contractile rings appear to assemble from clusters of myosin-II (Henson *et al.*, 2017), reminiscent of the nodes from which the fission yeast ring is assembled (Vavylonis *et al.*, 2008). However, light and dark bands were seen in electron microscopy images of the cleavage furrow in rat kangaroo cells (Sanger and Sanger, 1980). Fluorescence micrographs show bipolar myosin-II filaments in the contractile ring in sea urchin embryos and LLC-Pk1 cells (Beach *et al.*, 2014; Henson *et al.*, 2017) and lateral stacking of myosin bipolar filaments in striated patterns reminiscent of sarcomeric organization in HeLa cells (Fenix *et al.*, 2016). Thus, cytokinetic rings in other organisms may exhibit both similarities and significant differences in organization, and a major scientific challenge will be to establish if basic mechanisms emerging in fission yeast carry over to these organisms.

Materials and Methods

Model equations for the time evolution of counterclockwise nodes

The equations for evolution of the density and velocity of the clockwise nodes are eqns. 3.1-3.4. Similar equations can be written for the counterclockwise '-' nodes, using the following replacements in these equations: density $\rho_+(x,t) \to \rho_-(x,t)$ in eq. 3.4, velocity $v_+(x,t) \to v_-(x,t)$ in eqns. 3.1, 3.4, and the filament length $l \to -l$ in eq. 3.3 as the filaments of these nodes are pointing in the opposite direction.

$$\gamma_{\text{anc}} v_- = F_{\text{node}}^{\text{total}} + F_{\text{fil},-}^{\text{total}} \tag{3.18}$$

$$F_{\text{node}}^{\text{total}} = f_{\text{node}}(n_- - n_+),\ n_+ = \int_{x-l}^{x} \rho_+ dy\,,\ n_- = \int_{x}^{x+l} \rho_- dy \tag{3.19}$$

$$F_{\text{fil},-}^{\text{total}} = -f_{\text{node}} \int_{x-l}^{x} (\rho_+(y,t) + \rho_-(y,t))\, dy \tag{3.20}$$

$$\frac{\partial \rho_-}{\partial t} + \frac{\partial}{\partial x}(\rho_- v_-) = \frac{\rho_0/2 - \rho_-}{\tau_{\text{turn}}} \tag{3.21}$$

In the presence of a force-velocity relationship for the myosin Myo2, eqns. 3.19 and 3.20 get modified as

$$F_{\mathrm{node}}^{\mathrm{total}} = f_{\mathrm{node}} n_- - f_{\mathrm{node}} \left(1 - \frac{v_{\mathrm{rel}}}{v_{\mathrm{myo}}^0}\right) n_+ \tag{3.22}$$

$$F_{\mathrm{fil},-}^{\mathrm{total}} = -f_{\mathrm{node}} \int_{x-l}^{x} \left(\left(1 - \frac{v_{\mathrm{rel}}}{v_{\mathrm{myo}}^0}\right) \rho_+(y,t) + \rho_-(y,t) \right) dy \tag{3.23}$$

Numerical solution of the model

We solved eqns. 3.1-3.4, 3.18-3.21 numerically using Runge-Kutta 4 with a spatial grid size of 50 nm and a time step of 0.2 s, except for the velocity results for Fig. 3.2 where a finer grid of size 10 nm was used to achieve more accurate velocities. The mean velocity of the peak and the valley of Fig. 3.2B was measured as the slope of the best-fit straight-line to the peak or valley position versus time.

As the model exhibits presumably unbounded node density growth in the absence of turnover, we used a non-linear filter to remove numerical instabilities (Engquist *et al.*, 1989). In the absence of turnover, a node-node repulsive force was used to prevent unbounded growth. In this case, eqns. 3.1 and 3.18 gets modified as

$$\gamma_{\mathrm{anc}} v_+ = F_{\mathrm{node}}^{\mathrm{total}} + F_{\mathrm{fil},+}^{\mathrm{total}} + F_{\mathrm{rep}}^{\mathrm{total}}, \ \gamma_{\mathrm{anc}} v_- = F_{\mathrm{node}}^{\mathrm{total}} + F_{\mathrm{fil},-}^{\mathrm{total}} + F_{\mathrm{rep}}^{\mathrm{total}}. \tag{3.24}$$

Here $F_{\mathrm{rep}}^{\mathrm{total}}$ is a short-ranged repulsive force between nodes of magnitude f_{rep} and length scale b_{rep} given by

$$F_{\mathrm{rep}}^{\mathrm{total}} = f_{\mathrm{rep}} \left(\int_{x-b_{\mathrm{rep}}}^{x} (\rho_+ + \rho_-) dy - \int_{x}^{x+b_{\mathrm{rep}}} (\rho_+ + \rho_-) dy \right). \tag{3.25}$$

f_{rep} and b_{rep} were chosen such that the final mean cluster width after aggregation was ~150 nm. All numerical calculations were done in MATLAB.

Tension formula for the numerical calculations of the model

Every arrangement of nodes in the ring corresponds to a ring tension, which we calculate as follows. A clockwise filament from a + node at the point *s* crossing the point of interest *x* feels a pulling force f_{node} from the myosins of all the nodes lying along its length from *x* till its pointed end at $s + l$. A similar pulling force is felt by counter-clockwise filaments from the nodes at *x* till their pointed end at $s - l$. The net tension is obtained by summing these contributions over all the filaments at the point *x*

$$T(x) = f_{\mathrm{node}} (\int_{x-l}^{x} \rho_+(s) \int_{x}^{s+l} \rho_{\mathrm{tot}}(y) dy\, ds + \int_{x}^{x+l} \rho_-(s) \int_{s-l}^{x} \rho_{\mathrm{tot}}(y) dy\, ds). \tag{3.26}$$

The mean tension is then obtained by averaging T over the ring length.

Initial conditions

For the velocity measurements in Figs. 3.2B and 3.2C, the following initial condition was used

$$\rho_{\pm}(x,t) = \frac{\rho_0}{2} \left(1 \pm 0.05 \exp \left(-\frac{(x - L_0/2)^2}{2\sigma^2} \right) \right) \tag{3.27}$$

where $\rho_0 = 16.1\ \mu\mathrm{m}^{-1}$ is the mean total density of nodes, x is the coordinate along the ring i.e. $0 \le x \le L_0$ where $L_0 = 11.8\ \mu\mathrm{m}$ is the initial length of the ring. σ is the standard deviation of the Gaussian function and is related to the full width at half maximum w as $w = 2\sqrt{2\ln 2}\,\sigma \approx 2.355\,\sigma$.

For the results of Figs. 3.4 and 3.5, a similar initial condition was used

$$\rho_{\pm}(x,t) = \frac{\rho_0}{2}\left(1 + 0.05\exp\left(-\frac{(x-L_0/2)^2}{2\sigma^2}\right)\right). \tag{3.28}$$

The full width at half maximum here is $w = 500$ nm, which gives $\sigma = 212$ nm.

Appendix

Determination of myosin-II load-free velocity $\boldsymbol{v_{\mathrm{myo}}^{0}}$ from the gliding filament assay of (Stark *et al.*, 2010)

A previous experiment measured the velocity of actin filaments gliding on fission yeast myosin-II Myo2 that was adhered onto a coverslip (Stark *et al.*, 2010). The authors measured the increase of the gliding velocity of the filaments with the number of Myo2 heads interacting with the actin filament. The velocity saturated at ~50 heads.

Using the measurement of a mean of 1500 and 180 dimers of myosin Myo2 and formin Cdc12 respectively using quantitative fluorescence microscopy (Wu and Pollard, 2005; Courtemanche *et al.*, 2016), and the proposal of a mean of 8 myosin Myo2 dimers per node using FPALM (Laplante *et al.*, 2016), we calculated the total mean number of nodes as 190, and a mean of 0.95 formin dimers per node. Thus, our model has 190 nodes with one actin filament, one formin dimer, and 8 myosin dimers each. Thus, the ratio of Myo2 molecule number to actin filament number is 16. At this ratio, the gliding filament assay measurements report an actin filament gliding velocity of 240 nm s^{-1}, which is the myosin-II load-free velocity v_{myo}^{0} as the myosins experience little load in these experiments (Stark *et al.*, 2010).

Linear stability analysis of the model-predicted homogeneous ring in the presence of turnover

One steady state solution to eqns. 3.1-3.4, 3.18-3.21 is $\rho_{\pm}(x,t) = \rho_0/2$ and $v_{\pm}(x,t) = \pm v_0$ where $v_0 = \rho_0 f_{\mathrm{node}} l/\gamma_{\mathrm{anc}}$. Now, let us consider a small perturbation to the steady state of wavenumber k or equivalently a wavelength $2\pi/k$. The node density is $\rho_{\pm}(x,t) = \rho_0/2 + \varepsilon_{\pm}(t)\exp(ikx)$ where $\varepsilon_{\pm}(0) \ll \rho_0$ and we calculate the time evolution of $\varepsilon_{\pm}(t)$. Plugging this into eqns. 3.1-3.4, 3.18-3.21 and linearizing about the steady state $\rho_{\pm}(x,t) = \rho_0/2$, we get

$$\frac{\partial \varepsilon_+}{\partial t} = -a_1\varepsilon_+ - a_2\varepsilon_- \tag{3.29}$$

$$\frac{\partial \varepsilon_-}{\partial t} = -a_2^{\star}\varepsilon_+ - a_1^{\star}\varepsilon_- \tag{3.30}$$

where $a_1 = ikv_0 - (1-\cos kl)/2\tau_{\mathrm{a}} + 1/\tau_{\mathrm{t}}$, $a_2 = (\exp ikl - 1)/2\tau_{\mathrm{a}}$, and $\tau_{\mathrm{a}} = l/2v_0$ is a characteristic timescale whose meaning will be explained later in the section. Eliminating ε_- between these two equations, we get

$$\frac{\partial^2 \varepsilon_+}{\partial t^2} + (a_1 + a_1^{\star})\frac{\partial \varepsilon_+}{\partial t} + (|a_1|^2 - |a_2|^2)\varepsilon_+ = 0 \tag{3.31}$$

The solution to this equation is of the form $\varepsilon_+(t) = c_1 \exp -t/\tau_1 + c_2 \exp -t/\tau_2$ where τ_1^{-1} and τ_2^{-1} are the solutions of the quadratic equation $x^2 + (a_1 + a_1^{\star})x + (|a_1|^2 - |a_2|^2) = 0$ as can be verified by plugging in this solution to eq. 3.31. The constants c_1 and c_2 depend on the initial conditions $\varepsilon_{\pm}(0)$ and are not calculated here.

The timescales τ_1, τ_2 set the stability of the ring. Using the substitution $\tau_{\mathrm{a}} = l/(2v_0)$ and the expressions for $a_1,\ a_2$, the solutions to the quadratic equation are

$$\frac{1}{\tau_1} = \frac{1}{\tau_{\mathrm{t}}} - \frac{1-\cos kl}{2\tau_{\mathrm{a}}} + ikf(k) \tag{3.32}$$

$$\frac{1}{\tau_2} = \frac{1}{\tau_{\mathrm{t}}} - \frac{1-\cos kl}{2\tau_{\mathrm{a}}} - ikf(k) \tag{3.33}$$

where $f(k) = v_0((k^2l^2/2 - 1 + \cos kl)/(k^2l^2/2))^{1/2}$. Thus, the fluctuations could decay or grow exponentially with time depending on whether the real part of the timescales $\mathrm{Re}(\tau_1), \mathrm{Re}(\tau_2)$ is positive or negative respectively. From eqns. 3.32 and 3.33, we can see that if $\tau_{\mathrm{t}} < \tau_{\mathrm{a}}$, the real part is positive for all wavenumbers and the model-predicted homogeneous ring is stable in the face of small fluctuations. As the experimentally measured turnover time $\tau_{\mathrm{t}} = 18.6$ s is smaller than the model-predicted aggregation time $l/2v_0 = 61.4$ s, this condition is satisfied. In addition, as the turnover time is only about a third of the aggregation time i.e. $\tau_{\mathrm{t}} \ll \tau_{\mathrm{a}}$, fluctuations of all wavelengths decay with roughly the same time scale i.e. $\mathrm{Re}(\tau_1) \approx \mathrm{Re}(\tau_2) \approx \tau_{\mathrm{t}}$.

In the absence of turnover, the real parts of these time scales are negative and the fluctuations grow with time. The shortest time scale of growth is for a fluctuation of wavelength *2l* and is τ_{a}, as can be seen by the substitution $k = 2\pi/(2l)$ in the solutions above. The fastest growing fluctuations are those of wavelengths $2l/n$ where n is an odd integer. We note here that this analysis is only valid for the initial stages of growth in fluctuation amplitude where these amplitudes are small compared with the mean node density ρ_0. In the later phase of growth, non-linear effects are important.

Effect of Myo2 force-velocity relation and actin filament growth on myosin force per head

For simplicity our model considered a fixed force per Myo2 head, f_{myo}, which was assumed to have the same order of magnitude as the stall force of Myo2, f_{stall}. However, we did not consider the myosin force-velocity relationship to estimate how much f_{myo} deviates from f_{stall}. Our model did not explicitly include formin-mediated polymerization of actin filaments, which would increase this deviation. Below, we calculate by how much f_{myo} differs from f_{stall}.

(i) Consider first interfamily interactions, i.e. between nodes whose actin filament has one polarity with nodes whose filament has the opposite polarity. In our model, the relative velocity between myosins of one node family and actin filaments belonging to nodes of the opposite polarity is $2v_0$, where v_0 is the node velocity. Actin filament growth at rate v_{pol} would increase this relative velocity to $2v_0 + v_{\mathrm{pol}}$. Assuming a simple linear force-velocity relation, the myosin force is thus lowered to $f_{\mathrm{myo}} = f_{\mathrm{stall}}\left(1 - [2v_0 + v_{\mathrm{pol}}]/v_{\mathrm{myo}}^0\right)$. (ii) Now consider intrafamily interactions, between two nodes of the same polarity. The myosin force is now lowered to $f_{\mathrm{myo}} = f_{\mathrm{stall}}\left(1 - v_{\mathrm{pol}}/v_{\mathrm{myo}}^0\right)$, as the relative velocity between myosins belonging to the same node family is zero, so the relative velocity between the myosin of one node and the actin filament of another node in the same family is v_{pol}. (iii) To obtain the overall effect on the value of f_{myo}, it is necessary to take the mean of the two contributions from interfamily and intrafamily interactions, since they contribute equally to ring tension. This gives a mean relation $f_{\mathrm{myo}} = f_{\mathrm{stall}}\left(1 - [v_0 + v_{\mathrm{pol}}]/v_{\mathrm{myo}}^0\right)$.

Now we estimate filament growth rates using previous experimental measurements of ring disassembly in the presence of the actin monomer sequestering drug Latrunculin A. Only ~10% of rings remained after 55 s of exposure (Yonetani *et al.*, 2008). This gives an actin turnover rate of ~0.042 s^{-1}, assuming the fall-off of actin subunit numbers in the ring is exponential with time. Using this turnover rate, the actin filament growth rate that would have normally occurred to synthesize a filament of mean length 2.7 μm is v_{pol} ~ 110 nm s^{-1}.

Using this value of v_{pol}, the node speed $v_0 = 22\ \mathrm{nm\ s}^{-1}$, and the Myo2 load-free velocity $v_{\mathrm{myo}}^0 = 240\ \mathrm{nm\ s}^{-1}$, we obtain $f_{\mathrm{myo}} \sim 0.45 f_{\mathrm{stall}}$. This is our main conclusion regarding how the force-velocity relation and actin polymerization reduce the myosin per force per head from the stall force value.

Now in the subsection "*Tension is generated in the cytokinetic ring by myosin pulling on barbed end anchored actin filaments*" of *Results*, we compared the model-predicted value of ring tension with the experimentally measured value, and we found $f_{\mathrm{myo}} \sim 1.1$ pN. Thus, we obtain a value of the stall force f_{stall} ~ 2.4 pN. This is close to previously reported stall force values for myosin-II in different organisms, 0.6 – 2.3 pN (Kishino and Yanagida, 1988; Molloy *et al.*, 1995; Ishijima *et al.*, 1996; Tyska *et al.*, 1999).

Chapter 4: Dilation of fusion pores by crowding of SNARE proteins

Introduction

Fusion pores are nanoscale connections between membrane-enclosed compartments that are key intermediates during membrane fusion reactions such as the exocytotic release of neurotransmitters and hormones (Lindau and de Toledo, 2003). Following nucleation by specialized proteins (Chernomordik and Kozlov, 2008), fusion pores flicker repeatedly and then dilate or reseal during release of hormones (Lindau and de Toledo, 2003) or neurotransmitters (Staal *et al.*, 2004; He and Wu, 2007; Alabi and Tsien, 2013), or during fusion mediated by viral proteins (Cohen and Melikyan, 2004). The mechanisms that govern these behaviors are poorly understood, despite the availability of sensitive electrical and electrochemical methods to detect single fusion pores during protein-free fusion (Chanturiya *et al.*, 1997; Mellander *et al.*, 2014), viral protein induced fusion (Cohen and Melikyan, 2004), and exocytosis (Lindau, 2012). Even the very nature of the fusion pore intermediate (whether lipid- or protein-lined) is debated (Bao *et al.*, 2016).

During exocytotic neurotransmitter or hormone release, a fusion pore opens as vesicle-associated *soluble N-ethylmaleimide-sensitive factor attachment protein receptors* (v-SNAREs) pair with cognate t-SNAREs on the target plasma membrane (Sudhof and Rothman, 2009). This is a tightly regulated process that requires coordinated actions of several proteins, including Munc18, Munc13, and others (Rizo and Xu, 2015). Complex formation between the v- and t-SNAREs likely starts from the membrane distal N-termini and may proceed in stages toward the membrane-proximal regions (Gao *et al.*, 2012). Assembly of the SNARE domains results in a four-helix bundle (SNAREpin) that brings bilayers into close proximity, but assembly is thought to be halted at some stage to poise vesicles for fast release. Calcium influx in response to depolarization is thought to lead to further SNARE assembly that promotes pore nucleation. This last step coupling calcium entry to fusion also requires Synaptotagmin and Complexin, which may actively contribute to pore opening. The initial fusion pore is a metastable structure that may reseal without ever dilating beyond ~1-2 nm in size. This results in transient "kiss & run" exocytosis, a well-established mode of fusion for hormone-secreting cells (Fulop *et al.*, 2005; Hanna *et al.*, 2009; Alabi and Tsien, 2013). In contrast, whether transient fusion is a relevant mode of release for synaptic vesicle fusion is debated (Pawlu *et al.*, 2004; Staal *et al.*, 2004; He and Wu, 2007; Alabi and Tsien, 2013; Chapochnikov *et al.*, 2014), mainly due to technical challenges in probing fusion pores directly during synaptic release. For both neuronal and endocrine release, little is known about the molecular mechanisms that govern pore dilation and set the balance between transient and full fusion (Alabi and Tsien, 2013), in large part due to a lack of biochemically defined assays that are sensitive to single-pores.

Here, using a recently developed nanodisc-cell fusion system (Wu *et al.*, 2016), we found that only a few SNARE complexes can nucleate a pore, but reliable pore dilation necessitates many more.

Results

Fusion between v-SNARE reconstituted nanolipoprotein particles and flipped t-SNARE cells

Here we used 21-27 nm diameter nanolipoprotein particles (NLPs) (Bello *et al.*, 2016) to determine whether SNAREs alone can catalyze pore dilation. In contrast, most previous studies employed much smaller, 6-18 nm diameter NDs (Shi *et al.*, 2012; Bao *et al.*, 2016; Wu *et al.*, 2016), whose dimensions restricted pore diameters to ≲ 4 nm (Wu *et al.*, 2016) and SNARE copy numbers to ≲ 9, precluding studies of pore dilation (Bello *et al.*, 2016). We incorporated v-SNAREs into NLPs stabilized by a recombinant apolipoprotein E variant consisting of the N-terminal 22 kDa fragment (ApoE422k), and varied the lipid-to-ApoE422 ratio to control the NLP size and the VAMP2-to-ApoE422k ratio to tune the v-SNARE copies per NLP (Bello *et al.*, 2016) (Fig. 4.1). We confirmed that vNLPs fused with liposomes reconstituted with t-SNAREs in a SNARE-dependent manner using a previously described bulk assay that monitors calcium release through pores connecting v-SNARE nanodiscs with t-SNARE liposomes (Shi *et al.*, 2012; Bello *et al.*, 2016) (Fig. 4.1—Figure supplement 1a). Although NLP pores could in principle grow to ≳ 10 nm diameter (Fig. 4.4b), much larger than the ∼4 nm allowed by the MSP ND geometry (Shi *et al.*, 2012; Wu *et al.*, 2016), bulk calcium release rates were comparable between vNLP and vMSP NDs loaded with similar v-SNARE copy numbers (Fig. 4.1—Figure supplement 1b), confirming that the bulk assay is largely insensitive to pore properties under these conditions (Bello *et al.*, 2016).

We then confirmed lipid mixing between the membranes of vNLPs and flipped t-SNARE cells (tCells) using a previously described protocol (Wu *et al.*, 2016) (Fig. 4.2). NLPs co-labeled with 1 mole % each of DiI (donor) and DiD (acceptor) were incubated with tCells for 30 min at 4°C, a temperature that allows docking, but not fusion. Cells were then rinsed to remove free NLPs and mounted onto a confocal microscope stage held at 37°C to initiate fusion and imaging of DiI and (directly excited) DiD fluorescence. At the concentrations used, when the dyes are initially in the NLP membrane, the DiI fluorescence is quenched by DiD. Upon fusion, the dyes become diluted in the plasma membrane and the DiI fluorescence increases. Directly excitated DiD fluorescence provides a measure of the amount of docked NLPs. The ratio of the DiI to DiD intensity normalizes the lipid mixing signal to the amount of docked NLPs. Normalized lipid mixing signals increased when tCells were incubated with vNLPs carrying 8 v-SNAREs total (vNLP8), but not with empty NLPs (eNLP) or NLPs loaded with 8 copies of a v-SNARE construct, VAMP2-4X, carrying mutations in the C-terminal hydrophobic layers (L70D, A74R, A81D, and L84D) (Fig. 4.2b). These mutations prevent zippering of the C-terminal half of the SNARE domains (Krishnakumar *et al.*, 2011; Krishnakumar *et al.*, 2013; Wu *et al.*, 2016), a perturbation that does not affect docking (Fig. 4.2c) but prevents fusion (Fig. 4.2b,d) (Krishnakumar *et al.*, 2013; Wu *et al.*, 2016). A variation of the assay that avoided the 4°C incubation but prevented live imaging in the presence of the labeled NLPs confirmed these results (Fig. 4.2d). We estimate that 4-5 % of the docked vNLPs undergo fusion with the flipped t-SNARE cells over the course of ~20 min (Fig. 4.2—Figure supplement 1). In comparison, fusion between v-SNARE NLPs and t-SNARE liposomes yields a similar extent of lipid mixing over the same period (Bello *et al.*, 2016).

Lipid mixing could result from the merging of only the proximal lipid bilayer leaflets of the vNLPs and the tCells. To test whether full fusion occurred, we loaded the cells with Fluo-4, a fluorescent calcium probe, and monitored calcium signals. If full fusion occurred, then calcium influx through the fusion pores connecting vNLP and tCell membranes should increase cytosolic Fluo-4 signals (Wu *et al.*, 2016). This was indeed the case for vNLP8 samples, but not for empty NLPs or NLPs loaded with VAMP2-4X (Fig. 4.3) Using this calcium influx assay, we also assessed whether pores eventually resealed by washing away the free vNLPs after 5 min of incubation. Cellular calcium levels returned to baseline within a few minutes, suggesting pores eventually resealed (Fig. 4.3—Figure supplement 1).

Dynamics of single fusion pores

Next, we probed single pores connecting vNLPs to tCell membranes (Wu *et al.*, 2016) (Fig. 4.4). We voltage-clamped in the cell-attached conFiguration a “tCell” ectopically expressing “flipped” neuronal/exocytotic t-SNAREs syntaxin1 and SNAP25 (Hu *et al.*, 2003) (Fig. 4.4). NLPs reconstituted with 8 copies of the complementary neuronal v-SNARE VAMP2/synaptobrevin (vNLDs), included in the pipette solution (100 nM vNLPs, 120 µM lipid), diffused to the pipette tip and fused with the patch. Because a NLP is not a closed structure like a vesicle, its fusion with the voltage-clamped membrane patch establishes a direct conduction pathway between the cytosol and the pipette solution, leading to direct-currents whose magnitude reflects pore geometry (Wu *et al.*, 2016).

Currents appeared in bursts with an average frequency of ~0.2 bursts per min, or ~2.5 per patch (Fig. 4.4c). The very low burst frequency, together with small unitary conductances (see below), strongly suggest that each burst represents currents passing through a single pore (Wu *et al.*, 2016). Currents fluctuated and returned to baseline multiple times, as if the fusion pore fluctuated in size and opened and closed repeatedly, i.e. flickered (Fig. 4.4d and Materials and Methods). Nucleation was blocked when the cytoplasmic domain of VAMP2 (CDV), or the tetanus neurotoxin light chain (TeNT) were included in the pipette solution, or empty NLPs (eNLPs) were used (Fig. 4.4c). CDV competes with the NLP v-SNAREs for binding to the flipped t-SNAREs on the patch surface, and TeNT cleaves VAMP2. When we used VAMP2-4X, pore nucleation rate was not significantly different than any of the other negative controls (Fig. 4.4c). Because this construct allows efficient docking (Fig. 4.2c) but is fusion incompetent (Fig. 4.2b,d) (Krishnakumar *et al.*, 2013; Wu *et al.*, 2016), this result indicates ApoE does not induce pores even when kept in close proximity of the target membrane. Collectively, these observations indicate that similar to their smaller ND courterparts (Wu *et al.*, 2016), NLPs fuse with liposome or cell membranes in a strictly SNARE-dependent manner.

Combining data from 64 current bursts we obtained distributions for vNLP8-tCell fusion pores as shown in Figures 4.4e-f and Fig. 4.4—Figure supplement 1. The number of pore flickers and burst durations were well described by geometric and exponential distributions, respectively, with $N_{\text{flickers}} = 16 \pm 2.7$ flickers per burst and $T_o = 10.3 \pm 2.2$ s (mean ± S.E.M.), as would be expected for discrete transitions between open, transiently blocked, and closed states (Sakmann and Neher, 2009) (Fig. 4.4—Figure supplement 1).

Conductances in the open-state and corresponding radii were broadly distributed (Materials and Methods and Fig. 4.4e, f), with mean $\langle G_{po} \rangle = 450$ pS (S.E.M. = 169 pS), and $\langle r_{po} \rangle = 0.84$ nm (S.E.M $= 0.09$ nm), respectively. Surprisingly, these values were significantly less than the maximum possible value based on NLP dimensions (Fig. 4.4b). This suggested a substantial inherent resistance to pore expansion, independent of the constraints imposed by the NLP dimensions. To quantify the resistance we computed the apparent pore free energy $U(r_{\text{po}})$ from the distribution of pore radii, $P(r_{\text{po}}) \sim e^{-\frac{U(r_{\text{po}})}{kT}}$. This suggested that ~ *2* kT energy was required for every 1 nm increase in pore radius above the most likely value $r_{po} \approx 0.5$ nm (Figs. 4.4f, g).

A few SNARE complexes are sufficient to create a fusion pore, but many more are needed to dilate it

We then varied the number of SNAREs, and found that just a few SNARE complexes are sufficient to create a fusion pore, but many more are needed to dilate it. We repeated the measurements in Fig. 4.4 using NLPs loaded with total v-SNARE copy numbers ranging from 1 (vNLP1) to ~30 (vNLP30, ~15 copies per face) (Fig. 4.5). Pore nucleation required at least 2 v-SNAREs per NLP face and ~4 to reach maximal nucleation rates (Fig. 4.5a). In contrast, when $\gtrsim$ 4 v-SNAREs per NLP face were present, pore conductances (Fig. 4.5b) and radii (Fig. 4.5—Figure supplement 1b) were significantly larger than SNARE-free values and increased dramatically as the copy number per NLP face reached 15. Conductance fluctuations about the mean increased even more sharply (Fig. 4.5—Figure supplement 1a), while burst lifetimes and pore open probability showed a more gradual increase (Fig. 4.5—Figure supplement 1c,d). Thus, different numbers of SNARE complexes cooperate at the distinct stages of fusion pore nucleation and pore dilation.

Is the increase in the mean pore conductance as the SNARE copy numbers are increased (Fig. 4.5b) due to appearance of multiple small pores per NLP or due to an increase in the mean size of a single pore? The latter is much more likely, for the following reasons. First, a probe that cannot pass through small pores becomes permeant to pores when large copy number vNLPs are employed (Fig. 4.5—Figure supplement 4). If multiple small pores were present when vNLP30 are used, then the probe should equally be impermeant. The probe employed was N-methyl-D-glucamine ($NMDG^+$), a large ion $\sim 1.1 \times 0.5$ nm in size without its hydration shell (Melikov *et al.*, 2001), which replaced sodium in the pipette solution. Conductance was low when ~15 nm MSP nanodiscs with 8 copies of v-SNAREs (vMSP8) were used (Wu *et al.*, 2016), but not affected when ~23 nm NLPs bearing 30 v-SNAREs were employed (vNLP30). These results are consistent with those of Bello et al. who showed that progressively larger cargo could be released from t-SNARE liposomes during fusion with vNLPs as the v-SNARE copies per NLP was increased (Bello *et al.*, 2016). Second, conductance of n small pores in a single NLP would be additive, giving total conductance equal to $G_{po} = n \times g_{po}$, where g_{po} is the mean open-pore conductance of a small pore. Doubling the SNARE copies would presumably at most double n, and by consequence, total conductance. The fact that we find faster than linear increase in mean pore conductance (Fig. 4.5b) is consistent with each NLP bearing a single pore whose size increases with increasing SNARE copies. Third, if multiple small pores occurred per NLP, this should be evident in the distribution of point-by-point conductance values, with peaks at $n \times g_{po}$, where $n = 1, 2, 3$ .... Instead, for the distribution of mean G_{po} for vNLP30 we find a peak at ~300 pS, and a broad peak at ~3-14 nS (Fig 4.6b). If the typical small pore has 300 pS conductance, then to have ~6 nS (typical large conductance), there would have to be ~20 small pores per NLP. It is hard to imagine this many pores coexisting in this small area. Finally, unless the multiple pores occurred simultaneously, we would also find the fusion rate to incrase with copy numbers. Instead, the rate saturates above ~ 4 copies (Fig. 4.5a). In conclusion, although we cannot rule out that very occasionally, a small number of pores may simultaneously appear in a single NLP, all the evidence suggests this cannot be very common.

Previous reports suggested (Fdez *et al.*, 2010; Shi *et al.*, 2012; Wu *et al.*, 2016) that pore nucleation is promoted by the assembly of the v- and t-SNARE TMDs. To test whether pore dilation also required the TMDs, we replaced the v-SNARE TMDs with lipid anchors (Shi *et al.*, 2012). We used long-chain anchors that span both leaflets of the bilayer, since previous work suggested lipid anchors spanning a single leaflet are not efficient to induce full fusion (McNew *et al.*, 2000; Chang *et al.*, 2016). Lipid-anchoring VAMP2 into NLPs significantly reduced pore nucleation frequency and increased the mean burst duration (Fig. 4.5—Figure supplement 2a, b, e), consistent with previous work using smaller MSP NDs (Wu *et al.*, 2016) and with reduced overall fusion efficiency reported for lipid-anchored VAMP2 (Shi *et al.*, 2012; Chang *et al.*, 2016). Importantly however, FPs induced by lipid-anchored v-SNAREs displayed the same trends as their intact counterparts: with increasing VAMP2-C45 copy numbers, mean conductance, fluctuations, burst lifetimes, and pore radii increased, but the pore open probability during a burst varied little (Fig. 4.5—Figure supplement 2). These results suggest that specific interactions between v-SNARE and t-SNARE TMDs are not critical for cooperative pore dilation by SNARE proteins.

The target membrane during exocytosis (where the t-SNAREs reside) is the inner leaflet of the plasma membrane which is rich in acidic phospholipids. In contrast, in our vNLP-tCell fusion assay, the target membrane is the outer leaflet of the plasma membrane which is largely devoid of negatively charged lipids. In general, a limitation of our system is that the lipid composition of the outer leaflet of the t-SNARE-presenting cell differs substantially from that of the plasma membrane inner leaflet, and lipid composition can play a key role in fusion. To test whether the target membrane composition affected fusion, we swapped the locations of the v- and t-SNAREs and fused flipped v-SNARE cells with t-SNARE NLPs. This allowed us to have a better mimic of the inner plasma membrane leaflet composition on the target membrane (now the tNLP membrane). This swap resulted in similar fusion rates and pore properties for two different SNARE copy numbers per NLP (Fig. 4.5—Figure supplement 3), suggesting that fusion mediated by SNAREs alone may not be very sensitive to target membrane composition within a certain range (Stratton *et al.*, 2016).

Interestingly, the increased mean pore conductance as v-SNARE copy numbers are increased does not occur homogeneously across all pores. For vNLPs bearing 4 or more total copies of v-SNAREs, we found two types of fusion pores. Most had small mean conductance $\lesssim$ 1 nS, but with increasing SNARE load, an increasing fraction of pores had much larger conductances of a few nS (Fig. 4.6a). In contrast, for NLPs that contained 0 or 1 copy of

VAMP2, the pores that occasionally occurred all had small mean conductance $\lesssim 1$nS. The distribution of mean conductances for individual pores revealed two components for vNLP30 (Fig. 4.6b), with a sharp peak at ~300 pS (71% of total mass), and a much broader population centered at 7.21 nS, separated at ~1 nS. Conductance fluctuations increased sharply for larger pores with $\langle G_{po} \rangle \gtrsim 1$ nS (Fig. 4.6—Figure supplement 1), indicating a change in behavior above this threshold. Thus, multiple criteria indicated ~1 nS as a cut-off that separated small and large pores. We applied this cut-off to all NLPs tested and clustered pore conductances in each NLP group into low ($\langle G_{po} \rangle < 1$ nS) and high conductance ($\langle G_{po} \rangle > 1$ nS) states (Fig. 4.6c). The occurrence of high conductance pores increased with increasing SNARE copy number, suggesting dilation of the pores to >1 nS (corresponding to $r_{po} \approx 1.7$ nm) is facilitated by SNARE crowding.

We defined the pore dilation probability, $P_{dilation}$, as the fraction of pores in the high-conductance state for a given SNARE copy number (Fig. 4.6c), and plotted $P_{dilation}$ as a function of v-SNARE copies per face (Fig. 4.6d). Even at the maximum SNARE load of ~15 copies per face, $P_{dilation}$ was ~0.30, far from saturating. To estimate how many SNARE complexes would be required to reach saturation, we assumed the ratio between the probabilities of high and low conductance states, $P_{dilation}/(1 - P_{dilation})$ is equal to a Boltzmann factor $e^{-\Delta E/kT}$, with ΔE the difference between the energy levels of the two conductance states, and kT thermal energy. Making the simplest assumption that $\Delta E \propto N_{SNARE} - N_0$, where N_{SNARE} is the number of SNARE complexes involved and N_0 is the copy number that would make $P_{dilation} = 0.5$, we found N_0 =19.3 (Fig. 4.6d). Thus, pore dilation with $P_{dilation} = 0.90$ would require $N \approx 30$ complexes (Fig. 4.6d, open black circle), about 10-fold more than required for nucleation (Fig. 4.5a).

SNARE crowding generates entropic forces that drive pore expansion

The characteristic fusion pore free energy function $U(r_{po})$ progressively softened as the SNARE copy number increased (Fig. 4.7a). The minimum at $r_{po} \approx 0.5$ nm did not shift, but for larger pore radii the slope decreased and the profile broadened. These free energy profiles quantify how fusion pore dilation is driven by SNARE proteins. For example, an energy ~ 6 kT is required to expand the 1 SNARE fusion pore from its preferred radius of ~ 0.5 nm to a 3-fold larger pore, showing that such an expansion is unlikely to occur spontaneously. On the other hand, with 4 SNAREs per face the same expansion requires only ~ 3 kT, and only ~ 2 kT with 15 SNAREs (Fig. 4.7a), bringing the expansion within reach of spontaneous fluctuations. The broad and shallow profile suggests a fully developed pore would then result, were the NLP replaced by a vesicle as in the physiological setting (Fig. 4.7a). These effects can equivalently be phrased in terms of force: ~ 24 pN opposes pore expansion with 1 SNARE, but this is lowered to ~ 8 pN and ~ 5 pN by 4 and 15 SNAREs per face, respectively.

To help elucidate the molecular mechanism underlying SNARE-mediated pore dilation we developed a coarse-grained mathematical model that assumed the bilayer-SNARE system is equilibrated, consistent with the long-lived current bursts so that $U(r_{po})$ is then the true thermodynamic free energy (see Materials and Methods and Table 4.1 for model parameters). In our model, for a given pore size the free energy represents an average over possible fusion pore heights, pore shapes and SNARE complex conFigurations. SNAREs can be fully zippered at the fusion pore waist, or they may unzipper and roam (Fig. 4.7—Figure supplement 1).

Table 4.1. Parameters used in the analytical model of fusion pores.

Symbol	Meaning	Value	Legend
b	Thickness of SNARE bundle	2 nm	**(A)**
$\varepsilon_{\mathrm{zip}}$	Energy of zippering of v- and t-SNAREs	9.6 kT	**(B)**
δ	Thickness of the plasma membrane	5 nm	**(C)**
D	NLP diameter	24 nm	**(D)**
λ	Decay length for inter-membrane steric-hydration force	0.10 nm	**(B)**
P_0	Pressure prefactor for inter-membrane steric-hydration force	5.0×10^{11} dyn/cm^2	**(E)**
τ	Torque per unit length to twist the ApoE proteins at the NLP boundary	8.43 pN	**(B)**
κ	Bending modulus of the lipid bilayer	20 kT	**(F)**
γ	Membrane tension	0.66 pN nm^{-1}	**(B)**
Ω_z	Solid angle explored by bending of zippered SNAREs	0.05 sr	**(G)**

(A) Measured by fitting a cylinder to the part of the fully zippered SNARE protein structure sans the TMDs produced using PyMOL software with PDB code 3HD7 (http://www.pymol.org).
(B) Estimated in this study as a fitting parameter.
(C) Measured in ref. (Mitra *et al.*, 2004).
(D) Measured in this study (Fig. 4.1).
(E) Calculated using a weighed average of the P_0 of palmitoyl-2-oleoyl phosphatidylcholine (POPC) and 1,2-dioleoyl phosphatidylserine (DOPS) from (Rand and Parsegian, 1989). The weighed average of the two pressure parameters according to the 85:15 molar ratio of POPC:DOPS present in the NLPs in this study to obtain P_0. We assumed that the hydration properties of POPC are the same as 1,2-dioleoyl phosphatidylcholine (DOPC).
(F) Values of κ in previous studies range from 10-50 kT (Brochard and Lennon, 1975; Cohen and Melikyan, 2004; Marsh, 2006; Khelashvili *et al.*, 2013). A commonly used value in studies is $\kappa = 20$ kT (Jackson, 2009), which we used here.
(G) Calculated based on an atomistic molecular dynamics study of the t-SNARE TMD that shows that these explore angles ~10^0 around their equilibrium position in a bilayer (Knecht and Grubmuller, 2003).

The model free energies reproduced experimental profiles with physiologically realistic parameters (Fig. 4.7b). Protein-free pores resisted expansion because a bigger pore has greater area: a 1 nm increase in pore radius required ~ 3.0 kT work against membrane tension and increased membrane bending energy by ~ 2.4 kT. Thus, a net force ~ 22 pN resists pore expansion, close to the experimental value of ~24 pN (Fig. 4.7a). When SNAREs were present, zippering of SNARE linker domains (Gao *et al.*, 2012) and TMDs drove several SNAREs to fully assemble at the fusion pore waist, where crowding generated an entropic pore expansion force (Fig. 4.7c). Bigger pores were associated with more zippered SNAREs at the waist (Fig. 4.7—Figure supplement 1). With 15 SNAREs per face the entropic expansion force of 17 pN was within 5 pN of the 22 pN resistance.

Consistent with our experiments using lipid-anchored v-SNAREs, when we ran the model with lowered excluded volume among zippered SNAREs to mimic the lipid anchor, the best fit total zippering energy was reduced by $< 1\ kT$ (see Materials and Methods). This suggests that the driving force for SNARE zippering that underlies pore expansion does not rely on putative v- and t-SNARE TMD interactions, but has a significant contribution from non-specific interactions favoring alignment of membrane anchors.

Discussion

In summary, we find that a few SNAREs can nucleate a fusion pore, consistent with previous findings (Karatekin *et al.*, 2010; Mohrmann *et al.*, 2010; van den Bogaart *et al.*, 2010; Sinha *et al.*, 2011; Shi *et al.*, 2012; Bao *et al.*, 2016), but the pore is highly unlikely to expand significantly without additional forces. Pore dilation is resisted by intrinsic bilayer properties (Chizmadzhev *et al.*, 1995; Chanturiya *et al.*, 1997; Jackson, 2009), but promoted by the action of many SNAREs that cooperatively exert expansion forces of entropic origin (Fig. 4.7c).

In our study, pores fluctuated in size, and closed and opened (flickered) multiple times before resealing, similar to exocytotic fusion pores recorded from neuroendocrine cells or neurons (Klyachko and Jackson, 2002; Lindau and de Toledo, 2003; Staal *et al.*, 2004; Fulop *et al.*, 2005; He *et al.*, 2006). Each such burst lasted several seconds on average. Confinement of the pore radius by the NLP scaffold to $\lesssim 7-8$ nm likely contributed to this long lifetime. However, we suggest the lifetime also reflects the natural tendency of small pores to resist dilation, for the following reasons. First, the most likely pore radius, ~0.5 nm (Fig. 4.4f and 4.7a), is much smaller than the maximum allowed by the NLP geometry, ~7-8 nm. Second, fusion pores connecting protein-free bilayers flicker for seconds, and do not dilate unless increased membrane tension is applied (Chanturiya *et al.*, 1997). Third, pores lasting on the order of a second or longer have been documented during exocytosis using capacitance recordings, e.g. from beta cells secreting insulin (MacDonald *et al.*, 2006; Hanna *et al.*, 2009), or during synaptic vesicle fusion (He *et al.*, 2006). Amperometry often reports shorter pore lifetimes compared to capacitance measurements (Chang *et al.*, 2015); it may underestimate pore lifetimes since no signal can be observed once all cargo is released. It is also possible that a pore can reseal after partial dilation giving rise to an amperometric spike, leading to an underestimation of pore lifetime based on the pre-spike foot feature alone (Mellander *et al.*, 2012). Fourth, a recent FRET-based study suggested existence of long-lived, narrow fusion pores during neuronal SNARE-driven fusion between surface-tethered liposomes, dilation of which was promoted by Synaptotagmin-Ca^{2+} and Complexin (Lai *et al.*, 2013). Finally, various theoretical models suggested small pores to be metastable (Nanavati *et al.*, 1992; Chizmadzhev *et al.*, 1995; Jackson, 2009).

We measured a low fusion efficiency in our assay (4-5% of docked NLPs undergo lipid mixing in ~20 min, Fig. 4.2—Figure supplement 1), possibly due to the absence of factors known to be essential for exocytosis in our assay. Indeed, the low fusion efficiency in SNARE-only reconstitutions lacking other factors such as Munc13 that are required *in vivo* for exocytosis is well documented (Weber *et al.*, 1998; Diao *et al.*, 2013; Hernandez *et al.*, 2014; Bao *et al.*, 2016; Bello *et al.*, 2016; Liu *et al.*, 2016). Another possibility is that the NLPs that actually fuse may be biased toward higher copy numbers of proteins, if higher copy number corresponded to higher fusion rates. While we cannot categorically exclude this possibility, we think it unlikely. First, the fusion rates we measured were statistically indistinguishable for copy numbers ≥ 4 (vNLP4, vNLP8, vNLP15 and vNLP30, Fig. 4.5a). Thus, there is no evidence of a bias due to differential fusion rates. Second, even if there were such a bias, our results would still correctly report the general trend of pore properties versus copy number as can be seen from the following argument. Assume a Poisson distribution for the copy number up to a maximum of 30, the maximum attainable value in our experiments (presumably a packing constraint). Then for large mean copy numbers this distribution has a small width, so that even if the ~ 5% fused fraction corresponds to the tail of this distribution the copy numbers involved will not be much greater than the mean value. Thus, the typical copy number of the NLPs whose pore properties are measured would still be an increasing function of the mean value.

A wide range of SNARE copy number requirements for fusion have been reported in the literature (Montecucco *et al.*, 2005; Domanska *et al.*, 2010; Karatekin *et al.*, 2010; Mohrmann *et al.*, 2010; van den Bogaart *et al.*, 2010; Sinha *et al.*, 2011; Shi *et al.*, 2012; Hernandez *et al.*, 2014; Bao *et al.*, 2016), depending on the system studied and the read-out used for fusion. Most studies concluded that only a few copies of neuronal SNAREs are sufficient for calcium-triggered exocytosis and fusion of small liposomes (Domanska *et al.*, 2010; Karatekin *et al.*, 2010; Mohrmann *et al.*, 2010; van den Bogaart *et al.*, 2010; Sinha *et al.*, 2011; Shi *et al.*, 2012; Bao *et al.*, 2016). Despite this, the average synaptic vesicle carries 70 v-SNARE copies (Takamori *et al.*, 2006) and at least as many t-SNAREs are clustered at plasma membrane docking and fusion sites in neuroendocrine cells (Knowles *et al.*, 2010). Our results provide a rationalization for this situation, as they suggest that reliable pore dilation may require engagement of many SNARE complexes. As the demands for SNARE cooperativity may be different at different stages of the fusion reaction, interpretation of copy number requirements should be made with caution. Methods that rely on lipid mixing or exchange of small ions through pores (e.g. capacitance or pH sensing) may measure the requirement for opening of small fusion pores, which may differ substantially from the requirements for pore dilation.

The action of SNAREs is highly regulated by other proteins during neurotransmitter or hormone release (Sudhof and Rothman, 2009). In addition to manipulations of SNAREs (Han *et al.*, 2004; Kesavan *et al.*, 2007; Fang *et al.*, 2008), mutations in Munc18 (Jorgacevski *et al.*, 2011), Synaptotagmin (Wang *et al.*, 2001; Wang *et al.*, 2003a; Wang *et al.*, 2003b), and complexin (Dhara *et al.*, 2014) affect fusion pore properties, linking these proteins to pore dynamics. Thus, one must be cautious when extending our SNARE-only results to physiological neurotransmitter and hormone release. Nevertheless, the concept of protein crowding promoting pore dilation is a general principle that may hold qualitatively in the presence of additional components of the physiological fusion machinery. Indeed, a previous study indicated that availability of SNAREs affects neurotransmitter release kinetics in neurons (Acuna *et al.*, 2014), while another suggested release occurred faster at sites with more t-SNAREs (Zhao *et al.*, 2013). Thus, we tentatively suggest that some proteins may exert their exocytotic regulatory function by organizing SNARE complexes around the fusion site and thereby controlling the number that participate, or by sequestering SNAREs to limit that number. Given the steep dilation probability curve (Fig. 4.6d), our results suggest a high sensitivity in the balance between transient *versus* full fusion.

Materials and Methods

Stable flipped SNARE and wild-type HeLa cell culture.

HeLa cell lines stably co-expressing flipped v-SNAREs (flipped VAMP2 and cytosolic DsRed2-nes, “vCells”) and t-SNAREs (flipped Syntaxin 1 and flipped SNAP-25 and the nuclear fluorescent marker CFP-nls, “tCells”) were generated in the Rothman laboratory as described (Giraudo *et al.*, 2006). The cells were a generous gift from the Rothman laboratory. The cells were maintained in DMEM (4500 mg/L glucose, L-glutamine, sodium pyruvate and sodium bicarbonate) and 10 % (v/v) fetal calf serum at 37ºC. A new aliquot of cryopreserved cells was thawed after at most three weeks of cell culture and cultured at least five days before data acquisition.

The flipped t-SNARE HeLa cells were tested by PCR Mycoplasma Test Kit I/C (cat. No. PK-CA91-1048, Promo Kine, Heidelberg, Germany) which showed contamination (Fig. 4.4—Figure supplement 3A). Because our assay fuses discs to the surface of these cells, no effect of mycoplasma contamination is expected. Indeed the controls in Figures 4.2-4 indicate fusion is SNARE-driven. Nevertheless, we tested any possible impact of mycoplasma contamination on our results, by repeating some of our single-pore measurements with cells treated with an antimycoplasma reagent (Plasmocin, cat. code ant-mpt, InvivoGen, California, USA). Fusion rates and pore properties were indistinguishable when untreated or treated cells were used (Fig. 4.4—Figure supplement 3, B-E), suggesting mycoplasma contamination does not affect fusion with NLPs.

Plasmids, protein expression and purification

Expression and purification of the t-SNARE complex used in vND-tSUV fusion experiments is described in Parlati *et al.* (Parlati *et al.*, 1999). The cytoplasmic domain of VAMP2 (CDV) was produced similarly to an earlier protocol (Weber *et al.*, 1998), except a SUMO vector was used. We followed Giraudo *et al.* (Giraudo *et al.*, 2006) for expression and purification of the tetanus neurotoxin light chain TeNT. VAMP2 proteins were expressed and purified as described earlier (Shi *et al.*, 2012). To produce full length WT VAMP2, we used the plasmid pET-SUMO-VAMP2 (Shi *et al.*, 2012). For producing lipid-anchored VAMP2, we followed McNew et al. (McNew *et al.*, 2000) and Shi et al. (Shi *et al.*, 2012). We first used a previously described construct (McNew *et al.*, 2000) to produce VAMP^{95}Cys containing the entire cytoplasmic domain of VAMP2 (residues 1-95) with a C-terminal cysteine residue. We then coupled this protein to maleimidopropionic acid solanesyl ester (maleimide-C45), produced as previously described (Shi *et al.*, 2012). For producing MSP NDs, we used the vector pET28-MSP1E3D1 (Addgene) to express and purify MSP1E3D1 as described previously (Ritchie *et al.*, 2009), except we cleaved the MSP proteins directly off the column by TEV protease overnight at 4 °C (Wu *et al.*, 2016).

Plasmid pET32a-Trx-His6X-ApoE422K to express the N-terminal 22 kDa fragment of apolipoprotein E4 (residues 1-199) was kindly provided by Dr. Nicholas Fischer, Lawrence Livermore National Laboratory, CA (Morrow *et al.*, 1999; Blanchette *et al.*, 2008). ApoE422K was expressed and purified as previously described (Morrow *et al.*, 1999) with the following modifications: The His6-ApoE422K was cleaved off the Ni-NTA beads (Qiagen) using 100U of Thrombin at 4 °C overnight. The protein was eluted in 25 mM HEPES, 140 KCl, pH 7.4 buffer containing 1% octylglucoside (OG), and was functional up to 4 weeks when stored at 4 °C. Protein concentrations were determined using the Bradford assay (Bio-Rad) with bovine serum albumin as standard.

Characterization of nanolipoprotein particles (NLP).

Details are provided by Oscar et al. (Bello *et al.,* 2016). Briefly, nanolipoprotein particles containing VAMP2 (vNLP) were produced using a modified version of the established protocol to generate SNARE-nanodiscs (Shi *et al.*, 2012; Shi *et al.*, 2013). A palmitoyl-2-oleoylphosphatidylcholine (POPC): 1,2-dioleoyl phosphatidylserine (DOPS) = 85:15 molar ratio lipid mixture (Avanti Polar Lipids) was dried under nitrogen flow, followed by vacuum for 1 hour. The lipid film was re-suspended in 25 mM HEPES, pH 7.4, 140 mM KCl, buffer with 1% OG supplemented by the desired amount of VAMP2. The mixture was vortexed at room temperature (RT) for 1 hour followed by the addition of ApoE422K and vortexed another hour at RT. The ApoE422K:VAMP2:lipid ratio was varied to tune the v-SNARE copy number per NLP as 1:0.2:180 (1 VAMP2, “vNLP1”); 1:1:180 (4 copies, “vNLP4”); 1:2:180 (8 copies, “vNLP8”); 1:4:180 (15 copies, “vNLP15”) and 1:8:180 (30 copies, “vNLP30”). NLPs containing 1, 4 and 15 copies of VAMP-C45 were obtained using a similar approach. Excess detergent was removed using SM-2 bio-beads (Bio-Rad) overnight at 4°C with constant mixing. The assembled v-NLPs were separated from free proteins and lipids via gel filtration on a Superose 6 column (Fig. 4.1a). Samples were concentrated using Amicon Ultra (50 KDa cutoff) centrifugal filter units, and analyzed by SDS-PAGE with Coomassie staining (Fig. 4.1b). The number of VAMP2 copies per disc was determined by the VAMP2-to-ApoE ratio by densitometry using ImageJ (NIH). The number of ApoE copies per disc was estimated (Bello *et al.*, 2016) using the calibration of disc size vs number of ApoE copies previously reported (Blanchette *et al.*, 2008). The size distribution of the v-NLPs were determined for every batch of production using transmission electron microscopy. To do this, the NLP discs were diluted (1:50) and mounted onto carbon-coated 400 mesh copper electron microscopy grids and negatively stained with 2 % uranyl acetate (w/v) solution, and subsequently examined in an FEI Tecnai-12 electron microscope operated at 120 kV. Micrographs of the specimen were taken on a Gatan Ultrascan4000 CCD camera at a magnification of 42,000. Typical micrographs and a size distribution are shown in Figure 4.1c,d. The size of the NLP discs with 1:180 ApoE422K: lipid ratio was typically 24 ± 2 nm (100-200 NLP discs were analysed for every production batch). Representative size distributions are shown as box plots for the conditions tested in Figure 4.1e. At least three independent batches of NLPs were used per condition. tNLPs were produced in a similar fashion, using a t-SNARE:ApoE:lipid ratio of 0.8:1:180 and 3:1:180 for tNLP4 (4 copies of t-SNARE complex Stx/SN25 total per NLP) and tNLP 15 samples (15 total copies of t-SNAREs per NLP), respectively.

Bulk fusion of NLPs with t-SNARE liposomes.

We used a previously established (Shi *et al.*, 2012; Bello *et al.*, 2016) assay to monitor release of calcium from t-SNARE reconstituted small unilamellar vesicles (t-SUVs) as they fused with discs loaded with v-SNAREs. 40 μl t-SUVs entrapping 50 mM calcium were mixed with 5 µl vMSP NDs (prepared as described previously (Shi *et al.*, 2012)) or 10 µl of vNLP-discs in a buffer containing 2 µM of the calcium-sensitive dye mag-fluo-4 (Invitrogen). The mixture was loaded into a 96 well plate, and the mag-fluo-4 fluorescence (λ_{ex}= 480 nm, λ_{em}=520 nm, 515 cutoff) was recorded by a SpectraMax M5 plate reader (Molecular Devices). After 60 minutes, 15 µl of 5 % dodecylmaltoside was added and the mixture incubated an additional 20 min to release all remaining entrapped calcium to establish the maximum mag-fluo4 signal. Fusion is reported as percent of maximum fluorescence in Figure 4.1—Figure supplement 1.

Single-cell lipid mixing and calcium influx assays.

These were carried out as described in Wu et al. (Wu *et al.*, 2016). Briefly, for lipid mixing, tCells were plated in 35 mm poly-D-lysine coated glass bottom dishes (MatTek Corporation, MA, USA) and vNLP8 were prepared as described above, except 1 mole % each of 1,1'-dioctadecyl-3,3,3',3'-tetramethylindocarbocyanine perchlorate (DiI, cat. no. D282, Molecular Probes, Eugene, OR) and 1,1'-dioctadecyl-3,3,3',3'-tetramethylindodicarbocyanine perchlorate (DiD, cat. no. D307, Molecular Probes) fluorescent lipid labels were included in the lipid composition. For each reaction, 15 µl of vNLP8 was added onto tCells (final NLP lipid concentration was ~54 µM) and incubated for 30 min at 4 ℃, a temperature at which SNARE complexes assemble, but cannot drive fusion (Weber *et al.*, 1998). Fusion was started by raising the temperature to 37 ℃ and monitored by the dequenching of the DiI fluorescence using confocal microscopy. As controls, empty nanodiscs (eNLP) or NLPs bearing VAMP2-4X (harboring the mutations L70D, A74R, A81D, L84D) were used (Fig. 4.2b). To estimate the extent of lipid mixing, at the end some experiments DiD fluorescence was completely bleached using direct excitation at 647 nm with 100 % laser power. This resulted in the maximum possible donor (DiI) intensity, F_{max}. We then rescaled the donor fluorescence values $F(t)$ to obtain the fraction of maximum DiI fluorescence: $\widetilde{F(t)} = (F - F_0)/(F_{max} - F_0)$, where F_0 is the minimum at the beginning of acquision.

To assess lipid mixing, we also used an alternative protocol that avoided the cold incubation step, but could not be used for time course measurements because of the high background due to excess NLPs. The same amount of vNLP8 as above was added to tCells at 37 ℃. After 15 min incubation, excess NLPs were washed, and DiI, DiD and CFP fluorescence were acquired using confocal microscopy (Fig. 4.2c,d).

To measure the influx of calcium through fusion pores, tCells were loaded with 5 µM of Fluo-4 AM (life technologies, NYC, USA), a cell-permeant calcium-sensitive fluorescent dye, as previously described (Wu *et al.*, 2016). After washing to remove dye not taken by cells, vNLP (15 µl) were added to tCells at 37 °C and the influx of calcium was tracked by imaging of Fluo-4 fluorescence using a confocal microscope (Wu *et al.*, 2016).

Electrophysiology.

Details are given in Wu et al. (Wu *et al.*, 2016). Briefly, flipped t-SNARE HeLa cells (tCells) were cultured in 3 cm dishes. For recordings, a dish was placed in a temperature controlled holder (TC-202A by Harvard Apparatus, or Thermo Plate by Tokai Hit) set at 37℃. Cells were visualized with an inverted microscope (Olympus IX71, Olympus Corp.) using an Andor DU-885K EMCCD camera controlled by Solis software (Andor). Recording pipettes (borosilicate glass, BF 150-86-10, Sutter Instruments) were pulled using a model P-1000 pipette puller (Sutter Instruments) and polished using a micro-forge (MF-830, Narishige). Pipette resistances were 5–10 MΩ in NaCl-based solution. The bathing medium contained (in mM): 125 NaCl, 4 KCl, 2 CaCl2 1 $MgCl_2$, 10 HEPES, (pH adjusted to 7.2 using NaOH) for the cell-attached recordings.

10 mM glucose was added to the medium before use. All voltage- and current-clamp recordings were made using a HEKA EPC10 Double USB amplifier (HEKA Electronics, Inc.), controlled by Patchmaster software (HEKA). Currents were digitized at 20 kHz and filtered at 3 kHz.

To measure SNARE-mediated single fusion pore currents in the cell-attached mode (Yang and Sigworth, 1998), electrodes were filled with the pipette solution composed of (in mM) 125 NaCl, 4 KCl, 10 HEPES, 13 or 26 tetraethylammonium-Cl (TEA-Cl, K^+-channel antagonist), adjusted to pH 7.2 using NaOH. This solution had resistivity 0.60 Ohm.m, measured using a conductivity cell (DuraProbe, Orion Versa Star, Thermo Scientific). For experiments designed to test the presence of multiple pores connecting large copy number vNLPs to tCells (Fig. 4.5—Figure supplement 4), electrodes were filled with a solution containing (in mM): 129 N-methyl-d-glucamine (NMDG), 10 HEPES, 26 TEA-Cl, pH adjusted to 7.2 using HCl, resistivity 0.88 Ohm.m, 305 mOsm. The pipette tip was initially filled with 1 μl of NLP-free buffer and back-filled with vNLPs suspended in the same buffer (final [vNLP]=100 nM, 120 μM lipids). This allowed establishing a tight seal ($R_{seal} > 10$ GOhm) with high success rate and recording a stable baseline before the vNLPs diffused to the membrane patch and started fusing with it 2-18 min later. Such a back-filling strategy is typically used in perforated patch measurements (Sakmann and Neher, 2009). All cell-attached recordings were performed using a holding potential of -40 mV relative to bath. With a cell resting membrane potential of -56 ± 7 mV (mean ± S.D., n=36), this provided 16 mV driving force across the patch membrane.

Analysis of fusion pore data

Analysis of fusion pores is described in detail in Wu et al. (Wu *et al.*, 2016). Briefly, we developed an interactive graphical user interface in Matlab to help identify, crop and process single fusion pore currents. Traces were exported from Patchmaster (HEKA Electronik) to

Matlab (Mathworks), low-pass filtered (280 Hz cutoff) and frequencies due to line voltage were removed using notch filtering. Zero phase shift digital filtering algorithms (Matlab Signal Processing Toolbox function filtfilt) were employed to prevent signal distortion. Filtered traces were averaged in blocks of 80 points (125 Hz final bandwidth) to achieve rms baseline noise $\lesssim$ 0.2 pA. Currents I for which $|I| > 2.0$ pA for at least 250 ms were accepted as fusion pore current bursts. During a burst, rapidly fluctuating currents often returned to baseline multiple times, i.e. pores flickered. To quantify pore flickering, we defined currents < -0.25 pA and lasting $\geq$ 60 ms (15 points) as open pores and currents not meeting these criteria as closed. For a given burst, the number of open periods was equal to the number of flickers, $N_{flickers}$. To estimate the fusion rate for each recording (i.e. the rate at which current bursts appeared), we counted the number of current bursts that fit the set criteria (current amplitude >2 pA for at least 250 ms) and divided this number by the duration of the recording. Rates from different records (patches) were averaged for each condition. We also refer to this rate as the pore nucleation rate. Periods during which the baseline was not stable were excluded from this analysis. Many recordings ended with what seemed to be currents from overlapping fusion pores. Such end-of-record currents were also excluded, since they could also be attributed to a loose seal. Thus, the fusion rates we report may underestimate the true rates, especially for conditions where fusion activity was high. For distributions of conductances and radii, we used pore open-state values, denoted by the subscript “po”. For Figure 4e,f, we first computed the probability density functions (PDFs) for individual pores using a fixed bin width for all, then averaged these to give equal weight to all pores. All distribution fitting was performed using Matlab Statistics Toolbox functions fitdist or mle, using maximum likelihood estimation. Open-pore conductance values were used point-by-point to estimate the open-pore radii, by approximating the pore as a cylinder and using the expression (Hille, 2001) $r_{po} = \left(\rho\lambda G_{po}/\pi\right)^{1/2}$, where ρ is the resistivity of the solution, $\lambda = 15$ nm is the length of the cylinder, and G_{po} is the open-pore conductance. For assessing statistical significance when comparing sample means, we used the two-sample t-test, or the nonparametric two-sample Kolmogorov-Smirnov test (ttest2 or kstest2, Matlab Statistics Toolbox), as indicated in Figure legends. We considered each single-pore measurement a biological replicate.

For clustering average single-pore conductances $\langle \mathrm{G_{po}} \rangle$ for vNLP30 measurements, we used a 2-component Gaussian mixture model (Figure 4.6b) which indicated a boundary between the two components at ~1 nS. Applying this cutoff to all vNLP samples we produced the boxplot in Fig. 4.6c, where on each box the central red line marks the median, the edges of the box are the 25th and 75th percentiles, and the whiskers extend from q3 + 1.5(q3 – q1) to q1 – 1.5(q3 – q1), where q1 and q3 are the 25th and 75th percentiles, respectively. For a given v-SNARE copy number per NLP face, N_{SNARE}, we defined the probability $P_{dilation}$ of achieving a high-conductance pore ($\langle G_{po} \rangle > 1$ nS) as the fraction of high conductance pores observed for that copy number. For example, only 3 out of 64 pores were large conductance for vNLP8 which had 4 copies per face (Fig. 4.6c), hence $\mathrm{P_{dilation}}(\mathrm{N_{SNARE}} = 4) = 3/64$. We plotted $\mathrm{P_{dilation}}$ as a function of v-SNARE copy number per NLP face in Figure 4.6d. In Figure 4.7a, for estimating the energy profiles of fusion pores for a given v-SNARE copy number, we first calculated the probability density function for open-pore radii as in Figure 4.4f. The probability P_r that the radius is between r and $r + \Delta r$ is the density at that bin × Δr, where Δr is the bin width. We estimated the energy $U(r)$ of a pore with radius r by $\mathrm{U/kT} = -\ln(\mathrm{P_r}) + \mathrm{A}$, where A is an arbitrary constant.

Mathematical model of the fusion pore between a nanodisc and planar membrane in the presence of SNAREs.

Membrane free energy.

We modeled the fusion pore as having a toroidal shape formed between a nanolipoprotein particle (NLP) modeled as a planar bilayer of diameter D and the tCell membrane modeled as an infinite planar bilayer, both of which are at a constant membrane tension (Fig. 4.7c). This toroidal assumption is similar to previous theoretical studies that assumed a toroidal shape of the fusion pore (Kozlov *et al.*, 1989; Chizmadzhev *et al.*, 2000; Jackson, 2010). Experimental studies also observed an hourglass shaped fusion pore that could be considered approximately toroidal (Curran *et al.*, 1993; Haluska *et al.*, 2006).

The fusion pore is parametrized by the toroidal shape parameters: the radius of the toroid r_{po} which corresponds to the fusion pore radius r_{po} and the separation of the membranes at the edge of the NLP h. The fusion pore is completely toroidal at small pore sizes. The free energy of the fusion pore is calculated using the Helfrich energy form as was used in previous studies (Kozlov *et al.*, 1989; Chizmadzhev *et al.*, 2000; Jackson, 2010)

$$U_{\mathrm{mb}}(r_{\mathrm{po}}, h) = U_{\mathrm{bend}}(r_{\mathrm{po}}, h) + \gamma \Delta A(r_{\mathrm{po}}, h) \tag{4.1}$$

Here, the energy due to bending is given by

$$U_{\mathrm{bend}}(r_{\mathrm{po}}, h) = \frac{\kappa}{2}\int_{M} (2\mathrm{C})^2 dA \tag{4.2}$$

where κ, C are the bending modulus and the mean curvature of the membrane respectively. The energy expended to add membrane area due to membrane tension γ is the second term, where ΔA is the change in total membrane area due to pore formation, given by $\Delta A(r_{\mathrm{po}}, h) = A_{\mathrm{po}}(r_{\mathrm{po}}, h) -$

$A_{\mathrm{rim}}(r_{\mathrm{po}}, h)$. Here, A_{po} is the area of the fusion pore. A_{rim} is the area of both rims of the fusion pore which is the area that has to be removed from the infinite tCell membrane and the NLP membrane to form the pore. We evaluated all integrals and all areas over the midplane M of the membrane forming the pore to give

$$U_{\mathrm{bend}}(r_{\mathrm{po}}, h) = \pi\kappa \left\{ \frac{2(R+H)^2}{H\sqrt{R(R+2H)}} \tan^{-1}\left(\sqrt{\frac{R+2H}{R}}\right) - 4 \right\} \tag{4.3}$$

$$\Delta A(r_{\mathrm{po}}, h) = \pi H((2\pi - 4)H + 2\pi R) - 2\pi(H+R)^2 \tag{4.4}$$

where $H = \mathrm{h}/2 + \delta/2$ and $R = r_{\mathrm{po}} + \delta/2$. Values of κ in previous studies range from 10-50 kT (Brochard and Lennon, 1975; Cohen and Melikyan, 2004; Marsh, 2006; Khelashvili *et al.*, 2013). A commonly used value is $\kappa = 20$ kT (Jackson, 2009), which we used here (Table 4.1). γ was obtained as a best-fit parameter (Table 4.1).

Free energy due to twisting of the ApoE proteins that line the boundary of the ND.

Due to the finite size of the NLP, toroidal states are not possible for large pore with $\mathrm{r_{po}}$ and h a sizeable fraction of the NLP diameter D. These shapes are partially toroidal and come into existence when $\mathrm{r_{po}} + \mathrm{h}/2 + \delta \geq \mathrm{D}/2$ where δ is the membrane thickness. The ApoE proteins that line the NLP boundary need to be rotated through an angle ϕ to form these shapes. An example of one such shape is the right hand panel of Fig. 4.7c.

We assumed these proteins exert a constant torque τ per unit length of the NLP boundary to resist this rotation. The ApoE proteins exert no torque in the completely toroidal states as ϕ vanishes for these states. The free energy of these proteins is

$$U_{\mathrm{ApoE}}(r_{\mathrm{po}}, h) = \tau \pi D \phi \qquad (4.5)$$

$$\phi(r_{\mathrm{po}}, h) = \sin^{-1}\left(\frac{r_{\mathrm{po}} + \frac{h}{2} + \delta - \frac{D}{2}}{\frac{h}{2}}\right), r_{\mathrm{po}} + \frac{h}{2} + \delta \geq \frac{D}{2} \qquad (4.6)$$

Thus, the ApoE proteins resist pore expansion as ϕ increases with the size of the pore. We obtained τ as a fitting parameter and D was measured in this study (values in Table 4.1). For further details about the partially toroidal states, please see the penultimate subheading '*Description of partially toroidal states*'.

Free energy contribution from short-ranged steric-hydration forces.

Steric-hydration repulsion between membranes is prominent at small membrane separation. Experimentally measured steric-hydration pressures between planar membranes of separation d are of the form $\mathrm{P_0} \exp -\mathrm{d}/\lambda$ (Rand and Parsegian, 1989). Values of $\mathrm{P_0}$ and λ have been measured before for several membrane compositions; λ is within 0.1 - 0.3 nm (Rand and Parsegian, 1989). As the pore sizes over which these effects are appreciable ($\sim\lambda$) are very small compared with the NLP diameter D, only toroidal states are considered for this calculation. We obtained $\mathrm{P_0}$ from previous studies and λ as a best-fit parameter (Table 4.1).

The steric-hydration forces act in two orthogonal directions on the membranes comprising the fusion pore: to increase the pore radius $\mathrm{r_{po}}$ and the separation between membranes h. The sum of the work done by these two forces gives the free energy of the steric-hydration interaction

$$U_{\mathrm{hyd}}(r_{\mathrm{po}}, h) = P_0 \lambda \left(\frac{\pi D^2}{4}\right) \exp\left(-\frac{h}{\lambda}\right) + P_0(2\pi l) \exp\left(-\frac{2r_{\mathrm{po}}}{\lambda}\right) \left(\frac{\lambda}{2} r_{\mathrm{po}} + \left(\frac{\lambda}{2}\right)^2\right) \qquad (4.7)$$

where l is the effective pore height, i.e. the height of the section of the pore that contributes substantially to the steric-hydration interaction. To obtain the free energy contribution of the steric-hydration forces, we now calculate the work done by these forces to assemble the fusion pore. We first observe that the work done W to bring two patches of membranes of area δA to a separation h from a large distance apart is

$$W = P_0 \int_{\infty}^{h} \delta A \exp\left(-\frac{y}{\lambda}\right) dy \tag{4.8}$$

The first term in eq. 4.4.7 is the work done to separate the planar part of the membranes to a distance h. As the pore area where these forces are relevant ($\sim\lambda^2$) is very small compared with the NLP area $\pi D^2/4$, we set area of the planar region $\delta A = \pi D^2/4$ in eq. 4.8 to obtain the first term. The second term in eq. 4.4.7 is the work done to separate the membranes to form a pore of diameter $2r_{po}$. To calculate this, we can imagine that the pore is a cylinder of diameter $2r_{po}$ and height l where $l = \sqrt{2\lambda(h + 2\delta)}$, since the change in pore diameter over the height l is negligible. Here, δ is the thickness of the bilayer and l is the height over which the the cross-sectional diameter of the toroidal shape increases from $2r_{po}$ to $2r_{po} + \lambda$.

To obtain l, we consider the inner surface of the toroidal pore. This shape is formed by revolving the semicircle given by $x = (r_{po} + R') - R' \cos\theta, z = R' \sin\theta$ where $-90^0 \le \theta \le 90^0$ in the XZ plane about the Z axis. Here, r_{po} is the radius of the pore and R' is the radius of the semicircle which is also equal to half of the maximum separation between the heads of the monolayers that line the inner surface of the pore, $R' = h/2 + \delta$ as can be seen from Fig. 4.7c. $l/2$ is that value of z at which the cross-sectional radius of the pore x increases to $r_{po} + \lambda/2$.

Thus, l is obtained by solving the equation of the semicircle $\left(r_{\text{po}} + h/2 + \delta - r\right)^2 + (l/2)^2 = (h/2 + \delta)^2$ to first order in λ where $r = r_{\text{po}} + \lambda/2$.

To calculate the steric-hydration contribution from a pore of size r_{po} and height h, one need only consider the pore over that height l at which the cross-sectional diameter of the toroidal shape increases from $2r_{\text{po}}$ to $2r_{\text{po}} + \lambda$, since λ is the range of the steric-hydration force. Thus, the area of the cylinder is $\delta A(r_{\text{po}}) = 2\pi r_{\text{po}} l$ and using eq. 4.8 the work done to set up the pore is $P_0 \int_{\infty}^{2r_{\text{po}}} (2\pi l y) \exp(-y/\lambda)\, dy$, giving the second term of eq. 4.7.

<u>Free energy contribution from SNARE proteins.</u>

In this section, we calculate the free energy due to the SNARE proteins. We fix the total number of v-SNAREs. Out of these N v-SNAREs, N_z are fully zippered and N_u are partially zippered. Only the TMDs and the linker regions of these partially zippered SNAREs are unzippered. For each N, we allowed N_z and N_u to vary from 0 to N to obtain an equilibrium distribution for both. We calculated the free energy of the SNAREs for $N = 0,2,4,8,15$ which correspond to the total number of v-SNAREs per NLP face used experimentally (Fig. 4.7a). To match with experiment, we used the assumption that only half of the total number of SNAREs present in the NLP would be present on the side of the NLP that faces the tCell and that all of these SNAREs would be available to participate in fusion pore expansion.

We assumed that the fully zippered SNAREs form a ring at the waist of the fusion pore (Fig. 4.7c). Their free energy is

$$U_{\mathrm{z}}\left(r_{\mathrm{po}}, N_{\mathrm{z}}\right) = -N_{\mathrm{z}}kT\left(\ln\frac{2\pi r_{\mathrm{po}} - N_{\mathrm{z}}b}{b} + 1\right) - N_{\mathrm{z}}\varepsilon_{\mathrm{zip}} - N_{z}kT\ln\Omega_{\mathrm{z}} \qquad (4.9)$$

The first term is the positional entropy of the zippered TMDs whose diameter is b, which we measured by fitting a cylinder to the measured crystal structure (Stein *et al.*, 2009). The second term is the energy released when a partially zippered SNAREpin completes its zippering. The third term is the orientational entropy associated with the zippered SNAREs. We assume that these are very stiff cylindrical rods. Due to their high stiffness, these rods can only explore a small solid angle $\Omega_{\mathrm{z}} = 0.05$ sr (Table 4.1). We calculated this based on an atomistic molecular dynamics study of the t-SNARE TMD that shows that these explore angles ~10^{0} around their equilibrium position in a bilayer (Knecht and Grubmuller, 2003). The SNAREs fluctuate about their equilibrium orientation which we assume is the local normal to the membrane.

The free energy of the partially unzippered SNAREs is

$$U_{\mathrm{uz}}(N_{\mathrm{uz}}) = -N_{\mathrm{uz}}kT\left(\ln\frac{2\pi D}{b}\right) - N_{\mathrm{uz}}kT\ln\pi \qquad (4.10)$$

The first term is the positional entropy of the TMDs. These partially zippered SNAREs are in a Y-shape with both unzippered TMD domains on the same side of the pore, either on the vNLP or the tCell membrane. The linker domains are also unzippered and this imparts flexibility to these SNAREs (Jahn and Scheller, 2006). This orientational freedom is given by the second term. These SNAREs can adopt all orientations where they do not intersect with the membrane; this corresponds to a solid angle of π steradian. We restricted these SNAREs to a circle of radius equal to that of the NLP as this considerable orientational freedom is only available when the SNAREpin body is away from the fusion pore lumen.

Calculation of the total free energy U as a function of pore size and number of SNAREs.

The probability that a fusion pore accesses a radius $\mathrm{r_{po}}$ in the presence of N SNAREs is proportional to $\exp -\mathrm{U}(\mathrm{r_{po}}, \mathrm{N})/\mathrm{kT}$ in equilibrium, as this is the Boltzmann distribution where U is the total free energy. We assumed that the bilayer-SNARE system is equilibrated as the current bursts measured experimentally are long-lived. To calculate this free energy, we summed the Boltzmann factor of all states that comprise such a system

$$\exp\left(-\frac{U(r_{\mathrm{po}}, N)}{kT}\right) = \sum_{N_z=0}^{N} \int_b^\infty \exp\left(-\frac{U_{\mathrm{tot}}(r_{\mathrm{po}}, h, N, N_{\mathrm{z}})}{kT}\right) dh \qquad (4.11)$$

Here, $\mathrm{U_{tot}}$ is the total free energy of one fusion pore state with $\mathrm{N_z}$ zippered SNAREs and of membrane separation h, given by

$$U_{\mathrm{tot}} = U_{\mathrm{mb}} + U_{\mathrm{z}} + U_{\mathrm{uz}} + U_{\mathrm{hyd}} + U_{\mathrm{ApoE}} \qquad (4.12)$$

We performed the integration and the sum over all states in eq. 4.11 numerically in MATLAB.

Derivation of best-fit model parameters by fitting model-predicted free energy to experiment.

We performed a numerical calculation using eq. 4.11 to obtain free energy curves as a function of SNARE copy numbers and pore size. For the membrane parameters it is best to fit to data from membranes with no SNAREs. We fit the fusion pore free energy predicted by the model with no SNAREs (setting $\mathrm{N} = 0$ in eq. 4.11) to the experimentally measured curve for 1 SNARE, assuming such a pore behaves similarly to a protein-free pore. We first fit the model-predicted pore size at the minimum in the free energy to experiment by using the steric-hydration force scale λ as a best-fit parameter. We obtained the bending modulus κ from ref. (Jackson,

2009) and fit the slope following the minimum in the region $0.5 \text{ nm} \leq \mathrm{r_{po}} \leq 1.0 \text{ nm}$ using the membrane tension γ as a best-fit parameter as γ largely determines the slope beyond this minimum.

Using these parameters, we calculated the free energy versus pore radius in the presence of SNAREpins (Fig. 4.7b). As SNAREpins are introduced, the model predicts the minimum barely shifts, while the slope beyond the minimum decreases with increasing numbers of SNAREs by an amount depending on the zippering energy parameter $\varepsilon_{\mathrm{zip}}$. We selected a typical experimental curve (vNLP30) and fit the slope of the free energy from simulation to that measured from experiment for $0.5 \text{ nm} \leq \mathrm{r_{po}} \leq 2.5 \text{ nm}$ and $N = 15$ SNAREs (as vNLP30 corresponds to 15 SNAREs per face) using $\varepsilon_{\mathrm{zip}}$ as a fitting parameter and obtained $\varepsilon_{\mathrm{zip}} = 9.6 \text{ kT}$. This is higher than the zippering energy of the linker domains alone which was measured to be ~5 kT in (Gao *et al.*, 2012).

Further increases in pore size cause increases in free energy, as the fusion pore shapes are partially toroidal and the twisting torque from the ApoE proteins at the NLP boundary resists further expansion. Thus, we fit the slope of the free energy curve in this region ($4 \text{ nm} \leq \mathrm{r_{po}} \leq 4.5 \text{ nm}$) measured from simulation to that measured experimentally for $\mathrm{N} = 4$ SNAREs to obtain the torque per unit length $\tau = 8.43 \text{ pN}$ as a fitting parameter.

To understand how lipid-anchored VAMP2 affects pore dilation, we reduced the size of the zippered TMDs by 50% as the zippered SNARE complex lacks the v-SNARE TMD. This is the maximum possible reduction in the excluded volume of the zippered SNAREs. We then varied the zippering energy to ensure that the model-predicted mean pore size was invariant with respect to this reduction, consistent with the invariance in mean pore size observed in experiment

(Fig. 4.5—Figure supplement 2f). The best-fit zippering energy is 0.43 kT lower than the best-fit value obtained when both TMDs are present. This is an upper bound on the reduction in zippering energy given that we used the largest possible reduction in the excluded volume.

Description of partially toroidal states and calculation of membrane free energy

Due to the finite size of the NLP, toroidal states are not possible for large pores with $\mathrm{r_{po}}$ and h a sizeable fraction of the NLP diameter D. We instead assumed these shapes are partially toroidal. These come into existence when $\mathrm{r_{po}} + \mathrm{h}/2 + \delta \geq \mathrm{D}/2$ where δ is the membrane thickness. We set the shape of these states as follows. We constructed a toroidal pore with the shape parameters $\mathrm{r_{po}}, \mathrm{h}$, and truncated the top half of the toroid at the plane where the cross-sectional diameter of the toroid is equal to the NLP diameter (Fig. 4.7c, right panel). In these partially toroidal states, the ApoE proteins at the edge of the NLP are rotated through an angle ϕ compared with the fully toroidal states (eq. 4.6).

Evaluating the integral from eq. 4.2

$$U_{\text{bend}}(r_{\text{po}}, h, \phi) = U_{\text{bend}}(r_{\text{po}}, h, 0) + 2\pi\kappa(1 - \cos\phi) - \pi\kappa\frac{(R + H)^2 \tan^{-1}(\alpha)}{H\sqrt{R(R + 2H)}} \tag{4.13}$$

where $H = \mathrm{h}/2 + \delta/2, \mathrm{R} = \mathrm{r_{po}} + \delta/2, \tan^{-1}\alpha = \tan^{-1}\left(\sqrt{\frac{R}{\mathrm{R+2H}}}\cot\left(\frac{\pi - 2\phi}{4}\right)\right) - \tan^{-1}\left(\sqrt{\frac{\mathrm{R}}{\mathrm{R+2H}}}\right)$,

and $\mathrm{U_{bend}}(\mathrm{r_{po}}, \mathrm{h}, 0)$ is the bending energy in a fully toroidal state, given by eq. 4.3. The change in total membrane area due to pore formation in these partially toroidal states is given by

$$\Delta A_{\text{po}}(r_{\text{po}}, R_{\text{po}}, \phi) = \pi H\big((R + H)(2\pi - \phi) - 2H(1 + \cos\phi)\big) + \pi(R + H)^2 - \pi\left(\frac{D}{2}\right)^2 \tag{4.14}$$

In the partially toroidal states, h does not correspond to the membrane separation at the edge of the pore, although $\mathrm{r_{po}}$ is still the pore radius. Thus, we indicate the membrane separation at the NLP boundary by $\mathrm{h_{po}}$ given by

$$\mathrm{h_{po}} = \begin{cases} \frac{\mathrm{h}}{2}(1 + \cos \phi), \mathrm{r_{po}} + \frac{\mathrm{h}}{2} + \delta \geq \frac{\mathrm{D}}{2} \\ \mathrm{h}, \mathrm{r_{po}} + \frac{\mathrm{h}}{2} + \delta < \frac{\mathrm{D}}{2} \end{cases} \tag{4.15}$$

Figures

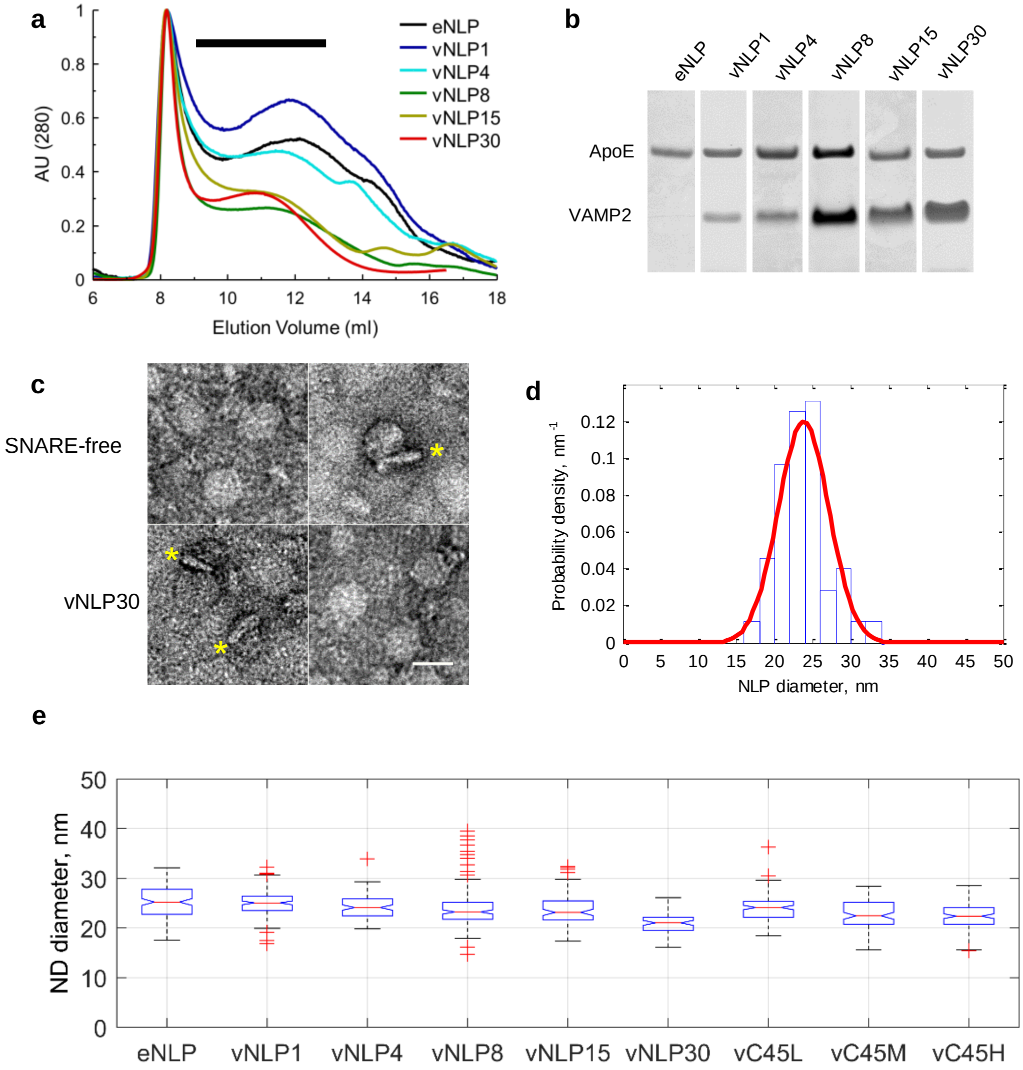

Figure 4.1. Size separation and characterization of NLPs.

a. Representative size exclusion chromatograms of various NLP preparations as indicated. NLPs were detected by absorption at 280 nm. Typically, a fraction comprising 9-13 ml was collected (black horizontal bar). **b**. Coomassie stained SDS PAGE of NLPs. For each preparation, the amount of VAMP2 relative to ApoE was determined using densitometry. **c**. Representative negative-stain EM micrographs of NLPs. Top row are SNARE-free NLPs. Bottom row are NLPs loaded with 30 v-SNARE copies. NLPs marked with * are oriented perpendicular to the imaging plane and show the flat disc structure. Scale bar is 25 nm. **d**. Distribution of NLP diameters for a representative vNLP15 sample, determined from analysis of micrographs as in c. A normal distribution fit (red line) is shown. **e**. Boxplot of representative NLP sizes for various conditions. NLPs containing lipid-anchored VAMP2 (vC45L, vC45M, vC45H for low, medium, and high copy number of C45 lipid-anchored VAMP2, bearing ~1, 4, and 15 copies) had sizes comparable to NLPs bearing similar loads of wild-type VAMP2 (vNLP1, vNLP4, and vNLP15). Activity of these NLPs was tested in an established bulk fusion assay with t-SNARE reconstituted liposomes (Fig. 4.1—Figure supplement 1).

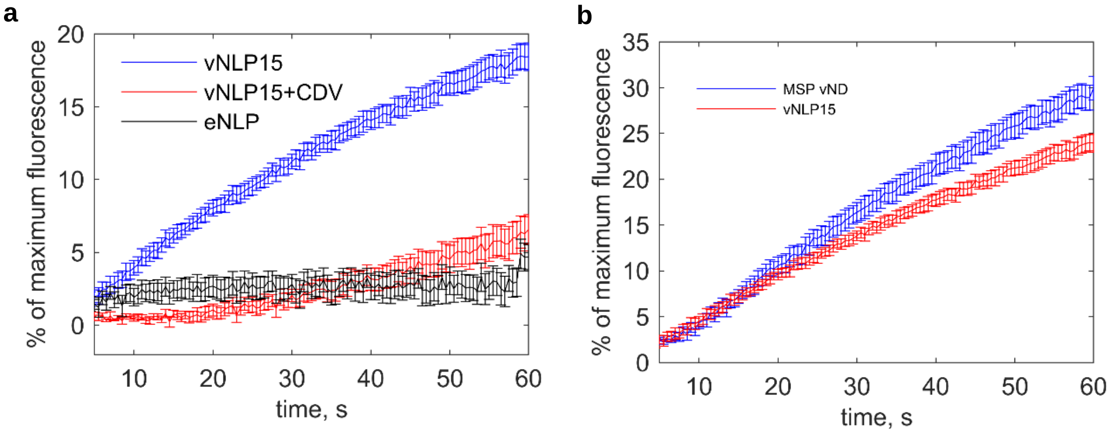

Figure 4.1—Figure supplement 1. Bulk content release assay (Shi *et al.*, 2012; Bello *et al.*, 2016) shows fusion of vNLPs with t-SNARE reconstituted small unilamellar vesicles (t-SUVs) is SNARE-dependent.

a. Release of calcium from the liposome lumens as a function of time. t-SNARE liposomes initially entrapping calcium were mixed with vNDs. Fusion with vNDs leads to leakage of calcium through fusion pores. Binding of leaked calcium to the calcium-sensitive dye Mag-fluo-4, included in the fusion buffer, results in increased fluorescence. The maximum fluorescence was determined by adding detergent to release all entrapped calcium at the end of the reaction. Results are displayed as percentage of maximum fluorescence as a function of time. Nine independent measurements per condition were averaged. **b**. Bulk calcium release rates are comparable for MSP or NLP discs bearing ~8 and ~15 copies of VAMP2, respectively, even though fusion pores can in principle grow to much larger sizes for NLPs. Thus, either the bulk contents release assay is insensitive to pore properties under these conditions, or pores with similar properties occur in both cases. Single-pore measurements indicate about 10% of vNLP15 pores reach large sizes. Eleven and 8 independent measurements were averaged for MSP vND and vNLP15 conditions, respectively. The error bars represent standard error of the mean for both panels a and b.

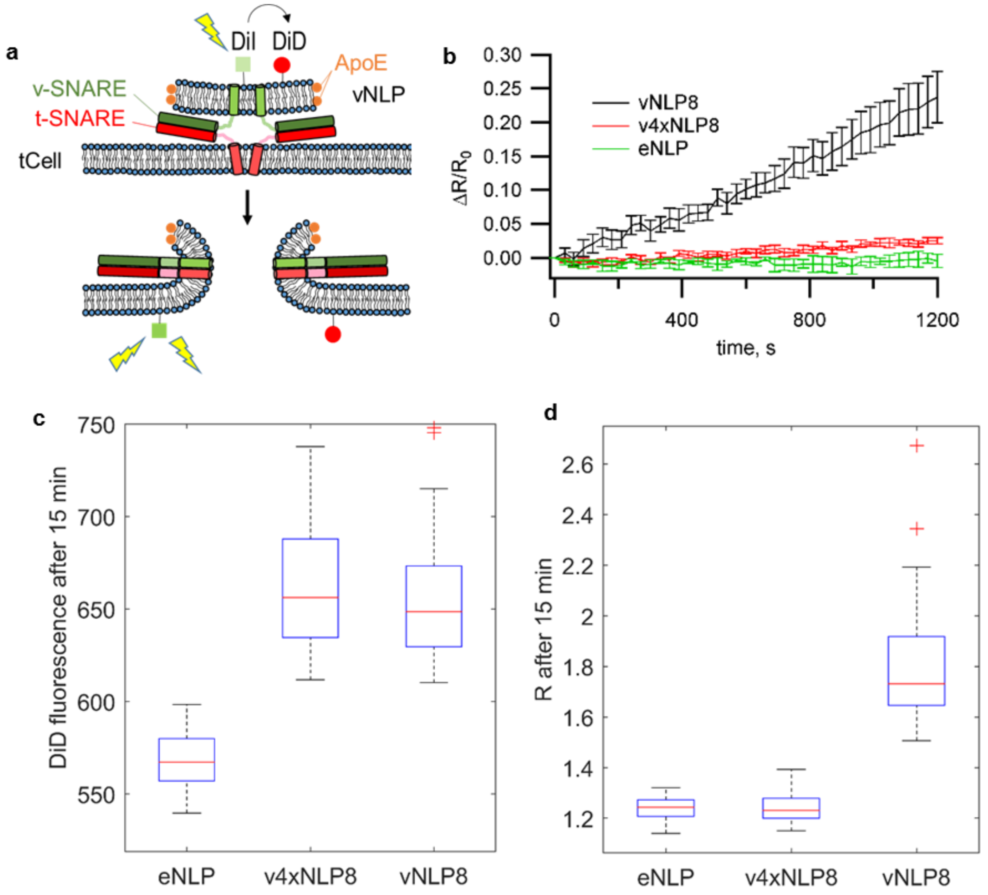

Figure 4.2. vNLPs induce lipid mixing when incubated with flipped t-SNARE cells (tCells). **a**. Schematic of the assay. **b**. NLPs co-labeled with 1 mole % DiI and DiD were incubated with tCells for 30 min at 4°C, a temperature that allows docking, but not fusion. Cells were then rinsed with cold PBS to remove free NLPs, and PBS pre-warmed to 37°C was added. Imaging of DiI and DiD fluoresce started shortly after the dish was mounted onto a confocal microscope stage held at 37°C. For each imaging cycle, we sequentially acquired DiI and DiD fluorescence (λ_{ex} =561 nm and 647 nm for DiI and DiD, respectively). We quantified cell membrane DiI and DiD fluorescence and calculated the ratio of these two intensities, R. DiI fluorescence reports lipid mixing, while the DiD fluorescence is proportional to the amount of docked NLPs per cell. Thus, the ratio R normalizes the lipid mixing signal to the amount of docked NLPs. Averages of 69, 73, and 47 regions of interest (+/- S.E.M.) from 7, 7, and 3 dishes are shown for NLPs loaded with ~8 copies of VAMP2 (vNLP8), ~8 VAMP2-4x mutant that is docking-competent but fusion incompetent (v4xNLP8), and empty NLPs (eNLPs), respectively. **c,d**. Confocal imaging after 15 min incubation and washing of NLPs with tCells at 37°C. **c**. DiD fluorescence reflects the amount of docked NLPs per cell. NLPs reconstituted with ~8 copies of VAMP2-4X (v4xNLP8) docked with the same efficiency as wild-type VAMP2 NLPs bearing the same SNARE copy number (vNLP8). **d**. DiI/DiD fluorescence ratio (R) reports lipid mixing normalized to the amount of docked NLPs per cell. Despite efficient docking, v4xNLP8 did not induce any lipid mixing. eNLP, empty (SNARE-free) NLPs. For c and d, 6, 10, and 11 dishes were measured and 41, 66, and 63 regions of interest analysed for eNLP, v4xNLP8, and vNLP8, respectively.

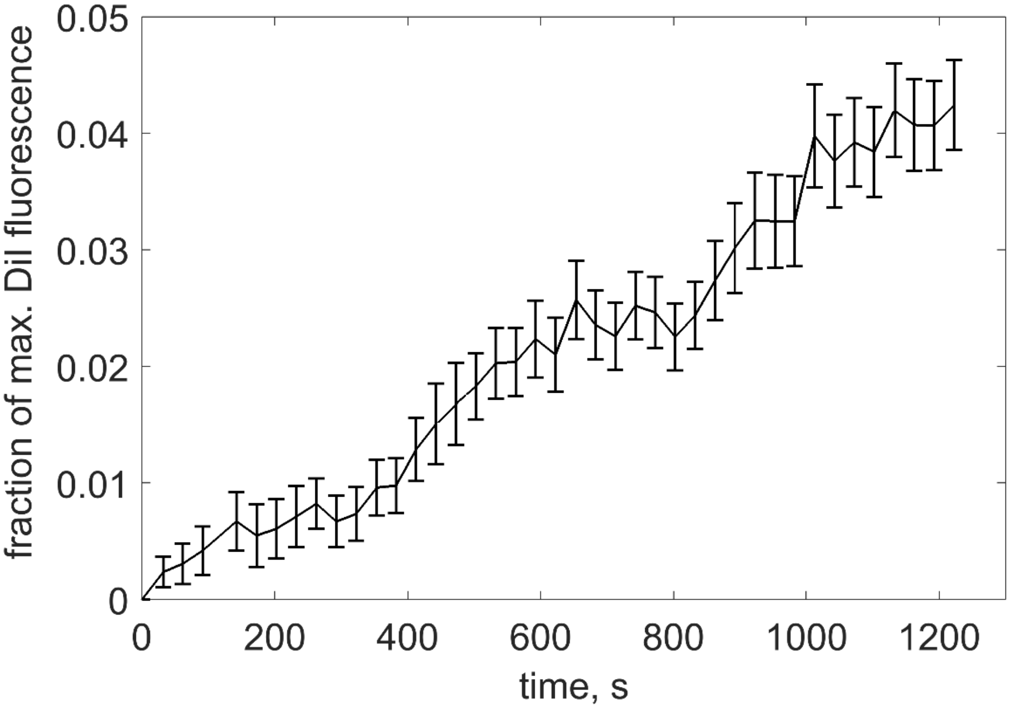

Figure 4.2—Figure supplement 1. Estimation of the extent of lipid mixing.
As in Fig. 4.2b, vNLPs co-labeled with 1 mole % each of DiI and DiD were incubated with tCells for 30 min at 4°C, a temperature that allows docking, but not fusion. Cells were then rinsed with cold PBS to remove free NLPs, and PBS pre-warmed to 37°C was added. Imaging of DiI and DiD fluoresce started shortly after the dish was mounted onto a confocal microscope stage held at 37°C. At the end of the experiment, the DiD (acceptor) fluorescence was completely bleached using direct excitation at 647 nm with 100% laser power to obtain the maximum possible donor (DiI) intensity, F_{max}. We then rescaled the donor fluorescence values $F(t)$ to obtain the fraction of maximum DiI fluorescence: $\widetilde{F(t)} = (F - F_0)/(F_{max} - F_0)$, where F_0 is the minimum at the beginning of acquision.

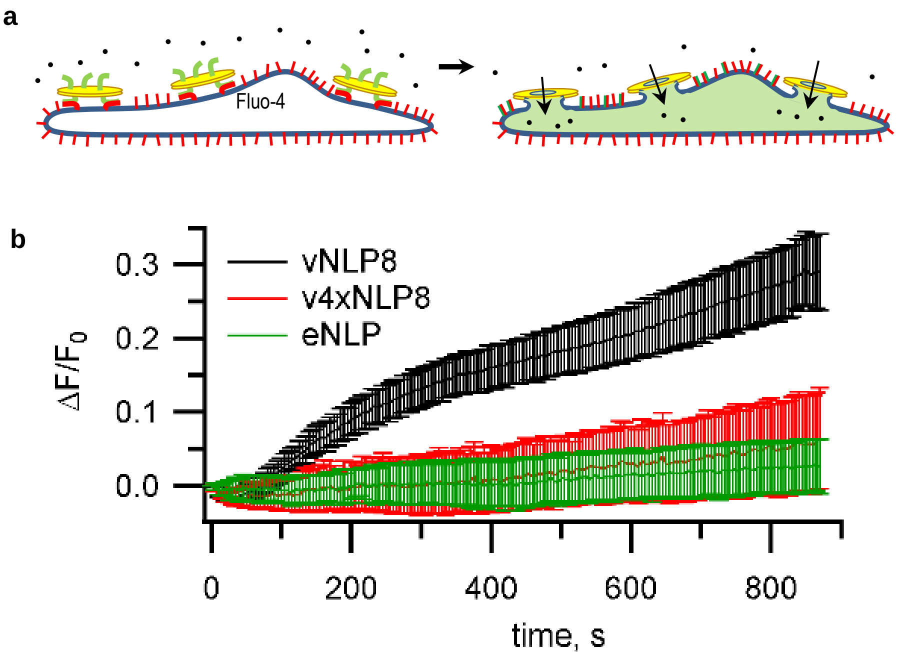

Figure 4.3. Calcium influx assay.

a. Schematic of the assay. **b**. tCells were loaded with the Ca^{2+} indicator Fluo-4 whose fluorescence was imaged as a function of time. Opening of fusion pores allowed Ca^{2+} influx into the cytosol, causing the Fluo-4 signal to increase for vNLP8 (10 dishes), but not for v4xNLP (6 dishes) or eNLP (4 dishes) samples. The fluorescence from the entire viewfield for each dish was averaged. Displayed errors are S.E.M.

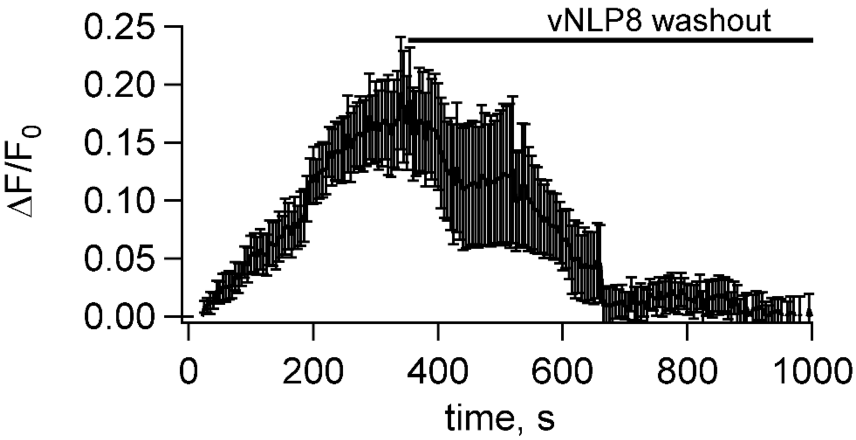

Figure 4.3—Figure supplement 1. Fusion pores connecting NLPs to cells eventually close. Flipped t-SNARE cells were loaded with the Ca^{2+} indicator Fluo-4 whose fluorescence was imaged as a function of time after addition of NLPs bearing 8 copies of VAMP2, as in Fig. 4.3. Opening of fusion pores allowed Ca^{2+} influx into the cytosol, causing the Fluo-4 signal to increase. To test whether pores eventually closed, free NLPs were washed out after 5 min, as indicated. This caused the Fluo-4 signal to return to baseline within a few minutes, indicating pores eventually closed. Data from 6 dishes, errorbars are S.E.M.

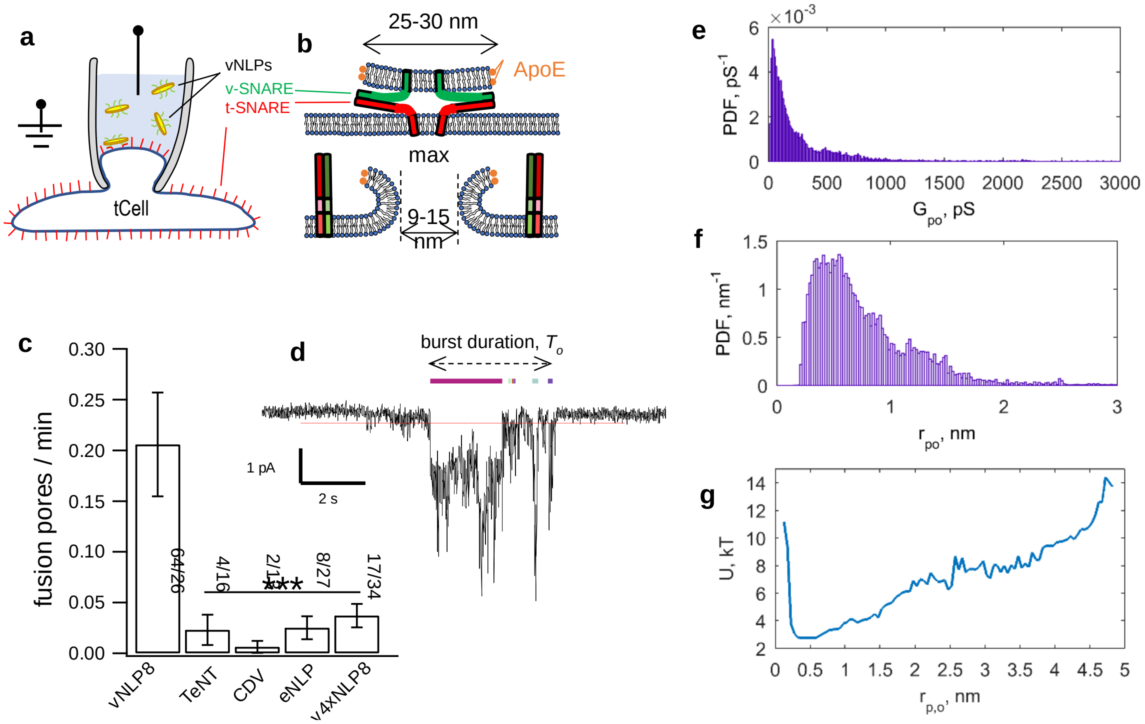

Figure 4.4. Detection of single-pores between vNLP nanodiscs and tCells.

a, b. Schematic of the assay. A glass pipette seals a patch on the tCell membrane. The pipette solution includes NLPs. When a vNLP fuses with the tCell membrane (b), a nm-sized pore opens and connects the cytosol to the pipette solution. Thus, currents through voltage clamped pores report fusion and pore properties with sub-ms time resolution. In b, the bilayers, SNAREs and the NLP are drawn approximately to scale. The light, medium and dark shades of green and red indicate the transmembrane, linker, and SNARE domains of the v- and t-SNAREs, respectively. **c**. Pores are SNARE-induced. When empty NLPs (eNLPs), cytoplasmic domain of VAMP2 (CDV), tetanus neurotoxin light chain (TeNT), or NLPs loaded with the docking-competent, fusion-incompetent VAMP2-4X mutant (v4xNLP8) were used, only a very low level of current activity was recorded compared to NLPs loaded with ~8 copies of wild-type v-SNAREs. The number of pores/patches are indicated for each condition. (*** indicates p<0.001, t-test against vNLP8) **d**. An example of a fusion pore current "burst". Fusion leads to fluctuating and flickering currents that are well separated in time from one another. A threshold (red dotted line) and a minimum crossing time is imposed to define pore open periods (Materials and Methods and Wu et al. (Wu *et al.*, 2016)). Detected sub-openings are indicated with colored bars above the current trace. **e.** Average probability density function (PDF) of open-pore conductances. **f**. Averaged PDF of open-pore radii. Data are from 61 fusion pores, 26 cells. **g**. Free energy profile calculated from the distribution of pore sizes in f. Distributions of flicker numbers per pore and burst lifetimes are shown in Fig. 4.4—Figure supplement 1. Additional examples of current bursts are provided in Fig. 4.4—Figure supplement 2.

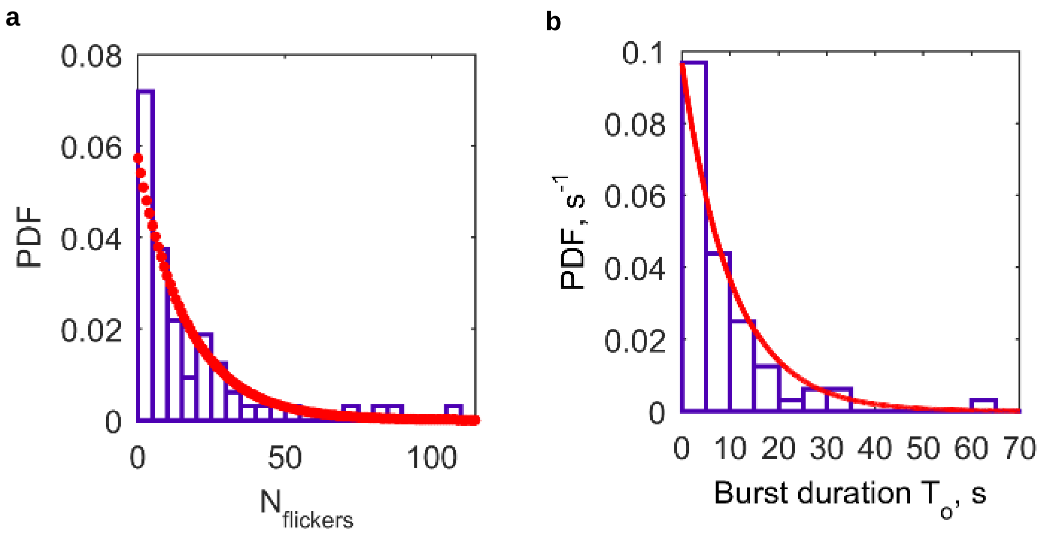

Figure 4.4—Figure supplement 1. Additional properties of single fusion pores connecting NLPs loaded with 8 copies of VAMP2 and flipped t-SNARE cells (64 pores from 26 cells).

a. Distribution of flicker numbers, and fitted geometric distribution. The red dots are a fit to a geometric distribution, $y = p(1-p)^n, n = 0,1,2$, 3,... with $p = 0.0573$ (95% confidence interval: $0.0437, 0.0709$). Mean ± SEM was 16±2.7 flickers. **b**. Distribution of burst lifetimes, T_0, as defined in d, and exponential best fit (red curve). Mean ± SEM=10.3±2.2 s.

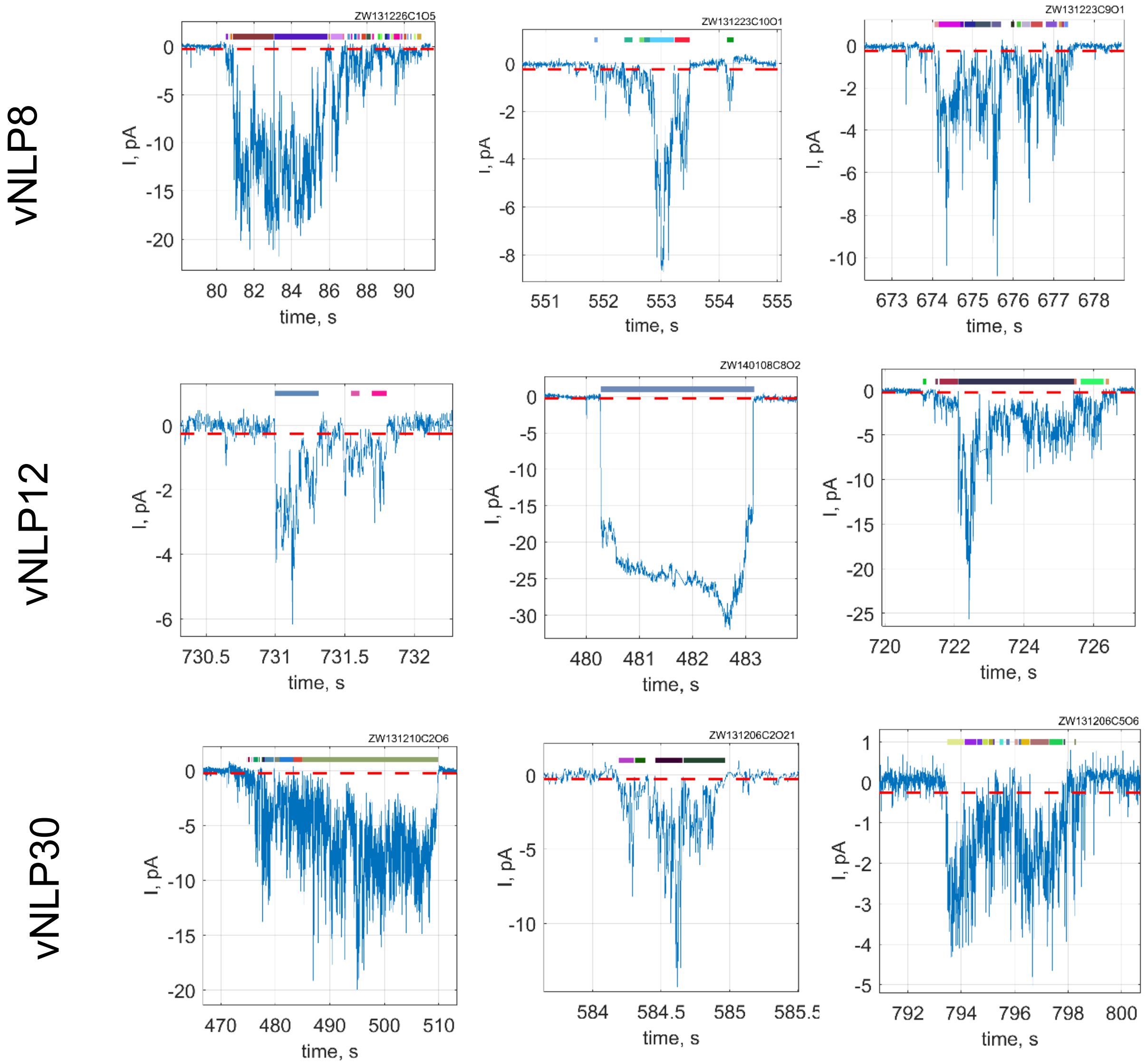

Figure 4.4—Figure supplement 2. Additional examples of current bursts.

Red dashed line indicates -0.25 pA threshold. During a burst, a pore is considered open if it crosses this threshold for at least 15 consecutive points (60 ms). Detected open sub-periods are indicated by colored bars above the traces.

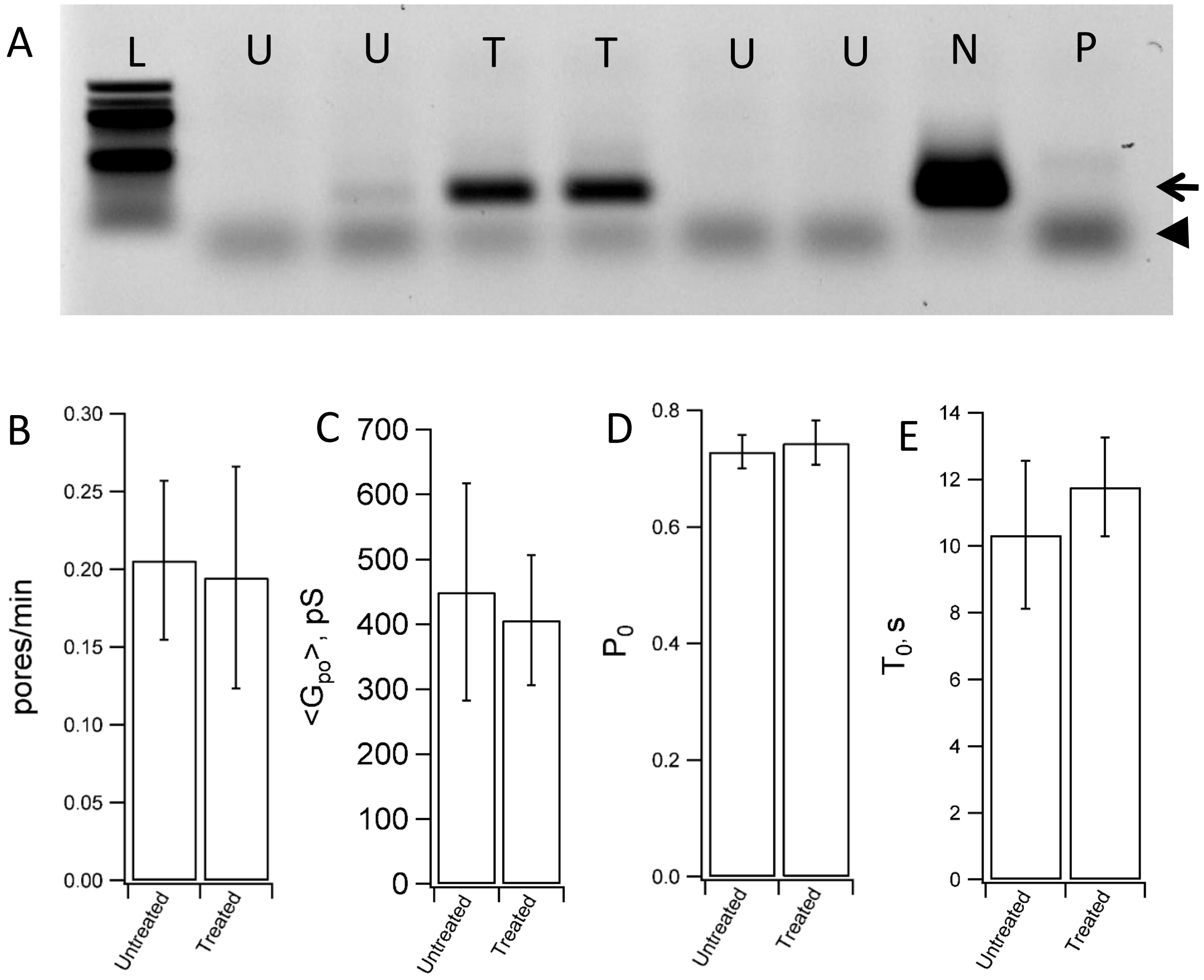

Figure 4.4—Figure supplement 3. Mycoplasma contamination does not affect fusion with NLPs. **A**. Testing of flipped t-SNARE cells for mycoplasma contamination. Mycoplasma-negative control (lane marked N) shows the internal control band at 479 bp (arrow). The positive control (lane marked P) shows a band at 270 bp (arrowhead) and an additional band of the internal control at 479 bp. The 479 bp internal control DNA of the detection kit fades with increased amount of amplicons formed due to mycoplasma DNA. Lane L is the ladder, lanes marked U test untreated flipped t-SNARE cells, lanes marked T test flipped t-SNARE cells treated with an anti-mycoplasma agent. Anti-mycoplasma treatement reduced contamination substantially. **B-E**. Fusion between NLPs bearing 8 total copies of v-SNARE (vNLP8) and flipped t-SNARE cells that were either untreated or treated for mycoplasma contamination. The rate at which pores appear (B), the mean pore conductance (C), the pore open probability during a burst (D) and the pore lifetime (E) are indistinguishable for untreated vs. mycoplasma-treated cells. 64 pores from 26 patches were recorded from untreated cells and 51 pores from 21 patches were recorded from treated cells.

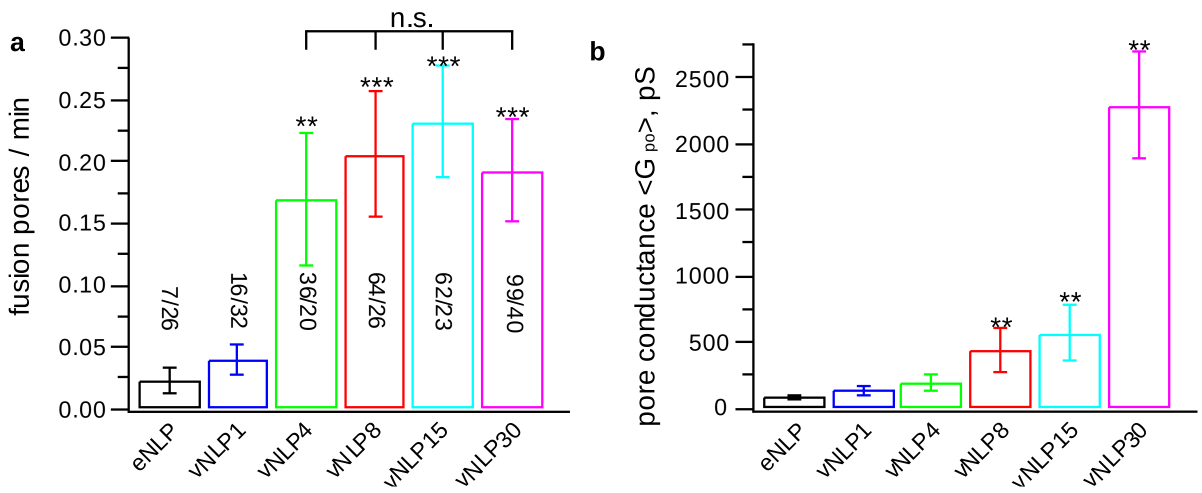

Figure 4.5. Only a few SNARE complexes are required to nucleate a pore, but more than ~15 are required to dilate it.

a. Pore nucleation rate as a function of total v-SNARE copy number per NLP. Copy numbers per NLP face are approximately 0, 1, 2, 4, 7.5, and 15 for eNLP and vNLP1 through vNLP30, respectively. Pore nucleation requires ~2 copies per NLP face and saturates above ~4 copies per NLP face. n.s. indicates no statistically significant differences for the mean fusion rates among vNLP4, vNLP8, vNLP15, and vNLP30 samples, as assessed by an analysis of variance (ANOVA) and multiple pairwise comparisons of the group means. The source and analysis files are provided as Fig. 4.5—source data 1. b. Mean single-pore conductance, $\langle G_{po} \rangle$ as a function of v-SNARE copies loaded into NLPs. $\langle G_{po} \rangle$ increases rapidly as increasing numbers of v-SNAREs are loaded per NLP. At the maximum value tested, ~15 copies per NLP face, $\langle G_{po} \rangle$ is far from saturating. The number of pores analyzed/total number of cells is indicated for each condition in a. **, *** indicate p<0.01 and 0.001, respectively, using the two-sample t-test (a) or the Kolmogorov-Smirnov test (b) against eNLP. Additional pore properties are shown in Fig. 4.5—Figure supplement 1. Properties of pores induced using lipid-anchored v-SNAREs are shown in Fig. 4.5—Figure supplement 2.

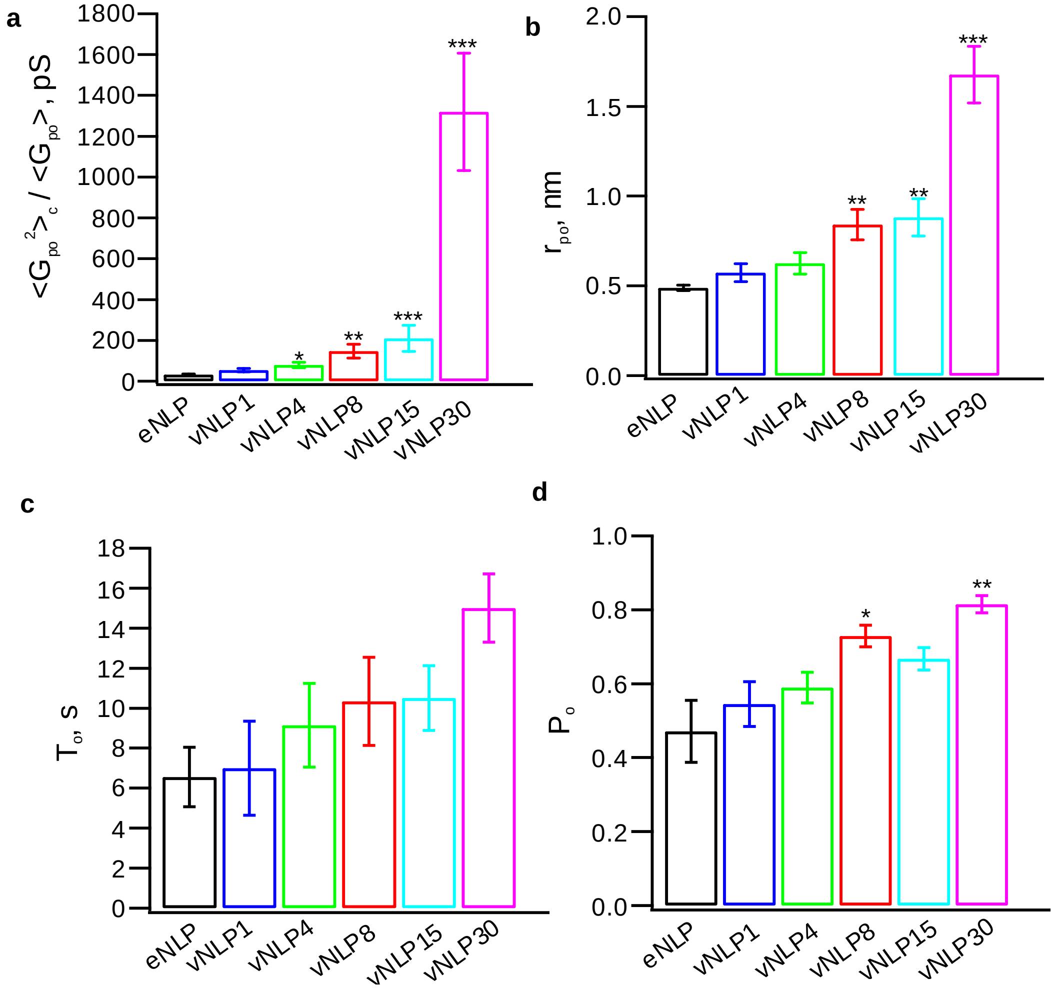

Figure 4.5—Figure supplement 1. Additional pore properties as a function of v-SNARE copy number per NLP.

a. Conductance fluctuations relative to mean $\langle G_{po}^2 \rangle / \langle G_{po} \rangle$. b. Mean open-pore radii $\langle r_{po} \rangle$. c. Pore lifetime, T_o. d. Burst open probability P_o. eNLP, empty (SNARE-free) NLPs. The numbers in vNLP1 through vNLP30 indicate the total v-SNARE copy numbers per NLP. *, **, *** indicate p<0.05, 0.01, and 0.001, respectively, using the Kolmogorov-Smirnov test against eNLP.

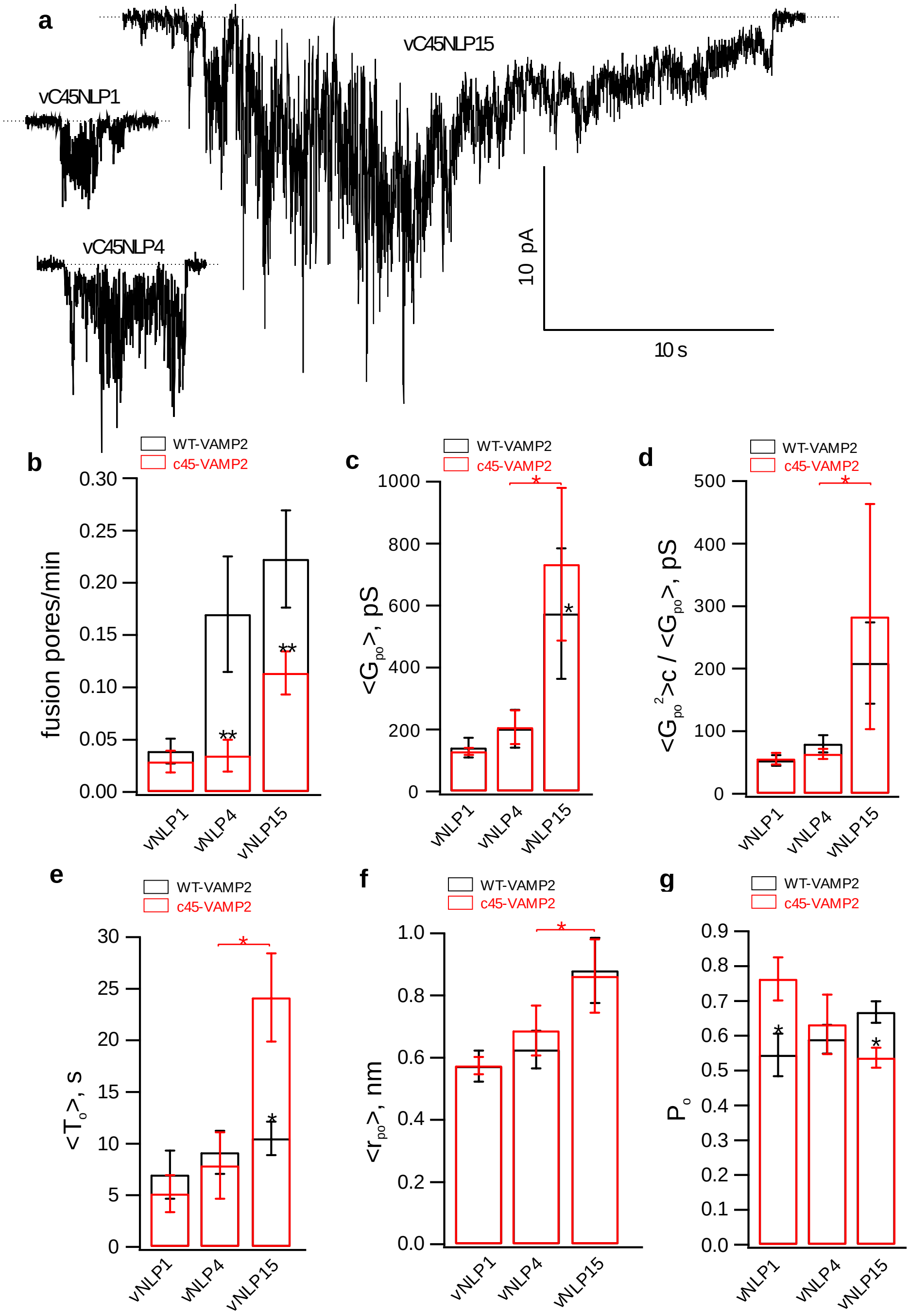

Figure 4.5—Figure supplement 2. Larger numbers of lipid-anchored v-SNAREs promote pore dilation.

a. Sample traces for NLPs loaded with different copy numbers of lipid-anchored VAMP2. **b-g**. Fusion pore properties of lipid-anchored (red) and wild-type (black) v-SNARE NLPs (see legend of Fig. 4.5—Figure supplement 1 for parameter definitions). Replacing VAMP TMD with a C45 lipid anchor reduced pore nucleation (b) but made them last longer (e), consistent with previous results using smaller MSP NDs **(Wu *et al.*, 2016)**. Overall trends as a function of copy number were similar for all parameters for C45 and WT vNLPs. The number of pores/patches were 90/63, 12/30, and 11/29 for vC45NLP15, vC45NLP4, and vC45NLP1, respectively.

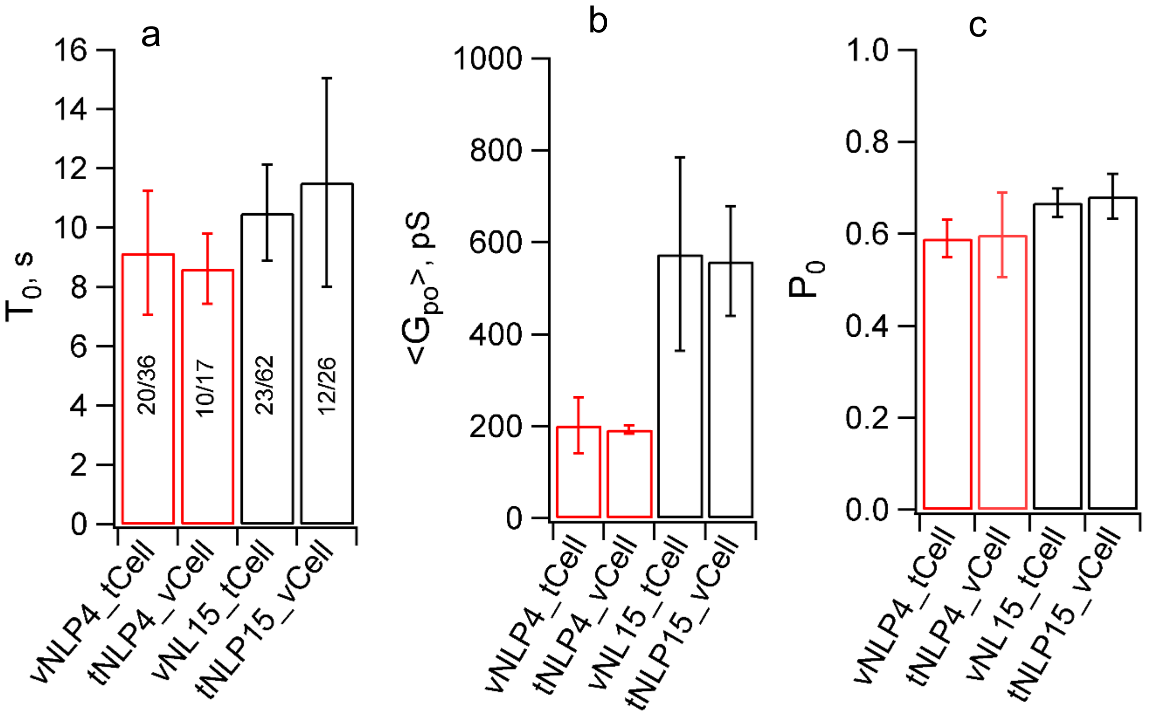

Figure 4.5—Figure supplement 3. Swapping the locations of the v- and t-SNAREs does not affect pore properties.

Flipped v-SNARE cells were fused with t-SNARE NLPs (loaded with 4 or 15 total copies of t-SNAREs, tNLP4 and tNLP15), inverting the target membrane. For a given SNARE copy number in NLPs, burst lifetime (a), mean open-pore conductance (b), and pore open probability during a burst were indistinguishable between the vNLP_tCell and tNLP_vCell configurations. The number of pathches/pores are indicated for each condition in (a). The same numbers apply to (b) and (c). For vNLP_tCell fusion, results are copied from Fig. 4.5 and Fig. 4.5—Figure supplement 1 to facilitate comparison.

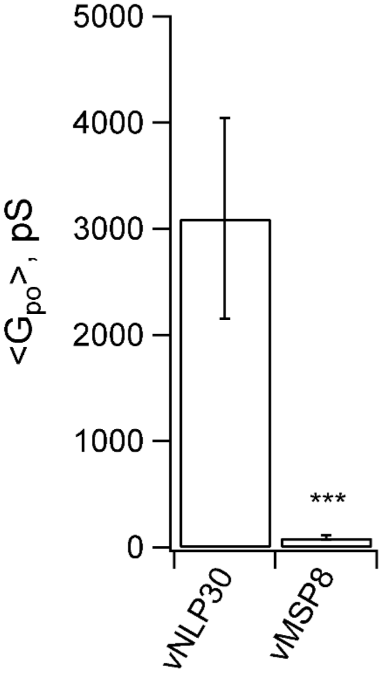

Figure 4.5—Figure supplement 4. Permeability of pores to NMDG$^+$.

Sodium in the pipette solution was replaced with N-methyl-D-glucamine (NMDG$^+$), a large ion ~1.1 × 0.5 nm in size without its hydration shell(Melikov *et al.*, 2001), to test its passage through the fusion pores. Conductance was low when ~15 nm MSP nanodiscs with 8 copies of v-SNAREs (vMSP8) were used(Wu *et al.*, 2016), but not affected when ~23 nm NLPs bearing 30 v-SNAREs were employed (vNLP30). This suggests the increase in mean pore conductance as SNARE copy numbers are increased (Fig. 4.5b) is due to pores becoming larger, not the appearance of multiple small pores. *** indicates $p<0.001$ (two-sample Kolmogorov-Smirnov test).

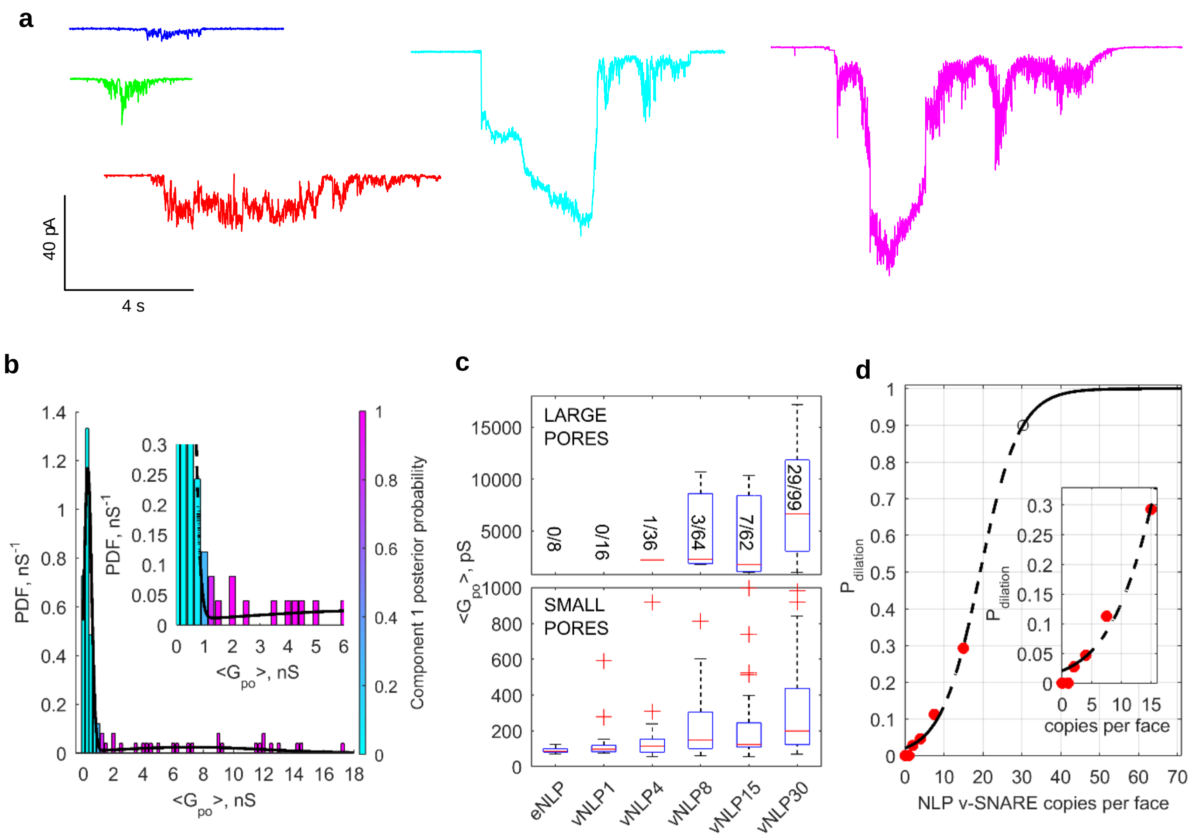

Figure 4.6. Increasing v-SNARE copy numbers increases the occurrence of large pores.
a. At low copy numbers, all pores produced small amplitude currents (leftmost traces). As copy numbers increased, most pores still produced small-amplitude currents, but an increasing fraction had much larger currents, such as the two traces shown on the right. **b**. The probability density function of mean open-pore conductance values $\langle G_{po} \rangle$ from 99 vNLP30-tCell fusion pores was fitted with a Gaussian mixture model with two components. The data clustered into two Gaussians centered around 300 pS and 7.21 nS, separated at ~1 nS. For every bin, the probability of belonging to component 1 is color-coded with the color map indicated to the right of the plot. Inset shows a zoom to the transition region between the two components. **c**. Individual pores were classified as low ($\langle G_{po} \rangle < 1$ nS) or high ($\langle G_{po} \rangle > 1$ nS) conductance. The distribution of mean conductances are shown as box plots for the v-SNARE copy numbers tested. The number of large pores/total number of pores is indicated for each group. **d**. Probability of pore dilation, $P_{dilation}$, defined as the fraction of pores in the high-conductance category in c as a function of SNARE copy number per NLP face (red dots). The dashed line is a fit $P_{dil} = \exp\left(\frac{N_{SNARE}-N_o}{b}\right) / \left(1 + \exp\left(\frac{N_{SNARE}-N_o}{b}\right)\right)$, where N_o is the copy number at which $P_{dil} = 0.5$, and b measures the width of the transition. Best fit parameters were (with 95% confidence intervals) $N_o = 19.3\ (16.9, 21.7)$, and $b = 5.0\ \ (3.3,\ 6.7)$ (R^2: 0.97). The black open circle indicates that $P_{dil} = 0.9$ requires 30 SNAREs. See Fig. 4.6—Figure supplement 1 for a plot of open-pore conductance fluctuations relative to mean as a function of mean open-pore conductance.

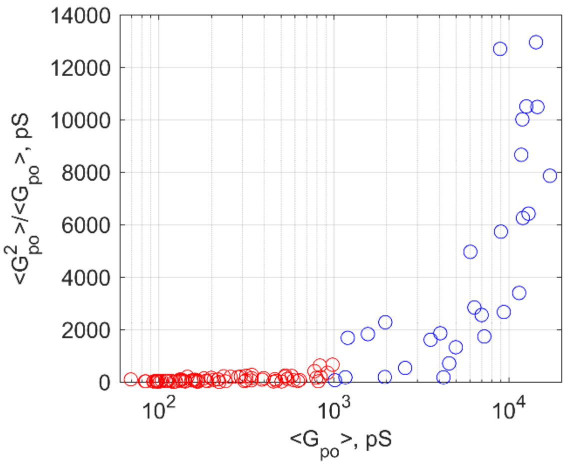

Figure 4.6—Figure supplement 1. Open-pore conductance fluctuations relative to mean, $\langle G_{po}^2 \rangle / \langle G_{po} \rangle$, as a function of mean open-pore conductance, $\langle G_{po} \rangle$.

Fluctuations rise sharply for $\langle G_{po} \rangle \gtrsim 1$ nS (blue circles).

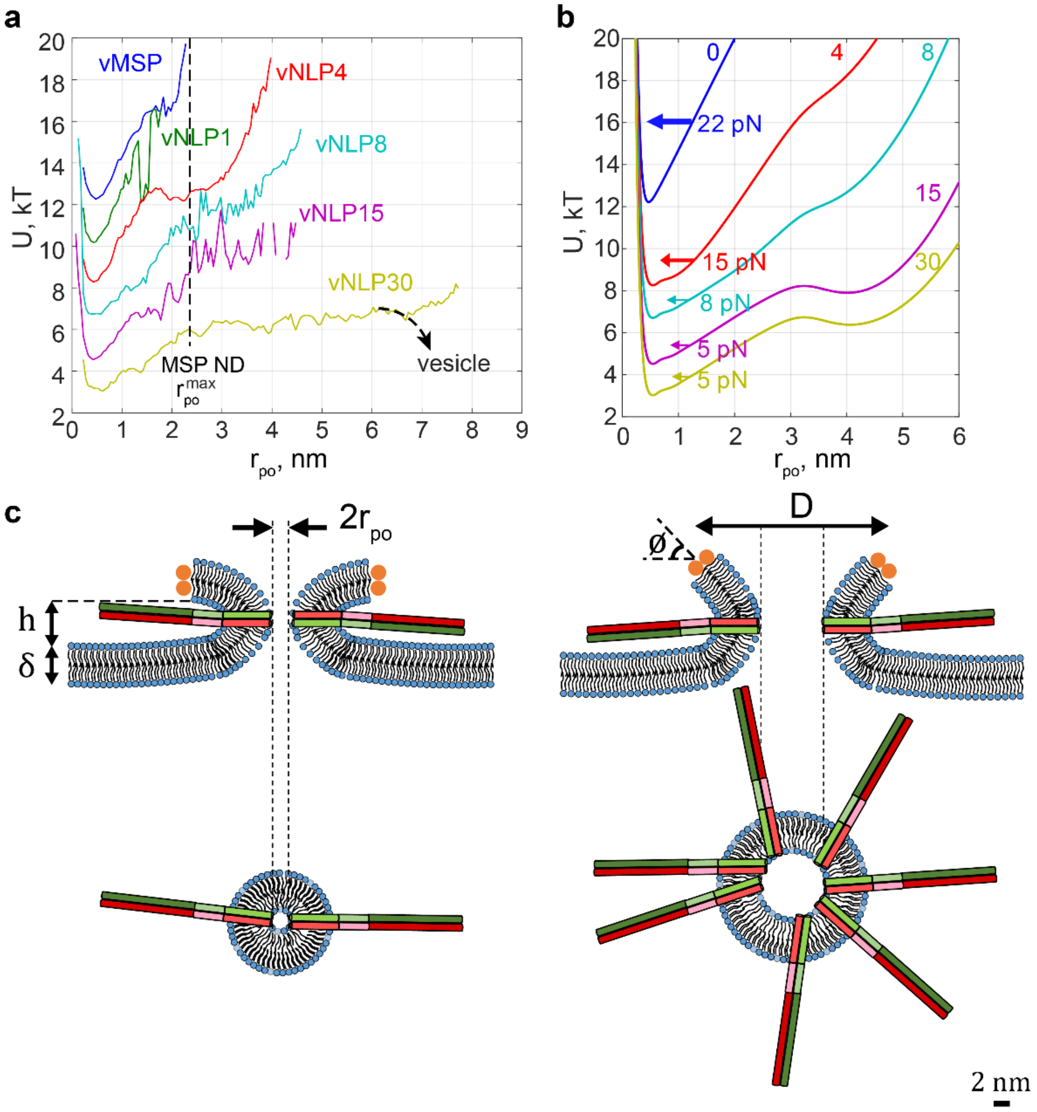

Figure 4.7. Free energy profiles for pore dilation, experimental results and model predictions. The mathematical model describes a mechanism of pore expansion in which SNARE crowding generates entropic expansion forces.

a. Open-pore free energy landscape $U(r_{po})$ for different SNARE copy numbers. Increasing SNARE copy numbers in NLP discs softens the energy barrier against pore expansion. For vNLP30 discs, the profile starts rising above $r_{po} \approx 7$ nm (expected maximum size $r_{po,\,max}^{NLP} \approx 7-8$ nm). If a vesicle were fusing instead of a NLP, dilation would presumably relax pore curvature and lower the energy (dashed curve marked “vesicle”). vMSP data was obtained in earlier work(Wu *et al.*, 2016) using smaller, ~16 nm diameter nanodiscs stabilized by the membrane scaffold protein (MSP), with 7-9 v-SNARE copies. The maximum allowable pore size is limited to slightly above 2 nm radius for MSP discs. The same energy minimum around $r_{po} \approx 0.5$ nm is found regardless of copy numbers or the size of disc used, suggesting this minimum represents an inherent property of fusing bilayers. **b.** Corresponding free energy profiles predicted by a mathematical model of the fusion pore with SNAREs (Materials and Methods and Fig. 4.7—Figure supplements 1 and 2). Each curve shows the copy number and the net inward force (averaged over all sizes $r_{po} > 1.5$ nm) tending to close down the pore to the minimum energy value. Membrane bending and tension resist pore expansion with a total force ~ 22 pN (SNARE-free pore, blue). With SNAREs, crowding effects produce an expansive entropic force that reduces the net inward force.

The net force is progressively lowered with increasing numbers of SNAREs, reaching ~ 5 pN with 15 SNAREs. **c.** Schematic illustrating proposed SNARE-mediated pore expansion mechanism. Left: a few SNAREs can nucleate a pore, but dilation beyond a few nm is unlikely. Right: with many SNAREs, crowding generates expansion forces sufficient to offset the intrinsic bilayer resistance and expand the pore. h, δ, D and ϕ are the height of the pore, the thickness of the membrane, the mean diameter of the vNLP discs, and the angle of twisting of the ApoE proteins respectively. For definitions of other model parameters, see Materials and Methods.

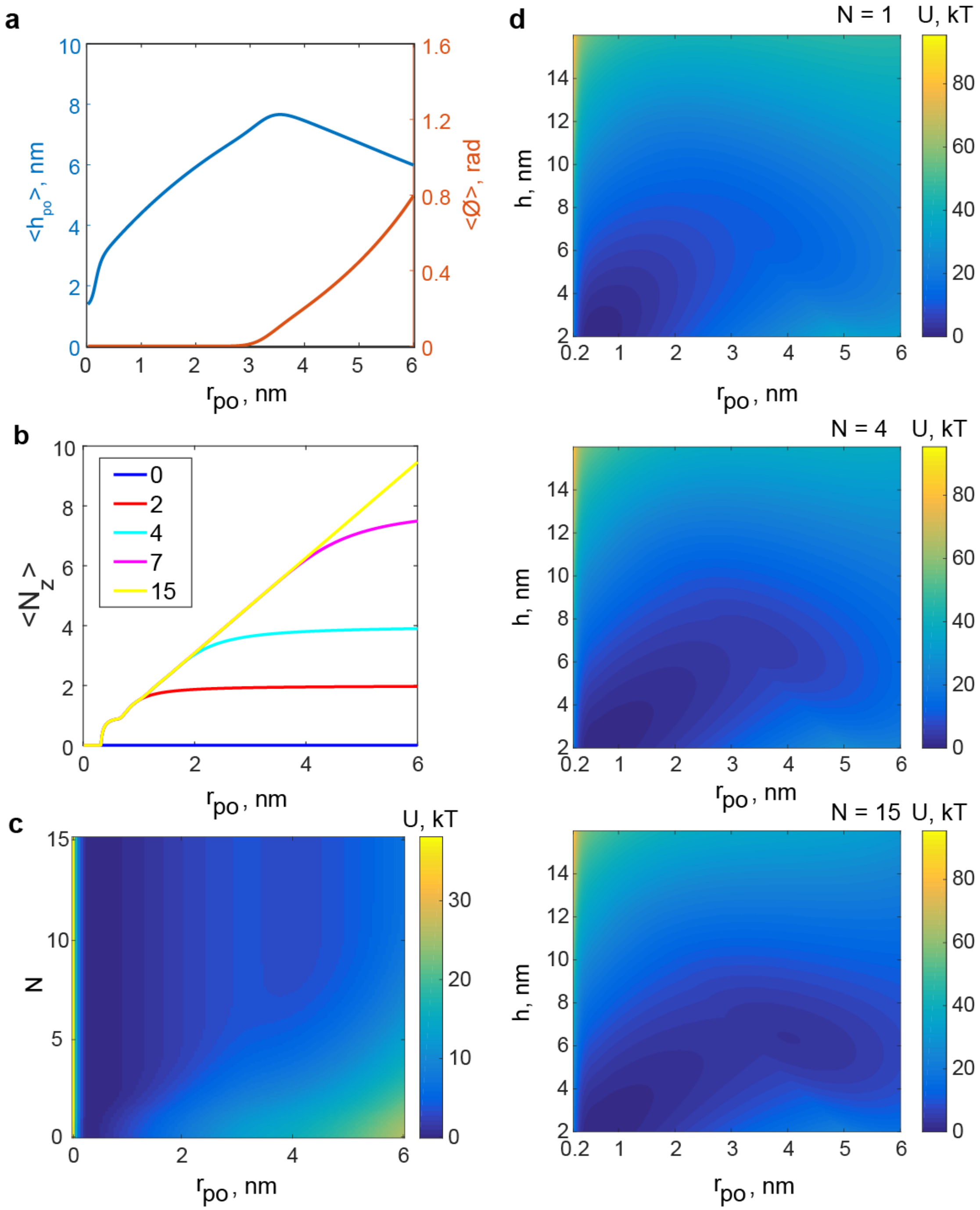

Figure 4.7—Figure supplement 1. Results of the mathematical model of the fusion pore in the presence of SNAREpins.

a. Membrane separation and angle of twist of the ApoE proteins versus pore size for a fusion pore without SNAREs. **b.** Mean number of zippered SNAREs versus pore size for a fusion pore with $\mathrm{N} = 0,2,4,7,15$ total numbers of v-SNAREs per NLP face. **c.** Free energy as a function of pore size and number of SNAREs (treated as a continuous variable). **d.** Free energy as a function of pore size and membrane separation for fusion pores with $\mathrm{N} = 1, 4, 15$ total available v-SNAREs.

Chapter 5: Conclusion

In the work presented here, we have tried to understand the roles that subcellular forces play in the function of the cytokinetic ring and the fusion machinery. Using a combination of mathematical modeling and experiment, we have demonstrated that (i) ring tension regulates septum closure via mechanosensitive septum growth machinery, (ii) a node-based architecture with node turnover is sufficient to marshal actomyosin forces to produce experimental values of ring tension and help the stability of the ring, (iii) SNARE proteins produce a cooperative entropic force that lessens the barrier to pore dilation and presumably successful neurotransmitter release.

Ring tension regulates septum growth

Although the cytokinetic ring machinery has been widely studied in fission yeast, the cell wall growth machinery is not so well characterized, and the interaction between the ring and the cell wall is poorly understood. The conventional purse-string mechanism suggests that the ring provides the mechanical force to deform the membrane and physically cleave the cell into two (Wolf *et al.*, 1999). However, in fission yeast this is not the case. Recent experiments have measured the ring tension and the modulus of the cell wall. The latter is so large that the force per unit area produced by the ring cannot possibly deform the cell wall and cause it to ingress in the wake of the constricting ring. Hence, the roles of the ring here are poorly understood.

We noticed that the septum holes in most previously obtained images were circular. As it is a considerable technical challenge to coordinate growth across a ~10 µm perimeter produced by ~2500 inherently-stochastic β-glucan synthase complexes, we hypothesized that septum growth was regulated. As the ring is attached to the plasma membrane where the cell-wall growing glucan synthases reside, we hypothesized that this regulation happened via the force exerted by the ring on these proteins.

Using a combination of mathematical modeling, image analysis, and experiment, we discovered that the edge roughness of the septum hole contour was regulated, and grew with the length scale under consideration with a one-half power law. This is similar to the Edwards Wilkinson and KPZ models of interfacial growth that have length-scale-dependent roughness that grows with the length scale according to a one-half power law (Edwards and Wilkinson, 1982; Kardar *et al.*, 1986). Our mathematical model reproduced this as well, and revealed that the effect of ring tension is to correct septum growth in a curvature-dependent manner to ensure the circularity of the septum hole. Thus, we have uncovered a key role of ring tension in ensuring successful cell division.

Node-based architecture marshalls forces to generate ring tension

Recent super-resolution experiments have revealed the ultrastructure of the constricting cytokinetic ring in fission yeast (Laplante *et al.*, 2016). Membrane-anchored protein complexes called nodes contain myosin-II molecules that pull on actin filaments synthesized by the formin Cdc12. Thus, the fundamental force-producing interaction in the ring is myosin-II of one node pulling on a filament growing from another node. These interactions somehow add up to a tense ring. Also, one would expect a ring with such interactions to be unstable as nodes are ‘attractive’ and are prone to clumping. Hence, naturally occuring density fluctuations would give rise to runaway contraction and hence rupture. How does the ring maintain its stability?

To answer these questions, we developed a simple, coarse-grained, one-dimensional model of the ring, representing nodes as a continuous density field. Given that previous measurements show a mean of one formin per node, there is only one actin filament per node, that could point clockwise or counterclockwise along the length of the ring. Depending on the polarity of this node attached filament, we found that nodes moved either clockwise or counterclockwise with a fixed velocity, as the force per node was fixed in a homogeneous ring. This explained the experimental observation of bidirectional node motion (Laplante *et al.*, 2016). Such a model also reproduced previously measured values of ring tension (~400 pN, (Stachowiak *et al.*, 2014)) with a myosin force per head ~ 1.1 pN, similar to previous measurements (Kishino and Yanagida, 1988; Molloy *et al.*, 1995; Ishijima *et al.*, 1996; Tyska *et al.*, 1999).

As stated above, nodes attract one another via the force produced by myosin of one node pulling on the actin of another. Such a structure would be prone to clumping instabilities. Our model shows that turnover of nodes prevents such aggregation, and that experimentally measured turnover times are small enough compared with the inherent aggregation timescale of the nodes. Thus, a node-based architecture with nodes turning over is sufficient to generate tension and help the stability of the ring.

Neurotransmission and the post-fusion role of SNAREpins

Neurotransmission involves the crucial step of communication between neurons where membrane-enclosed vesicles filled with neurotransmitter fuse with the membrane of a neuron inside the neuron, thereby opening a fusion pore connecting the interior of the vesicle with the exterior of the cell. Such a connection enables release of the neurotransmitter which is sensed by the next neuron. Thus, the nature of this connection, its stability and how the fusion pore size is regulated are essential to neurotransmission.

SNAREs are the core of the membrane fusion machinery of the cell. Fusion involves the assembly of SNARE complexes at the fusion site, but the roles of these proteins is unclear. Here, using a combination of mathematical modeling and experiments we sought to answer these questions. Our collaborators at Yale prepared an experimental system where patches of membranes (vNLPs) assembled SNARE complexes and fused with the membrane of a cell from the exterior of the cell. Electrophysiological experiments measured the conductance of the ensuing fusion pores and hence their sizes versus time.

We made a mathematical model treating the SNARE complexes with either fully or partially zippered transmembrane domains. The SNAREs could assemble at the waist of the fusion pore, or were free to roam. We saw that zippering energy drove SNAREs to zipper up and assemble at the waist, and entropic crowding forces in at the waist caused the pore to expand. This entropic force explains the experimental observation that average pore sizes are larger with more SNAREs at the fusion site, and suggests that the barrier to fusion pore expansion is ameliorated by the steric interactions between SNAREs. Thus, our work suggests a key post-fusion role of SNAREpins in neurotransmitter release.

References

Acuna, C., Guo, Q., Burre, J., Sharma, M., Sun, J., and Sudhof, T.C. (2014). Microsecond dissection of neurotransmitter release: SNARE-complex assembly dictates speed and Ca(2)(+) sensitivity. Neuron *82*, 1088-1100.

Alabi, A.A., and Tsien, R.W. (2013). Perspectives on kiss-and-run: role in exocytosis, endocytosis, and neurotransmission. Annual review of physiology *75*, 393-422.

Amir, A., Babaeipour, F., McIntosh, D. B., Nelson, D. R., and Jun, S. (2014). Bending forces plastically deform growing bacterial cell walls. Proc. Natl. Acad. Sci. U. S. A. 111, 5778–5783.

Arasada, R., and Pollard, T. D. (2014). Contractile Ring Stability in S. pombe Depends on F-BAR Protein Cdc15p and Bgs1p Transport from the Golgi Complex. Cell Rep. 8, 1533–1544.

Atilgan, E., Magidson, V., Khodjakov, A., and Chang, F. (2015). Morphogenesis of the fission yeast cell through cell wall expansion. Curr. Biol. 25, 2150–2157.

Balasubramanian, M. K., Srinivasan, R., Huang, Y., and Ng, K.-H. (2012). Comparing contractile apparatus-driven cytokinesis mechanisms across kingdoms. Cytoskeleton 69, 942–956.

Bao, H., Goldschen-Ohm, M., Jeggle, P., Chanda, B., Edwardson, J.M., and Chapman, E.R. (2016). Exocytotic fusion pores are composed of both lipids and proteins. Nature structural & molecular biology *23*, 67-73.

Beach, J. R., Shao, L., Remmert, K., Li, D., Betzig, E., and Hammer, J. A. (2014). Nonmuscle myosin II isoforms coassemble in living cells. Curr. Biol. 24, 1160–1166.

Bello, O.D., Auclair, S.M., Rothman, J.E., and Krishnakumar, S.S. (2016). Using ApoE Nanolipoprotein Particles To Analyze SNARE-Induced Fusion Pores. Langmuir : the ACS journal of surfaces and colloids *32*, 3015-3023.

Bezanilla, M., and Pollard, T. D. (2000). Myosin-II tails confer unique functions in Schizosaccharomyces pombe: characterization of a novel myosin-II tail. Mol. Biol. Cell 11, 79–91.

Blanchette, C.D., Law, R., Benner, W.H., Pesavento, J.B., Cappuccio, J.A., Walsworth, V., Kuhn, E.A., Corzett, M., Chromy, B.A., Segelke, B.W., Coleman, M.A., Bench, G., Hoeprich, P.D., and Sulchek, T.A. (2008). Quantifying size distributions of nanolipoprotein particles with single-particle analysis and molecular dynamic simulations. Journal of lipid research *49*, 1420-1430.

Brochard, F., and Lennon, J.F. (1975). Frequency spectrum of the flicker phenomenon in erythrocytes. J. Phys. France *36*, 1035-1047.

Cabib, E., and Arroyo, J. (2013). How carbohydrates sculpt cells: chemical control of morphogenesis in the yeast cell wall. Nat. Rev. Microbiol. 11, 648–655.

Canny, J. (1986). A computational approach to edge detection. IEEE Trans. Pattern Anal. Mach. Intell. 8, 679–698.

Carlier, M. F. (1991). Actin: protein structure and filament dynamics. J. Biol. Chem. 266, 1–4.

Chang, C.W., Chiang, C.W., Gaffaney, J.D., Chapman, E.R., and Jackson, M.B. (2016). Lipid-anchored Synaptobrevin Provides Little or No Support for Exocytosis or Liposome Fusion. The Journal of biological chemistry *291*, 2848-2857.

Chang, C.W., Hui, E., Bai, J., Bruns, D., Chapman, E.R., and Jackson, M.B. (2015). A structural role for the synaptobrevin 2 transmembrane domain in dense-core vesicle fusion pores. The Journal of neuroscience : the official journal of the Society for Neuroscience *35*, 5772-5780.

Chanturiya, A., Chernomordik, L.V., and Zimmerberg, J. (1997). Flickering fusion pores comparable with initial exocytotic pores occur in protein-free phospholipid bilayers. Proceedings of the National Academy of Sciences of the United States of America *94*, 14423-14428.

Chapochnikov, N.M., Takago, H., Huang, C.H., Pangrsic, T., Khimich, D., Neef, J., Auge, E., Gottfert, F., Hell, S.W., Wichmann, C., Wolf, F., and Moser, T. (2014). Uniquantal release through a dynamic fusion pore is a candidate mechanism of hair cell exocytosis. Neuron *83*, 1389-1403.

Chernomordik, L.V., and Kozlov, M.M. (2008). Mechanics of membrane fusion. Nature structural & molecular biology *15*, 675-683.

Chizmadzhev, Y.A., Cohen, F.S., Shcherbakov, A., and Zimmerberg, J. (1995). Membrane mechanics can account for fusion pore dilation in stages. Biophysical journal *69*, 2489-2500.

Chizmadzhev, Y.A., Kuzmin, P.I., Kumenko, D.A., Zimmerberg, J., and Cohen, F.S. (2000). Dynamics of fusion pores connecting membranes of different tensions. Biophys. J. *78,* 2241-2256.

Claessens, M. M. A. E., Bathe, M., Frey, E., and Bausch, A. R. (2006). Actin-binding proteins sensitively mediate F-actin bundle stiffness. Nat. Mater. 5, 748–753.

Cohen, F.S., and Melikyan, G.B. (2004). The energetics of membrane fusion from binding, through hemifusion, pore formation, and pore enlargement. The Journal of membrane biology *199*, 1-14.

Cooke, R. (1997). Actomyosin interaction in striated muscle. Physiol. Rev. 77, 671–697.

Cortés, J. C. G., Carnero, E., Ishiguro, J., Sánchez, Y., Durán, A., and Ribas, J. C. (2005). The novel fission yeast (1,3)beta-D-glucan synthase catalytic subunit Bgs4p is essential during both cytokinesis and polarized growth. J. Cell Sci. 118, 157–174.

Cortés, J. C. G., Konomi, M., Martins, I. M., Muñoz, J., Moreno, M. B., Osumi, M., Durán, A., and Ribas, J. C. (2007). The (1,3)beta-D-glucan synthase subunit Bgs1p is responsible for the fission yeast primary septum formation. Mol. Microbiol. 65, 201–217.

Cortés, J. C. G., Sato, M., Muñoz, J., Moreno, M. B., Clemente-Ramos, J. A., Ramos, M., Okada, H., Osumi, M., Durán, A., and Ribas, J. C. (2012). Fission yeast Ags1 confers the essential septum strength needed for safe gradual cell abscission. J. Cell Biol. 198, 637–656.

Courtemanche, N., Lee, J. Y., Pollard, T. D., and Greene, E. C. (2013). Tension modulates actin filament polymerization mediated by formin and profilin. Proc. Natl. Acad. Sci. U. S. A. 110, 9752–9757.

Courtemanche, N., Pollard, T. D., and Chen, Q. (2016). Avoiding artefacts when counting polymerized actin in live cells with LifeAct fused to fluorescent proteins. Nat. Cell Biol. 18, 676–683.

Curran, M.J., Cohen, F.S., Chandler, D.E., Munson, P.J., and Zimmerberg, J. (1993). Exocytotic fusion pores exhibit semi-stable states. J. Membr. Biol. *133*, 61-75.

Das, M., Drake, T., Wiley, D. J., Buchwald, P., Vavylonis, D., and Verde, F. (2012). Oscillatory Dynamics of Cdc42 GTPase in the Control of Polarized Growth. Science (80-.). 337, 239–243.

Desai, A., and Mitchison, T. J. (1997). Microtubule Polymerization Dynamics. Annu. Rev. Cell Dev. Biol. 13, 83–117.

Dhara, M., Yarzagaray, A., Schwarz, Y., Dutta, S., Grabner, C., Moghadam, P.K., Bost, A., Schirra, C., Rettig, J., Reim, K., Brose, N., Mohrmann, R., and Bruns, D. (2014). Complexin synchronizes primed vesicle exocytosis and regulates fusion pore dynamics. The Journal of cell biology *204*, 1123-1140.

Diao, J., Grob, P., Cipriano, D.J., Kyoung, M., Zhang, Y., Shah, S., Nguyen, A., Padolina, M., Srivastava, A., Vrljic, M., Shah, A., Nogales, E., Chu, S., and Brunger, A.T. (2013). Synaptic proteins promote calcium-triggered fast transition from point contact to full fusion. elife *1*, e00109.

Domanska, M.K., Kiessling, V., Stein, A., Fasshauer, D., and Tamm, L.K. (2010). Single vesicle millisecond fusion kinetics reveals number of SNARE complexes optimal for fast SNARE-mediated membrane fusion Journal of Biological Chemistry *285*, 11753-11753.

Drake, T., and Vavylonis, D. (2013). Model of Fission Yeast Cell Shape Driven by Membrane-Bound Growth Factors and the Cytoskeleton. PLoS Comput Biol 9, e1003287.

Edelstein, A., Amodaj, N., Hoover, K., Vale, R., and Stuurman, N. (2010). Computer control of microscopes using µManager. Curr. Protoc. Mol. Biol. Online Chapter 14, 14.20.1-17.

Edwards, S. F., and Wilkinson, D. R. (1982). The Surface Statistics of a Granular Aggregate. Proc. R. Soc. London. A. Math. Phys. Sci. 381, 17–31.

Engquist, B., Lotstedt, P., and Sjogreen, B. (1989). Nonlinear Filters for Efficient Shock Computation. Math. Comput. 52, 509–537.

Fang, Q.H., Berberian, K., Gong, L.W., Hafez, I., Sorensen, J.B., and Lindau, M. (2008). The role of the C terminus of the SNARE protein SNAP-25 in fusion pore opening and a model for fusion pore mechanics. Proceedings of the National Academy of Sciences of the United States of America *105*, 15388-15392.

Fdez, E., Martinez-Salvador, M., Beard, M., Woodman, P., and Hilfiker, S. (2010). Transmembrane-domain determinants for SNARE-mediated membrane fusion. Journal of cell science *123*, 2473-2480.

Fenix, A. M., Taneja, N., Buttler, C. A., Lewis, J., Van Engelenburg, S. B., Ohi, R., and Burnette, D. T. (2016). Expansion and concatenation of nonmuscle myosin IIA filaments drive cellular contractile system formation during interphase and mitosis. Mol. Biol. Cell 27, 1465–1478.

Fujiwara, K., and Pollard, T. D. (1976). Fluorescent antibody localization of myosin in the cytoplasm, cleavage furrow, and mitotic spindle of human cells. J. Cell Biol. 71, 848–875.

Fulop, T., Radabaugh, S., and Smith, C. (2005). Activity-dependent differential transmitter release in mouse adrenal chromaffin cells. Journal of Neuroscience *25*, 7324-7332.

Furchtgott, L., Wingreen, N. S., and Huang, K. C. (2011). Mechanisms for maintaining cell shape in rod-shaped Gram-negative bacteria. Mol. Microbiol. 81, 340–353.

Gao, Y., Zorman, S., Gundersen, G., Xi, Z., Ma, L., Sirinakis, G., Rothman, J.E., and Zhang, Y. (2012). Single reconstituted neuronal SNARE complexes zipper in three distinct stages. Science *337*, 1340-1343.

Gao, Y., Zorman, S., Gundersen, G., Xi, Z., Ma, L., Sirinakis, G., Rothman, J. E., and Zhang, Y. (2012). Single Reconstituted Neuronal SNARE Complexes Zipper in Three Distinct Stages. Science (80-.). 337, 1340–1343.

Geertsema, H. J., Kulczyk, A. W., Richardson, C. C., and van Oijen, A. M. (2014). Single-molecule studies of polymerase dynamics and stoichiometry at the bacteriophage T7 replication machinery. Proc. Natl. Acad. Sci. U. S. A. 111, 4073–4078.

Giraudo, C.G., Eng, W.S., Melia, T.J., and Rothman, J.E. (2006). A clamping mechanism involved in SNARE-dependent exocytosis. Science *313*, 676-680.

Green, R. A., Paluch, E., and Oegema, K. (2012). Cytokinesis in Animal Cells. Annu. Rev. Cell Dev. Biol. 28, 29–58.

Haluska, C.K., Riske, K.A., Marchi-Artzner, V., Lehn, J.M., Lipowsky, R., and Dimova, R. (2006). Time scales of membrane fusion revealed by direct imaging of vesicle fusion with high temporal resolution. Proc. Natl. Acad. Sci. U. S. A. *103*, 15841-15846.

Han, X., Wang, C.T., Bai, J.H., Chapman, E.R., and Jackson, M.B. (2004). Transmembrane segments of syntaxin line the fusion pore of Ca2+-triggered exocytosis. Science *304*, 289-292.

Hanna, S.T., Pigeau, G.M., Galvanovskis, J., Clark, A., Rorsman, P., and MacDonald, P.E. (2009). Kiss-and-run exocytosis and fusion pores of secretory vesicles in human beta-cells. Pflugers Archiv-European Journal of Physiology *457*, 1343-1350.

He, L., and Wu, L.G. (2007). The debate on the kiss-and-run fusion at synapses. Trends in neurosciences *30*, 447-455.

He, L.M., Wu, X.S., Mohan, R., and Wu, L.G. (2006). Two modes of fusion pore opening revealed by cell-attached recordings at a synapse. Nature *444*, 102-105.

Henson, J. H., Ditzler, C. E., Germain, A., Irwin, P. M., Vogt, E. T., Yang, S., Wu, X., and Shuster, C. B. (2017). The ultrastructural organization of actin and myosin II filaments in the contractile ring: new support for an old model of cytokinesis. Mol. Biol. Cell 28, 613–623.

Hermann, H., Schmidt, P. W., and Schneider, F. (1995). Fractal growth of FeO(OH) during corrosion. J. Mater. Sci. Lett. 14, 816–819.

Hernandez, J.M., Kreutzberger, A.J., Kiessling, V., Tamm, L.K., and Jahn, R. (2014). Variable cooperativity in SNARE-mediated membrane fusion. Proc Natl Acad Sci U S A *111*, 12037-12042.

Hille, B. (2001). Ion channels of excitable membranes. Sinauer: Sunderland, Mass.

Hu, C., Ahmed, M., Melia, T.J., Sollner, T.H., Mayer, T., and Rothman, J.E. (2003). Fusion of cells by flipped SNAREs. Science *300*, 1745-1749.

Hytönen, V. P., and Vogel, V. (2005). How force might activate talin's vinculin binding sites: SMD reveals a structural mechanism. PLoS Comput. Biol. preprint, e24.

Ishijima, A., Kojima, H., Higuchi, H., Harada, Y., Funatsu, T., and Yanagida, T. (1996). Multiple- and single-molecule analysis of the actomyosin motor by nanometer-piconewton manipulation with a microneedle: unitary steps and forces. Biophys. J. 70, 383–400.

Jackson, M.B. (2009). Minimum membrane bending energies of fusion pores. The Journal of membrane biology *231*, 101-115.

Jackson, M.B. (2010). SNARE complex zipping as a driving force in the dilation of proteinaceous fusion pores. J. Membr. Biol. *235*, 89-100.

Jahn, R., and Scheller, R. H. (2006). SNAREs — engines for membrane fusion. Nat. Rev. Mol. Cell Biol. 7, 631–643.

Jahn, R., and Scheller, R.H. (2006). SNAREs - engines for membrane fusion. Nature Reviews Molecular Cell Biology *7*, 631-643.

Jégou, A., Carlier, M.-F., and Romet-Lemonne, G. (2013). Formin mDia1 senses and generates mechanical forces on actin filaments. Nat Commun 4, 1883.

Jorgacevski, J., Potokar, M., Grilc, S., Kreft, M., Liu, W., Barclay, J.W., Buckers, J., Medda, R., Hell, S.W., Parpura, V., Burgoyne, R.D., and Zorec, R. (2011). Munc18-1 Tuning of Vesicle Merger and Fusion Pore Properties. Journal of Neuroscience *31*, 9055-9066.

Kamasaki, T., Osumi, M., and Mabuchi, I. (2007). Three-dimensional arrangement of F-actin in the contractile ring of fission yeast. J. Cell Biol. 178, 765–771.

Kanbe, T., Kobayashi, I., and Tanaka, K. (1989a). Dynamics of cytoplasmic organelles in the cell cycle of the fission yeast Schizosaccharomyces pombe: three-dimensional reconstruction from serial sections. J. Cell Sci. 94, 647–656.

Kanbe, T., Kobayashi, I., and Tanaka, K. (1989b). Dynamics of cytoplasmic organelles in the cell cycle of the fission yeast Schizosaccharomyces pombe: three-dimensional reconstruction from serial sections. J. Cell Sci. 94, 647–656.

Karatekin, E., Di Giovanni, J., Iborra, C., Coleman, J., O'Shaughnessy, B., Seagar, M., and Rothman, J.E. (2010). A fast, single-vesicle fusion assay mimics physiological SNARE requirements. Proceedings of the National Academy of Sciences of the United States of America *107*, 3517-3521.

Kardar, M., Parisi, G., and Zhang, Y.-C. Y. (1986). Dynamic Scaling of Growing Interfaces. Phys. Rev. Lett. 56, 889–892.

Kesavan, J., Borisovska, M., and Bruns, D. (2007). v-SNARE actions during Ca(2+)-triggered exocytosis. Cell *131*, 351-363.

Khelashvili, G., Kollmitzer, B., Heftberger, P., Pabst, G., and Harries, D. (2013). Calculating the Bending Modulus for Multicomponent Lipid Membranes in Different Thermodynamic Phases. J. Chem. Theory Comput. *9*, 3866-3871.

Kishino, A., and Yanagida, T. (1988). Force measurements by micromanipulation of a single actin filament by glass needles. Nature 334, 74–76.

Kitayama, C., Sugimoto, A., and Yamamoto, M. (1997). Type II myosin heavy chain encoded by the myo2 gene composes the contractile ring during cytokinesis in Schizosaccharomyces pombe. J. Cell Biol. 137, 1309–1319.

Klyachko, V.A., and Jackson, M.B. (2002). Capacitance steps and fusion pores of small and large-dense-core vesicles in nerve terminals. Nature *418*, 89-92.

Knecht, V., and Grubmuller, H. (2003). Mechanical coupling via the membrane fusion SNARE protein syntaxin 1A: a molecular dynamics study. Biophys. J. *84*, 1527-1547.

Knowles, M.K., Barg, S., Wan, L., Midorikawa, M., Chen, X., and Almers, W. (2010). Single secretory granules of live cells recruit syntaxin-1 and synaptosomal associated protein 25 (SNAP-25) in large copy numbers. Proc Natl Acad Sci U S A *107*, 20810-20815.

Kovar, D. R., Harris, E. S., Mahaffy, R., Higgs, H. N., and Pollard, T. D. (2006). Control of the assembly of ATP- and ADP-actin by formins and profilin. Cell 124, 423–435.

Kozlov, M.M., Leikin, S.L., Chernomordik, L.V., Markin, V.S., and Chizmadzhev, Y.A. (1989). Stalk mechanism of vesicle fusion. Intermixing of aqueous contents. Eur. Biophys. J. *17*, 121-129.

Krapp, A., and Simanis, V. (2008). An overview of the fission yeast septation initiation network (SIN). Biochem. Soc. Trans. 36, 411–415.

Krishnakumar, S.S., Kummel, D., Jones, S.J., Radoff, D.T., Reinisch, K.M., and Rothman, J.E. (2013). Conformational dynamics of calcium-triggered activation of fusion by synaptotagmin. Biophysical journal *105*, 2507-2516.

Krishnakumar, S.S., Radoff, D.T., Kummel, D., Giraudo, C.G., Li, F., Khandan, L., Baguley, S.W., Coleman, J., Reinisch, K.M., Pincet, F., and Rothman, J.E. (2011). A conformational switch in complexin is required for synaptotagmin to trigger synaptic fusion. Nature structural & molecular biology *18*, 934-940.

Lacroix, B., and Maddox, A. S. (2012). Cytokinesis, ploidy and aneuploidy. J. Pathol. 226, 338–351.

Lai, Y., Diao, J., Liu, Y., Ishitsuka, Y., Su, Z., Schulten, K., Ha, T., and Shin, Y.K. (2013). Fusion pore formation and expansion induced by Ca2+ and synaptotagmin 1. Proc Natl Acad Sci U S A *110*, 1333-1338.

Laplante, C., Berro, J., Karatekin, E., Hernandez-Leyva, A., Lee, R., and Pollard, T. D. (2015). Three Myosins Contribute Uniquely to the Assembly and Constriction of the Fission Yeast Cytokinetic Contractile Ring. Curr. Biol. 25, 1955–1965.

Laplante, C., Huang, F., Tebbs, I. R., Bewersdorf, J., and Pollard, T. D. (2016). Molecular organization of cytokinesis nodes and contractile rings by super-resolution fluorescence microscopy of live fission yeast. Proc. Natl. Acad. Sci. 113, E5876–E5885.

Lapujoulade, J. (1994). The roughening of metal surfaces. Surf. Sci. Rep. 20, 195–249.

Larson, M. H., Zhou, J., Kaplan, C. D., Palangat, M., Kornberg, R. D., Landick, R., and Block, S. M. (2012). Trigger loop dynamics mediate the balance between the transcriptional fidelity and speed of RNA polymerase II. Proc. Natl. Acad. Sci. U. S. A. 109, 6555–6560.

Le Goff, X., Motegi, F., Salimova, E., Mabuchi, I., and Simanis, V. (2000). The S. pombe rlc1 gene encodes a putative myosin regulatory light chain that binds the type II myosins myo3p and myo2p. J. Cell Sci. 113, 4157–4163.

Lesne, A., and Laguës, M. (2012). Growth and Roughness of Interfaces. In: Scale Invariance, Springer Berlin Heidelberg, 259–291.

Li, Y., Christensen, J. R., Homa, K. E., Hocky, G. M., Fok, A., Sees, J. A., Voth, G. A., and Kovar, D. R. (2016). The F-actin bundler α-actinin Ain1 is tailored for ring assembly and constriction during cytokinesis in fission yeast. Mol. Biol. Cell 27, 1821–1833.

Lieber, R. L., and Ward, S. R. (2011). Skeletal muscle design to meet functional demands. Philos. Trans. R. Soc. B Biol. Sci. 366, 1466–1476.

Lindau, M. (2012). High resolution electrophysiological techniques for the study of calcium-activated exocytosis. Biochimica Et Biophysica Acta-General Subjects *1820*, 1234-1242.

Lindau, M., and de Toledo, G.A. (2003). The fusion pore. Biochimica Et Biophysica Acta-Molecular Cell Research *1641*, 167-173.

Liu, J., Tang, X., Wang, H., Oliferenko, S., and Balasubramanian, M. K. (2002). The Localization of the Integral Membrane Protein Cps1p to the Cell Division Site is Dependent on the Actomyosin Ring and the Septation-Inducing Network in Schizosaccharomyces pombe. Mol. Biol. Cell 13, 989–1000.

Liu, X., Seven, A.B., Camacho, M., Esser, V., Xu, J., Trimbuch, T., Quade, B., Su, L., Ma, C., Rosenmund, C., and Rizo, J. (2016). Functional synergy between the Munc13 C-terminal C1 and C2 domains. Elife *5*.

Mabuchi, I. (1986). Biochemical aspects of cytokinesis. Int. Rev. Cytol. 101, 175–213.

Mabuchi, I., and Okuno, M. (1977). The effect of myosin antibody on the division of starfish blastomeres. J. Cell Biol. 74, 251–263.

MacDonald, P.E., Braun, M., Galvanovskis, J., and Rorsman, P. (2006). Release of small transmitters through kiss-and-run fusion pores in rat pancreatic beta cells. Cell metabolism *4*, 283-290.

Marsh, D. (2006). Elastic curvature constants of lipid monolayers and bilayers. Chem. Phys. Lipids *144*, 146-159.

Martín, V., García, B., Carnero, E., Durán, A., and Sánchez, Y. (2003). Bgs3p, a putative 1,3-beta-glucan synthase subunit, is required for cell wall assembly in Schizosaccharomyces pombe. Eukaryot. Cell 2, 159–169.

Maupin, P., and Pollard, T. D. (1986). Arrangement of actin filaments and myosin-like filaments in the contractile ring and of actin-like filaments in the mitotic spindle of dividing HeLa cells. J. Ultrastruct. Mol. Struct. Res. 94, 92–103.

Mcdonald, N. A., Lind, A. L., Smith, S. E., Li, R., and Gould, K. L. (2017). Nanoscale architecture of the Schizosaccharomyces pombe contractile ring.

McNew, J.A., Weber, T., Parlati, F., Johnston, R.J., Melia, T.J., Sollner, T.H., and Rothman, J.E. (2000). Close is not enough: SNARE-dependent membrane fusion requires an active mechanism that transduces force to membrane anchors. The Journal of cell biology *150*, 105-117.

Melikov, K.C., Frolov, V.A., Shcherbakov, A., Samsonov, A.V., Chizmadzhev, Y.A., and Chernomordik, L.V. (2001). Voltage-induced nonconductive pre-pores and metastable single pores in unmodified planar lipid bilayer. Biophysical journal *80*, 1829-1836.

Mellander, L.J., Kurczy, M.E., Najafinobar, N., Dunevall, J., Ewing, A.G., and Cans, A.S. (2014). Two modes of exocytosis in an artificial cell. Scientific reports *4*, 3847.

Mellander, L.J., Trouillon, R., Svensson, M.I., and Ewing, A.G. (2012). Amperometric post spike feet reveal most exocytosis is via extended kiss-and-run fusion. Scientific reports *2*, 907.

Michelot, A., Berro, J., Guérin, C., Boujemaa-Paterski, R., Staiger, C. J., Martiel, J.-L., and Blanchoin, L. (2007). Actin-Filament Stochastic Dynamics Mediated by ADF/Cofilin. Curr. Biol. 17, 825–833.

Minc, N., Boudaoud, A., and Chang, F. (2009). Mechanical forces of fission yeast growth. Curr. Biol. 19, 1096–1101.

Mitra, K., Ubarretxena-Belandia, I., Taguchi, T., Warren, G., and Engelman, D.M. (2004). Modulation of the bilayer thickness of exocytic pathway membranes by membrane proteins rather than cholesterol. Proc. Natl. Acad. Sci. U. S. A. *101*, 4083-4088.

Mohrmann, R., de Wit, H., Verhage, M., Neher, E., and Sorensen, J.B. (2010). Fast Vesicle Fusion in Living Cells Requires at Least Three SNARE Complexes. Science *330*, 502-505.

Molloy, J. E., Burns, J. E., Kendrick-Jones, J., Tregear, R. T., and White, D. C. (1995). Movement and force produced by a single myosin head. Nature 378, 209–212.

Montecucco, C., Schiavo, G., and Pantano, S. (2005). SNARE complexes and neuroexocytosis: how many, how close? Trends in Biochemical Sciences *30*, 367-372.

Morrow, J.A., Arnold, K.S., and Weisgraber, K.H. (1999). Functional characterization of apolipoprotein E isoforms overexpressed in Escherichia coli. Protein expression and purification *16*, 224-230.

Mostafavi, H., Thiyagarajan, S., Stratton, B. S., Karatekin, E., Warner, J. M., Rothman, J. E., and O'Shaughnessy, B. (2017). Entropic forces drive self-organization and membrane fusion by SNARE proteins. Proc. Natl. Acad. Sci. U. S. A. 114.

Muñoz, J., Cortés, J. C. G., Sipiczki, M., Ramos, M., Clemente-Ramos, J. A., Moreno, M. B., Martins, I. M., Pérez, P., and Ribas, J. C. (2013). Extracellular cell wall β(1,3)glucan is required to couple septation to actomyosin ring contraction. J. Cell Biol. 203, 265–282.

Munro, C. a (2013). Chitin and Glucan, the Yin and Yang of the Fungal Cell Wall, Implications for Antifungal Drug Discovery and Therapy. In: Advances in Applied Microbiology, Elsevier, 145–172.

Nanavati, C., Markin, V.S., Oberhauser, A.F., and Fernandez, J.M. (1992). The Exocytotic Fusion Pore Modeled as a Lipidic Pore. Biophysical journal *63*, 1118-1132.

Nattermann, T., and Tang, L.-H. (1992). Kinetic surface roughening. I. The Kardar-Parisi-Zhang equation in the weak-coupling regime. Phys. Rev. A 45, 7156–7161.

Parlati, F., Weber, T., McNew, J.A., Westermann, B., Sollner, T.H., and Rothman, J.E. (1999). Rapid and efficient fusion of phospholipid vesicles by the alpha-helical core of a SNARE complex in the absence of an N-terminal regulatory domain. Proc Natl Acad Sci U S A *96*, 12565-12570.

Pawlu, C., DiAntonio, A., and Heckmann, M. (2004). Postfusional control of quantal current shape. Neuron *42*, 607-618.

Pelham, R. J., and Chang, F. (2002). Actin dynamics in the contractile ring during cytokinesis in fission yeast. Nature 419, 82–86.

Pinho, M. G., Kjos, M., and Veening, J.-W. (2013). How to get (a)round: mechanisms controlling growth and division of coccoid bacteria. Nat. Rev. Microbiol. 11, 601–614.

Pollard, T. D., and Wu, J.-Q. (2010). Understanding cytokinesis: lessons from fission yeast. Nat. Rev. Mol. Cell Biol. 11, 149–155.

Proctor, S. a, Minc, N., Boudaoud, A., and Chang, F. (2012). Contributions of turgor pressure, the contractile ring, and septum assembly to forces in cytokinesis in fission yeast. Curr. Biol. 22, 1601–1608.

Rand, R.P., and Parsegian, V.A. (1989). Hydration forces between phospholipid bilayers. Biochim Biophys Acta *988*, 351-376.

Ritchie, T.K., Grinkova, Y.V., Bayburt, T.H., Denisov, I.G., Zolnerciks, J.K., Atkins, W.M., and Sligar, S.G. (2009). Reconstitution of Membrane Proteins in Phospholipid Bilayer Nanodiscs. Method Enzymol *464*, 211-231.

Rizo, J., and Xu, J. (2015). The Synaptic Vesicle Release Machinery. Annual review of biophysics *44*, 339-367.

Roberts-Galbraith, R. H., Chen, J.-S., Wang, J., and Gould, K. L. (2009). The SH3 domains of two PCH family members cooperate in assembly of the Schizosaccharomyces pombe contractile ring. J. Cell Biol. 184, 113–127.

Sakmann, B., and Neher, E. (2009). Single-channel recording. Springer: New York, NY.

Sanger, J. M., and Sanger, J. W. (1980). Banding and polarity of actin filaments in interphase and cleaving cells. J. Cell Biol. 86, 568–575.

Schiaffino, S., and Reggiani, C. (2011). Fiber Types in Mammalian Skeletal Muscles. Physiol. Rev. 91, 1447–1531.

Schoen, I., Pruitt, B. L., and Vogel, V. (2013). The Yin-Yang of Rigidity Sensing: How Forces and Mechanical Properties Regulate the Cellular Response to Materials. Annu. Rev. Mater. Res. 43, 589–618.

Schroeder, T. E. (1972). The contractile ring: II. determining its brief existence, volumetric changes, and vital role in cleaving arbacia eggs. J. Cell Biol. 53, 419–434.

Schroeder, T. E. (1975). Dynamics of the contractile ring. Soc. Gen. Physiol. Ser. 30, 305–334.

Shi, L., Howan, K., Shen, Q.T., Wang, Y.J., Rothman, J.E., and Pincet, F. (2013). Preparation and characterization of SNARE-containing nanodiscs and direct study of cargo release through fusion pores. Nat Protoc *8*, 935-948.

Shi, L., Shen, Q.T., Kiel, A., Wang, J., Wang, H.W., Melia, T.J., Rothman, J.E., and Pincet, F. (2012). SNARE Proteins: One to Fuse and Three to Keep the Nascent Fusion Pore Open. Science *335*, 1355-1359.

Sinha, R., Ahmed, S., Jahn, R., and Klingauf, J. (2011). Two synaptobrevin molecules are sufficient for vesicle fusion in central nervous system synapses. Proc Natl Acad Sci U S A *108*, 14318-14323.

Sladewski, T. E., Previs, M. J., and Lord, M. (2009). Regulation of fission yeast myosin-II function and contractile ring dynamics by regulatory light-chain and heavy-chain phosphorylation. Mol. Biol. Cell 20, 3941–3952.

Sparks, C. A., Morphew, M., and McCollum, D. (1999). Sid2p, a Spindle Pole Body Kinase That Regulates the Onset of Cytokinesis. J. Cell Biol. 146, 777–790.

Staal, R.G.W., Mosharov, E.V., and Sulzer, D. (2004). Dopamine neurons release transmitter via a flickering fusion pore. Nature neuroscience *7*, 341-346.

Stachowiak, M. R., Laplante, C., Chin, H. F., Guirao, B., Karatekin, E., Pollard, T. D., and O’Shaughnessy, B. (2014). Mechanism of Cytokinetic Contractile Ring Constriction in Fission Yeast. Dev. Cell 29, 547–561.

Stark, B. C., Sladewski, T. E., Pollard, L. W., and Lord, M. (2010). Tropomyosin and Myosin-II Cellular Levels Promote Actomyosin Ring Assembly in Fission Yeast. Mol. Biol. Cell 21, 989–1000.

Stegemann, B., Ritter, C., Kaiser, B., and Rademann, K. (2004). Crystallization of antimony nanoparticles: Pattern formation and fractal growth. J. Phys. Chem. B 108, 14292–14297.

Stein, A., Weber, G., Wahl, M.C., and Jahn, R. (2009). Helical extension of the neuronal SNARE complex into the membrane. Nature *460*, 525-U105.

Stratton, B.S., Warner, J.M., Wu, Z., Nikolaus, J., Wei, G., Wagnon, E., Baddeley, D., Karatekin, E., and O'Shaughnessy, B. (2016). Cholesterol Increases the Openness of SNARE-Mediated Flickering Fusion Pores. Biophysical journal *110*, 1538-1550.

Streiblova, E., Hasek, J., and Jelke, E. (1984). Septum pattern in ts mutants of Schizosaccharomyces pombe defective in genes cdc3, cdc4, cdc8 and cdc12. J. Cell Sci. 69, 47–65.

Südhof, T. C., and Rothman, J. E. (2009). Membrane Fusion: Grappling with SNARE and SM Proteins. Sci. 323, 474–477.

Sudhof, T.C., and Rothman, J.E. (2009). Membrane Fusion: Grappling with SNARE and SM Proteins. Science *323*, 474-477.

Takamori, S., Holt, M., Stenius, K., Lemke, E.A., Gronborg, M., Riedel, D., Urlaub, H., Schenck, S., Brugger, B., Ringler, P., Muller, S.A., Rammner, B., Grater, F., Hub, J.S., De Groot, B.L., Mieskes, G., Moriyama, Y., Klingauf, J., Grubmuller, H., Heuser, J., Wieland, F., and Jahn, R. (2006). Molecular anatomy of a trafficking organelle. Cell *127*, 831-846.

Tebbs, I. R., and Pollard, T. D. (2013). Separate roles of IQGAP Rng2p in forming and constricting the Schizosaccharomyces pombe cytokinetic contractile ring. Mol. Biol. Cell 24, 1904–1917.

Thiyagarajan, S., Munteanu, E. L., Arasada, R., Pollard, T. D., and O’Shaughnessy, B. (2015). The fission yeast cytokinetic contractile ring regulates septum shape and closure. J. Cell Sci. 128.

Thiyagarajan, S., Wang, S., and O’Shaughnessy, B. (2017). A node organization in the actomyosin contractile ring generates tension and aids stability. Mol. Biol. Cell 28, 3286–3297.

Tyska, M. J., Dupuis, D. E., Guilford, W. H., Patlak, J. B., Waller, G. S., Trybus, K. M., Warshaw, D. M., and Lowey, S. (1999). Two heads of myosin are better than one for generating force and motion. Proc. Natl. Acad. Sci. U. S. A. 96, 4402–4407.

Umbach, D., and Jones, K. (2003). A few methods for fitting circles to data. IEEE Trans. Instrum. Meas. 52, 1881–1885.

Ursell, T. S., Nguyen, J., Monds, R. D., Colavin, A., Billings, G., Ouzounov, N., Gitai, Z., Shaevitz, J. W., and Huang, K. C. (2014). Rod-like bacterial shape is maintained by feedback between cell curvature and cytoskeletal localization. Proc. Natl. Acad. Sci. U. S. A. 111, E1025-34.

van den Bogaart, G., Holt, M.G., Bunt, G., Riedel, D., Wouters, F.S., and Jahn, R. (2010). One SNARE complex is sufficient for membrane fusion. Nature structural & molecular biology *17*, 358-U129.

Vavylonis, D., Wu, J.-Q., Hao, S., O’Shaughnessy, B., and Pollard, T. D. (2008). Assembly mechanism of the contractile ring for cytokinesis by fission yeast. Science 319, 97–100.

Vavylonis, D., Yang, Q., and O’Shaughnessy, B. (2005). Actin polymerization kinetics, cap structure, and fluctuations. Proc. Natl. Acad. Sci. U. S. A. 102, 8543–8548.

Wang, C.T., Grishanin, R., Earles, C.A., Chang, P.Y., Martin, T.F., Chapman, E.R., and Jackson, M.B. (2001). Synaptotagmin modulation of fusion pore kinetics in regulated exocytosis of dense-core vesicles. Science *294*, 1111-1115.

Wang, C.T., Lu, J.C., Bai, J.H., Chang, P.Y., Martin, T.F.J., Chapman, E.R., and Jackson, M.B. (2003a). Different domains of synaptotagmin control the choice between kiss-and-run and full fusion. Nature *424*, 943-947.

Wang, C.T., Lu, J.C., Chapman, E.R., Martin, T.F.J., and Jackson, M.B. (2003b). Synaptotagmin IV induces long-duration kiss-and-run exocytosis through small fusion pores. Biophysical journal *84*, 209a-209a.

Wang, H. B., Dembo, M., Hanks, S. K., and Wang, Y. (2001). Focal adhesion kinase is involved in mechanosensing during fibroblast migration. Proc. Natl. Acad. Sci. U. S. A. 98, 11295–11300.

Wang, L., and Tran, P. T. (2014). Visualizing single rod-shaped fission yeast vertically in micro-sized holes on agarose pad made by soft lithography. Methods Cell Biol. 120, 227–234.

Wang, M. D., Schnitzer, M. J., Yin, H., Landick, R., and Gelles, J. (1998). Force and velocity measured for single molecules of RNA polymerase. Science 282, 902–907.

Weber, T., Zemelman, B.V., McNew, J.A., Westermann, B., Gmachl, M., Parlati, F., Sollner, T.H., and Rothman, J.E. (1998). SNAREpins: Minimal machinery for membrane fusion. Cell *92*, 759-772.

Wolf, W. a, Chew, T. L., and Chisholm, R. L. (1999). Regulation of cytokinesis. Cell. Mol. Life Sci. 55, 108–120.

Wollrab, V., Thiagarajan, R., Wald, A., Kruse, K., and Riveline, D. (2016). Still and rotating myosin clusters determine cytokinetic ring constriction. Nat. Commun. 7, 11860.

Wood, V. et al. (2002). The genome sequence of Schizosaccharomyces pombe. Nature 415, 871–880.

Wu, J.-Q., and Pollard, T. D. (2005). Counting cytokinesis proteins globally and locally in fission yeast. Science 310, 310–314.

Wu, J.-Q., Sirotkin, V., Kovar, D. R., Lord, M., Beltzner, C. C., Kuhn, J. R., and Pollard, T. D. (2006). Assembly of the cytokinetic contractile ring from a broad band of nodes in fission yeast. J. Cell Biol. 174, 391–402.

Wu, Z., Auclair, S.M., Bello, O., Vennekate, W., Dudzinski, N.R., Krishnakumar, S.S., and Karatekin, E. (2016). Nanodisc-cell fusion: control of fusion pore nucleation and lifetimes by SNARE protein transmembrane domains. Scientific reports *6*, 27287.

Wu, Z., Bello, O. D., Thiyagarajan, S., Auclair, S. M., Vennekate, W., Krishnakumar, S. S., O'Shaughnessy, B., and Karatekin, E. (2017). Dilation of fusion pores by crowding of SNARE proteins. Elife 6.

Yang, Y., and Sigworth, F.J. (1998). Single-channel properties of IKs potassium channels. The Journal of general physiology *112,* 665-678.

Yonetani, A., Lustig, R. J., Moseley, J. B., Takeda, T., Goode, B. L., and Chang, F. (2008). Regulation and Targeting of the Fission Yeast Formin cdc12p in Cytokinesis. Mol. Biol. Cell 19, 2208–2219.

Zhao, Y., Fang, Q., Herbst, A.D., Berberian, K.N., Almers, W., and Lindau, M. (2013). Rapid structural change in synaptosomal-associated protein 25 (SNAP25) precedes the fusion of single vesicles with the plasma membrane in live chromaffin cells. Proc Natl Acad Sci U S A *110*, 14249-14254.

Zhou, Z., Munteanu, E. L., He, J., Ursell, T., Bathe, M., Huang, K. C., and Chang, F. (2015). The contractile ring coordinates curvature-dependent septum assembly during fission yeast cytokinesis. Mol. Biol. Cell 26, 78–90.